DESIGN OF A MICROELECTROMECHANICAL TRANSDUCER FOR ELECTRIC FIELD MEASUREMENT

BY

Andrew Roncin

A Thesis submitted to
the Faculty of Graduate Studies
In Partial Fulfillment of the Requirements for the Degree of

MASTER OF SCIENCE

Department of Electrical and Computer Engineering
University of Manitoba
Winnipeg, Manitoba

THE UNIVERSITY OF MANITOBA

FACULTY OF GRADUATE STUDIES

*****

COPYRIGHT PERMISSION

DESIGN OF A MICROELECTROMECHANICAL TRANSDUCER FOR ELECTRIC FIELD MEASUREMENT

BY

Andrew Roncin

A Thesis/Practicum submitted to the Faculty of Graduate Studies of The University of Manitoba in partial fulfillment of the requirement of the degree

Of

MASTER OF SCIENCE

ABSTRACT

This thesis covers the design, fabrication, and measurement results of a micromachined electric field sensor. The sensor runs in three electrical modes of operation through the expansion E^2, where $E = E_{DC} + E_{AC}$ and $E^2 = E_{DC}^2 + 2*E_{AC} E_{DC} + E_{AC}^2$. Measuring the response of each term, sensitivities of 7.7kV/m, 0.31V/m, and 139V/m were found respectively.

The sensor uses electrostatic attraction to generate a force between a grounded membrane and an external field source. This electrostatic force moves a 500 μg sense plate up in a square ratio to the magnitude of the electric field. By controlling the lengths of springs supporting the membrane, fields up to 3MV/m could be measured.

The key advantage of this sensor over existing technology is it's small size, single moving part, and potential for low cost yet robust manufacturing. While it's disadvantage lies in the environmental protection required for the sense element.

For atmospheric field measurements for environmental and HVDC field sensing, this design shows promise and is worth further consideration.

ACKNOWLEDGEMENTS

To all the people who encouraged and supported me in my masters -- thank-you. Without your support and understanding, this wonderful journey would not have been possible.

Cyrus Shafai and David Swatek deserve special thanks. As an advisor, Cyrus' knowledge, sensitivity, and support have all been deeply appreciated. David Swatek created the impetus for this thesis and helped make sponsorship from Manitoba Hydro a reality.

Finally, to you the reader -- thank-you for taking the time to pick-up this text. May the information inside prove useful and relevant to your own research.

Andrew Roncin, 2004

TABLE OF CONTENTS

LIST OF FIGURES

LIST OF TABLES

NONCLEMENTURE

Variables

k	Spring constant	
z	Distance in the z direction	m
z_0	Steady state deflection caused by gravity	m
Δz	Differential change in height due to the electric field	m
Force Terms		
F_e	Electric Field Force	N
F_g	Gravitational Force	N
F_m	Mechanical Force due to the springs	N
A	Area of the membrane, 6.25 mm^2	m^2
Electric Field Terms		
$\mathbf{E}$	Electric Field	V/m
ε_o	8.854E-12	F/m
$\mathbf{D}$	$\mathbf{D} = \varepsilon_r \varepsilon_o \mathbf{E}$, electric displacement	
E^2	$\mathbf{E} \bullet \mathbf{E}^*$	V^2/m^2
E_{DC}	DC component of the Electric Field	V/m
E_{AC}	AC component of the Electric Field	V/m
E_n	Field strength contained within the noise envelope	V/m
d	Distance between plates in a capacitor, distance between overhead conductor and the ground plane	m
V_{DC}	DC or DC pulse voltage on the overhead conductor	V
V_{AC}	AC voltage on the overhead conductor	V
V_x	Horizontal output signal	V
V_y	Vertical output signal	V
V_s	Combined output signal	
Mechanical Constants		
$E_{Young's}$	Young's modulus	Pa
w	Width of the beam	m
t	Thickness	m
L	Length (length of a cantilever beam)	m
$N_{parallel}$	Spring lengths in parallel	
N_{series}	Spring lengths in series	

Chapter 1: INTRODUCTION

> "..microtransducers, while relying on silicon technology, are quite different from silicon IC devices. Electronic microtransducers involve a wealth of physical effects beyond the closed world of electrical effects basic to IC devices. Designing microtransducers requires in-depth knowledge of the physics, chemistry, or biology of the targeted non-electrical sensor input..."[1]

1.1 DESIGN CONTEXT

This research idea comes from David Swatek at Manitoba Hydro. His idea was to investigate using micromachining to see if this technology could overcome the reliability and power consumption problems of existing equipment. As such, the goal of this thesis is to demonstrate a proof of concept micromachined electric field sensor. If successful, future development would likely include optimization, packaging, and field testing of the sensor.

The goal of this research is to demonstrate an electrostatic force based micromachined electric field sensor.

To do this, several objectives needed to be accomplished

1. Conceive a micromachining compatible measurement scheme.
2. Acquire information on micromachining, electric field measurement, thin-film mechanics, and instrumentation electronics.
3. Design and fabricate the micromachined parts.
4. Develop and assemble a test platform.
5. Determine meaningful tests to demonstrate the proof-of-concept.
6. Test and document the device.

The scope of this thesis is to lay the groundwork for developing a force based electric field sensor. As such, the 6 objectives cited above have been met, culminating in documentation through this thesis. However, optimization, packaging, and the creation of a field ready sensor are challenges left for future engineers.

1.2 Design Problem

1.2.1 Operating Range

As a ground referenced sensor, this device should detect atmospheric fields in an outdoor environment. The reasonable operating environments range from nice sunny days (200V/m) to lightening storm conditions (3MV/m). Because of its placement on/in the ground, the fields are expected to be perpendicular to the plane of the sensor.

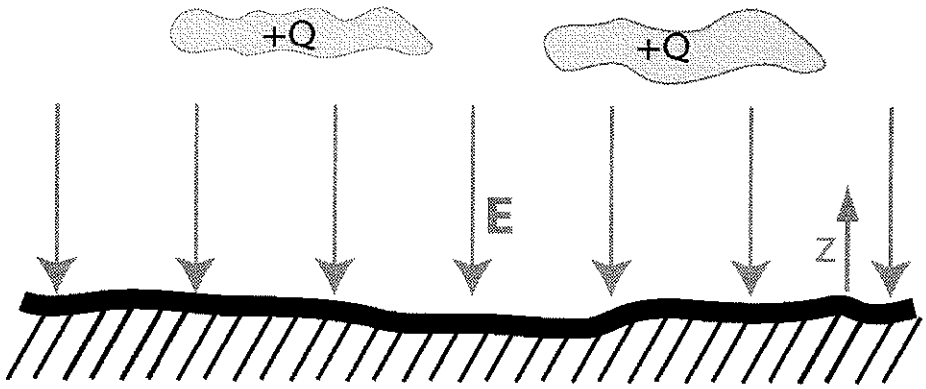

Figure 1 - 1: Environmental conditions, 200V/m<E<3MV/m.

1.2.2 Ambient Conditions

An interesting problem for real world electric field sensors is ionic charge or a "flux tube" under high voltage transmission lines. The transmission lines (AC and DC), often operate under corona conditions, whereby the high electric field at the surface of the conductor rips electrons off of atoms in the air, leaving positively charged air ions to interact with the environment. These ions float down towards the earth, charging dust and water molecules in the air.

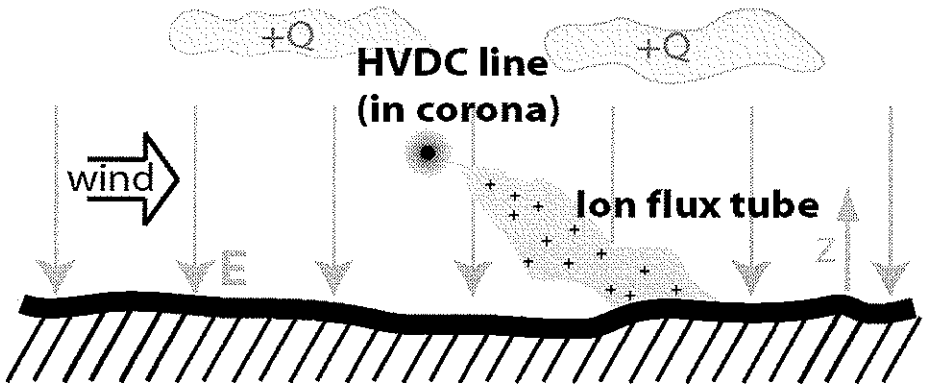

Figure 1 - 2: Ion flux tube generated by an HVDC line under corona.

> "A corona discharge is a self-sustaining, partial breakdown of a gas subjected to a highly divergent electric field such as that arising near [point sources]. In such an arrangement, the electric field, E_p at the corona point is considerably higher then elsewhere in the gap...
>
> When positive voltages are applied to the point, negative ions and electrons are accelerated towards the point while positive ions drift out of the ionization zone and flow through the drift zone towards the planer electrode."[2]

Although the ion current is of the order of nanoamps, it causes an electrostatic charge buildup on the surface of nearby insulators. Additionally, it reeks havoc on electronics, or charge sensitive induction probes, both of which require stable charge distributions (voltages and currents) over time.

1.2.3 Desired Improvements

Field mills (section 2.3) are predominantly used in atmospheric field measurement. However, these devices require the turning of an "earthed" chopper to modulate the DC field into an AC one. The problems with this design are that the chopper has to be rotated by a motor, and that excellent electrical contact is needed with the rotating shaft. In practice, field mills require relatively large amounts of power and frequent maintenance due to the gold filaments used wearing out quickly.

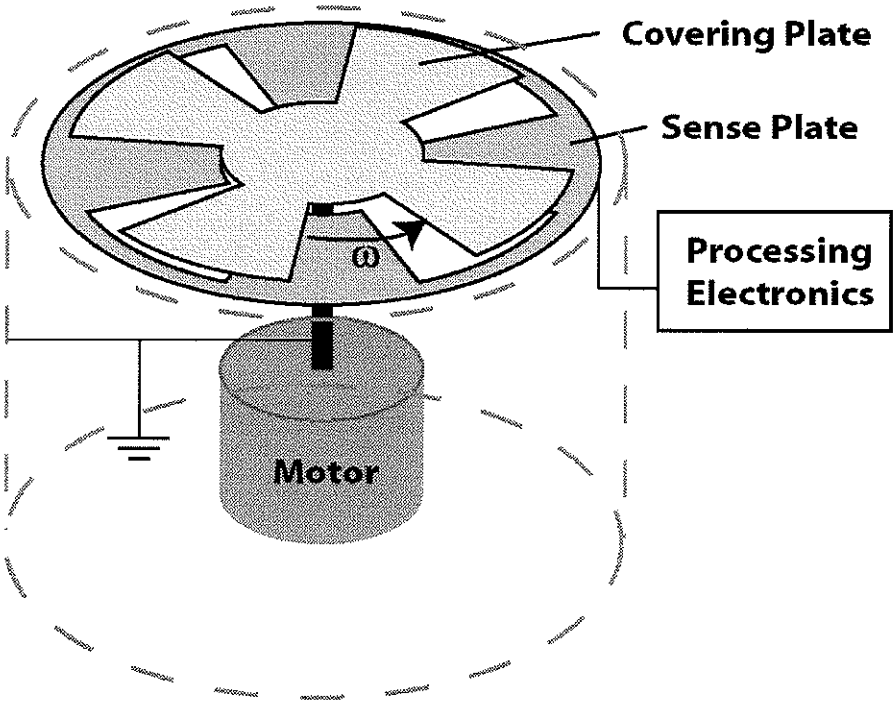

Figure 1 - 3: Basic field mill design.

In order to improve on existing field mill technology, this sensor should use minimal power, and require zero or minimal maintenance over a period of several months. Additionally to work outdoors, it must also be robust, withstanding dust, weather, insects, and animals.

1.3 DOCUMENT LAYOUT

The next three chapters of this document are designed to bring a novice reader up to speed on electrostatic sensing techniques (chapter 2), electrostatic and mechanical theory (chapter 3), micromachining (chapter 4). The subsequent chapters deal with design (chapter 5), measurement (chapter 6), and conclusions (chapters 7 and 8).

Chapter 2: FIELD MEASUREMENT TECHNIQUES

This chapter focuses on electromechanical field measurement techniques (induction probes, field mills, and vibrating field probes). Electro-optic sensors are briefly introduced, however they are less frequently used in the atmospheric field measurement industry. For further information on this topic, you should consult *Industrial Electrostatics* by Taylor and Secker or IEEE Standards 644 and 1308 [2,3,4].

2.1 ENVIRONMENT

In the real world, humidity, dust, debris, and insects all affect the operation of the electric field sensor. An interesting example is a spider's web being laid across the sensor surface [5]. The web can acquire its own charge and therefore bias the sensor quite significantly.

> "In order to make electric field measurements representing the unpeturbed field at a given location, the area should be free, as much as possible, from other power lines, towers, trees, fences, tall grass, or other irregularities. It is preferred that the location be relatively flat. It should be noted that the influence of vegetation on the electric field strength can be significant. In general, field enhancement occurs near the top of isolated vegetation and field attenuation occurs near the sides. The field peturbation can depend markedly on water content in the vegetation."[3]

Environmental concerns are not typically problems in a lab environment. However, they are defining criteria in successful industrial design. Thus, all electric field sensors and particularly micromachined ones need to address the sensor packaging and it's potential interaction with the environment.

2.2 INDUCTION PROBES

Induction probes are the basis of traditional electromechanical sensors. In these devices, high impedance op-amps are used to measure a change in the voltage between two capacitors caused by moving charge from one to the other (Figure 2 - 1). The top capacitor (C_1) is a sense plate whose surface charge mirrors that of the external field. As

charge is drawn from the bottom capacitor (C_2) to the top, the voltage across (C_2) changes $Q = CV$.

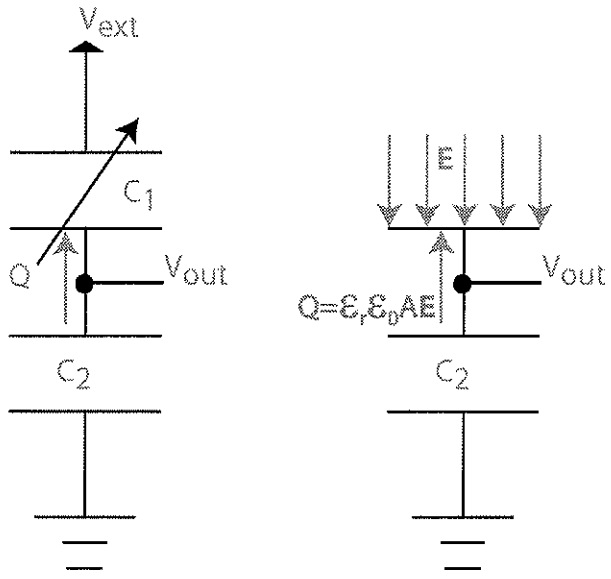

Figure 2 - 1: Induction probe model.

Mathematically, this is represented as:

$$Q = C_2 V_{out} \quad \text{C} \tag{2.1}$$

$$E_n = \frac{Q}{\varepsilon_r \varepsilon_0 A} \quad \text{V/m} \tag{2.2}$$

$$E_n = \frac{C_2}{\varepsilon_r \varepsilon_0 A} V_{out} \quad \text{V/m} \tag{2.3}$$

$$V_{out} = \frac{\varepsilon_r \varepsilon_0 A}{C_2} E_n \quad \text{V} \tag{2.4}$$

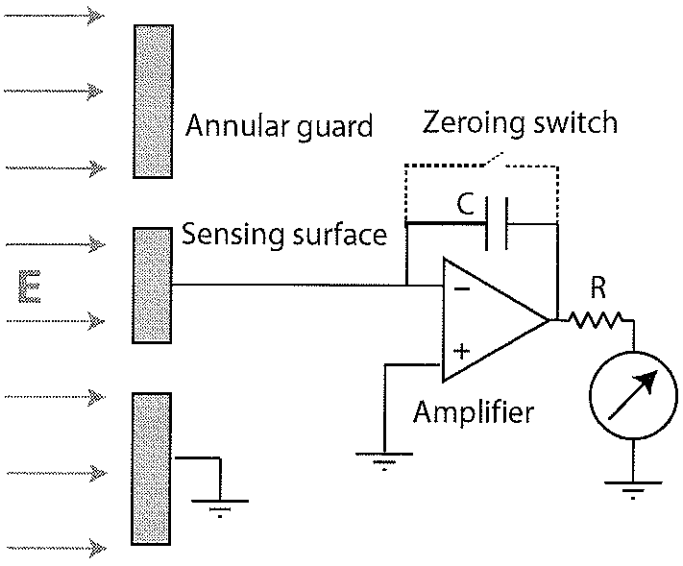

Figure 2 - 2: Induction probe with virtual earth amplifier [2].

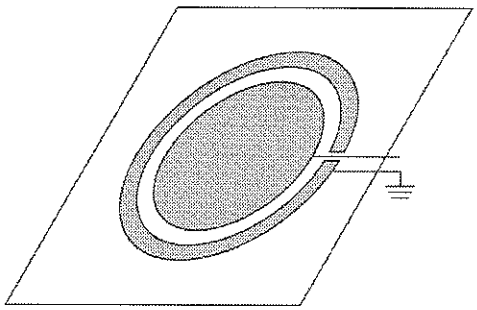

Figure 2 - 3: A PCB based sense electrode and annular guard [4].

Comprised of planer metal traces, a FET input op amp, and associated electronics -- induction probes are straightforward and easy to build. Unfortunately, this simplicity of design is marred by large drift. Bias currents into the op-amp, and ion flux landing on the sense plate, serve to cripple this sensors reliability.

2.3 FIELD MILLS

Field mills are an improvement over the traditional induction probe because they use mechanical motion to "mill" an electric field. The milling action, is obtained by

rotating an "earthed chopper" over the sense plate. This chopping action covers and uncovers the sense surface as seen in Figure 2 - 4 below. The resulting AC signal allows the field mill to ignore the DC bias effects seen in induction probes and affording it excellent long-term stability.

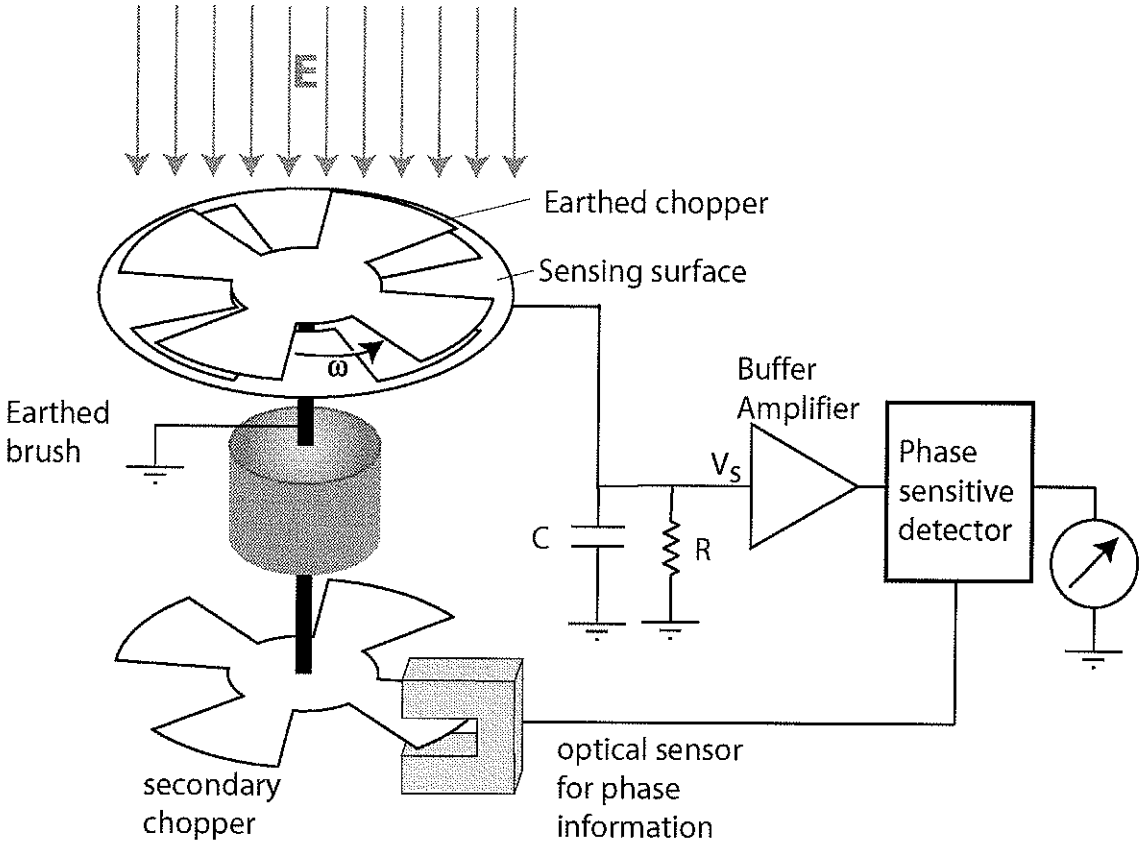

Figure 2 - 4: Basic field mill with electronics.

Summarizing the derivation in *Industrial Electrostatics* [2]:

As R $\rightarrow\infty$

$$\frac{dQ}{dt} = \pm(2\omega/\pi)\varepsilon_r\varepsilon_0 E_n A = i \quad \text{A} \tag{2.5}$$

For $\omega^2R^2C^2 >> \pi/48$

$$V_s = \varepsilon_r\varepsilon_0 E_n A/2C \quad \text{V} \tag{2.6}$$

Where,

V_s is the op-amp input voltage

$\frac{dQ}{dt} = i$ is the charge moving to and from the sense electrode

E_n is the normal field incident on the field mill

A is the sense electrode area

ω is the rotational speed of the chopper

C is the known capacitance of the system

Despite the output being independent of rotor frequency, the field mill is plagued by its own problems. Most noticeably, power consumption and "wear and tear". In the case of Manitoba Hydro, field mills and other test equipment are placed in remote locations for periods of several months. The one ampere power required to turn the field mill represents a significant hassle to field placement. Additionally, gold contacting wires are used on the rotor shaft to minimize electrical noise. These contacts wear out quickly (2-4 weeks) and need to be replaced by a field engineer [5].

2.4 VIBRATING FIELD PROBE

The vibrating field probe also works by converting mechanical motion into charge movement. In this device, the sense electrode is moved perpendicular to the aperture. This causes the system capacitance to change and an AC signal to be delivered to the induction probe.

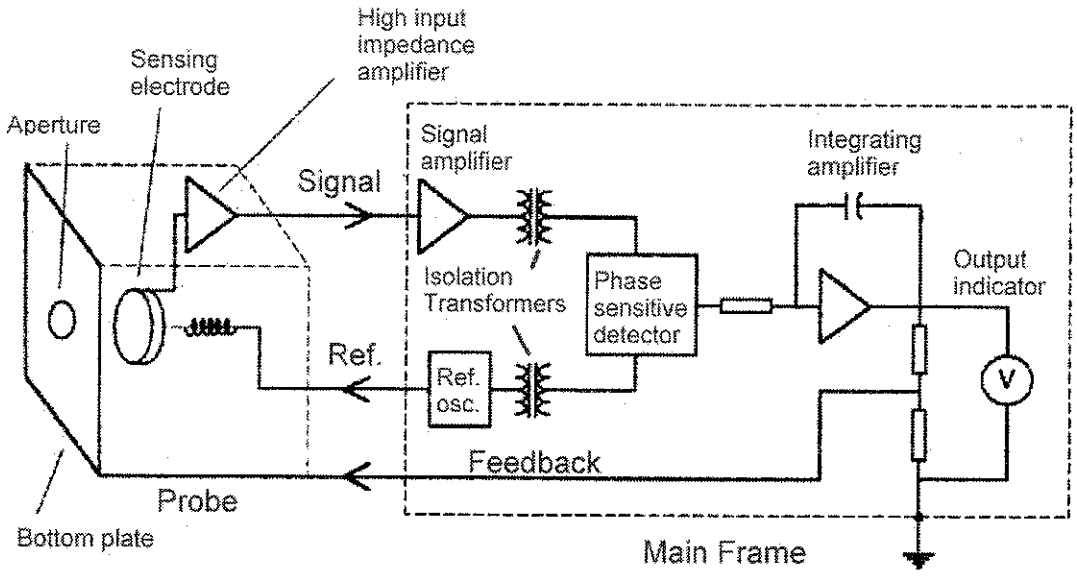

Figure 2 - 5: Schematic of a vibrating field probe [2].

Although more sensitive to dust and contamination, vibrating probe field meters are an alternative to rotating field mills when better spatial resolution is required.

2.5 ELECTRO-OPTIC METERS

Electro-optic meters work on Pockel (1st order) and Kerr (2nd order) effects in which the electric field changes the material properties and its refractive index.

> "The presence of such a field distorts the electron motions in the atoms or molecules of the substanc, or distorts the crystal structure resulting in changes in the optical properties... Typically changes in the refractive index are small." [6]

To measure electric fields, an optical beam is passed through a 45° polarizer, electro-optic cell, and another 45° polarizer. The signal is then compared to the intensity of a fully transmitted beam. Although an in-depth analysis of this measurement technique is beyond the scope of this thesis, electro-optic measurement is used in practice and the subject of many patents.

2.6 MICROMACHINED FIELD MILLS

In 2001 Mark Horenstien published his research in micromachined field mills. Using a lateral comb drive, he actuated a ground plane over a 10μm x 10μm square sense electrode with an exposed area of 5μm x10μm.

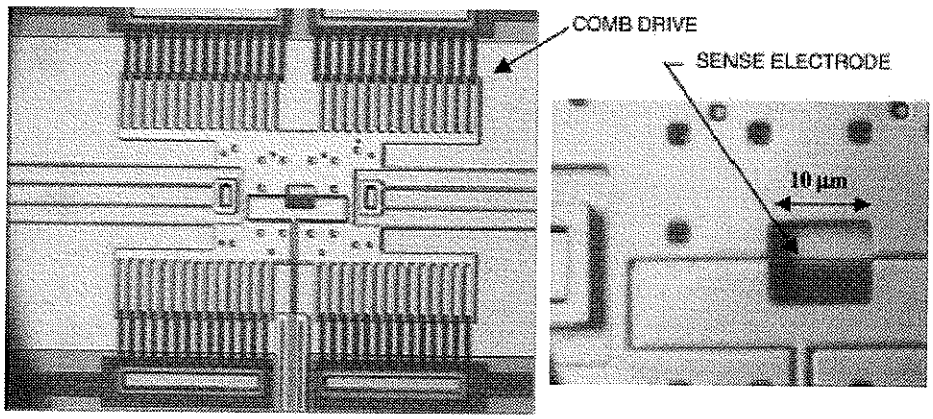

Figure 2 - 6: Microscope view of MEMS field mill. Left: shuttle mass, comb drives and folded beams. Right: close-up view of 10μm by 10μm aperture and sense electrode. [7].

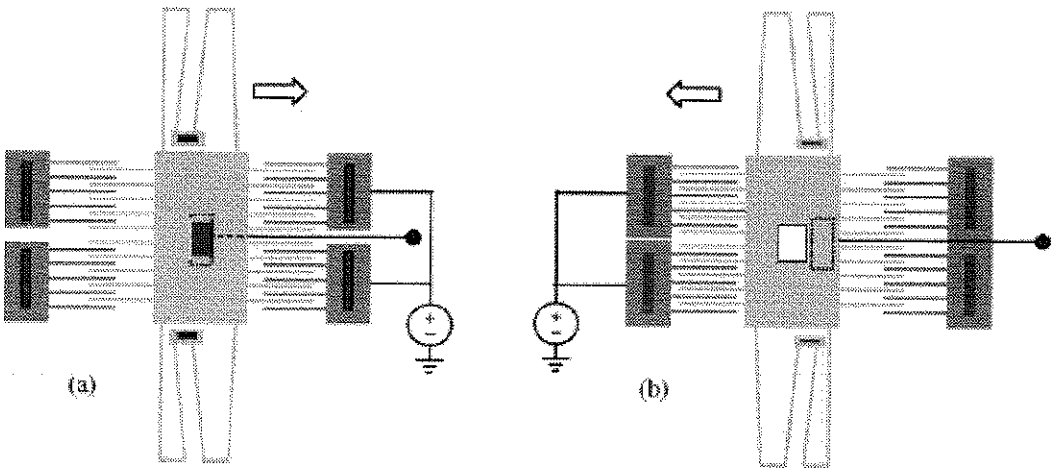

Figure 2 - 7: Transverse motion of field mill covering plate [7].

Horenstien's paper [7] demonstrates a successful micromachined electric field mill that has a sensitivity of about 35 V per kV/m. The device is constructed from 2 layers of surface micromachined polysilicon placed on a silicon substrate. The comb drive moves a 10μm x 10μm aperture side to side, exposing a 5μm x 10μm section of the underlying 10μm x80μm sense electrode. Interestingly, by using the voltage squared actuation properties of the comb drive and its symmetry, the actuating electric field can be filtered out by using a 8^{th} order high pass filter.

Professor Muller at the University of Berkley has also been involved in developing micromachined field mills for the past 15 years. His graduate students Hsu and Riehl built comb drive based electrometers. In 1990, Hsu [8] built and tested a discrete lateral comb drive based electrometer the sensitivity of which is described as:

"The sensed signal starts emerging from the parasitic feedthrough and background noise if the test surface is above 20V (with an electrode offset of 0.2mm). The [electrostatic voltmeter] response is about 15μV per volt change of the surface under measurement." [8]

Riehl [9] built an integrated coulomb meter and electrostatic field meter using the Analog Devices modMEMS technique. For the electrostatic fieldmeter, his resolution was 630V/m.

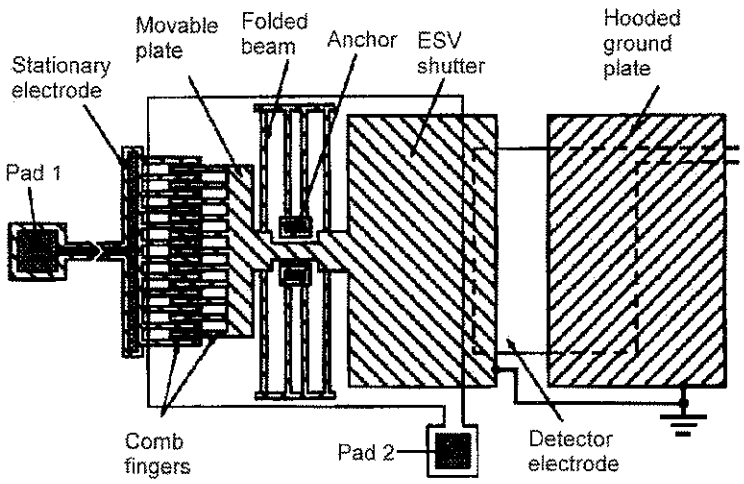

Figure 2 - 8: Micromachined electrostatic voltmeter [8], top view.

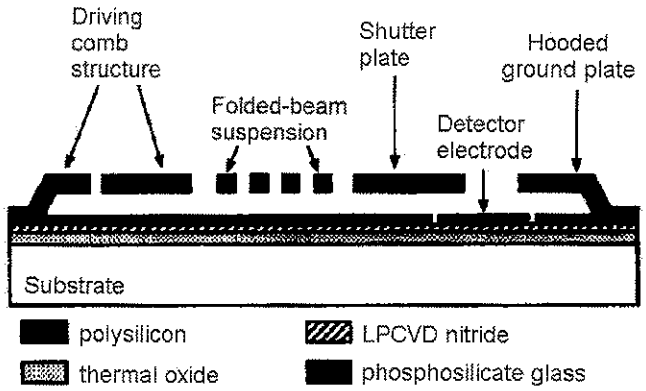

Figure 2 - 9: Micromachined electrostatic voltmeter [8], side view.

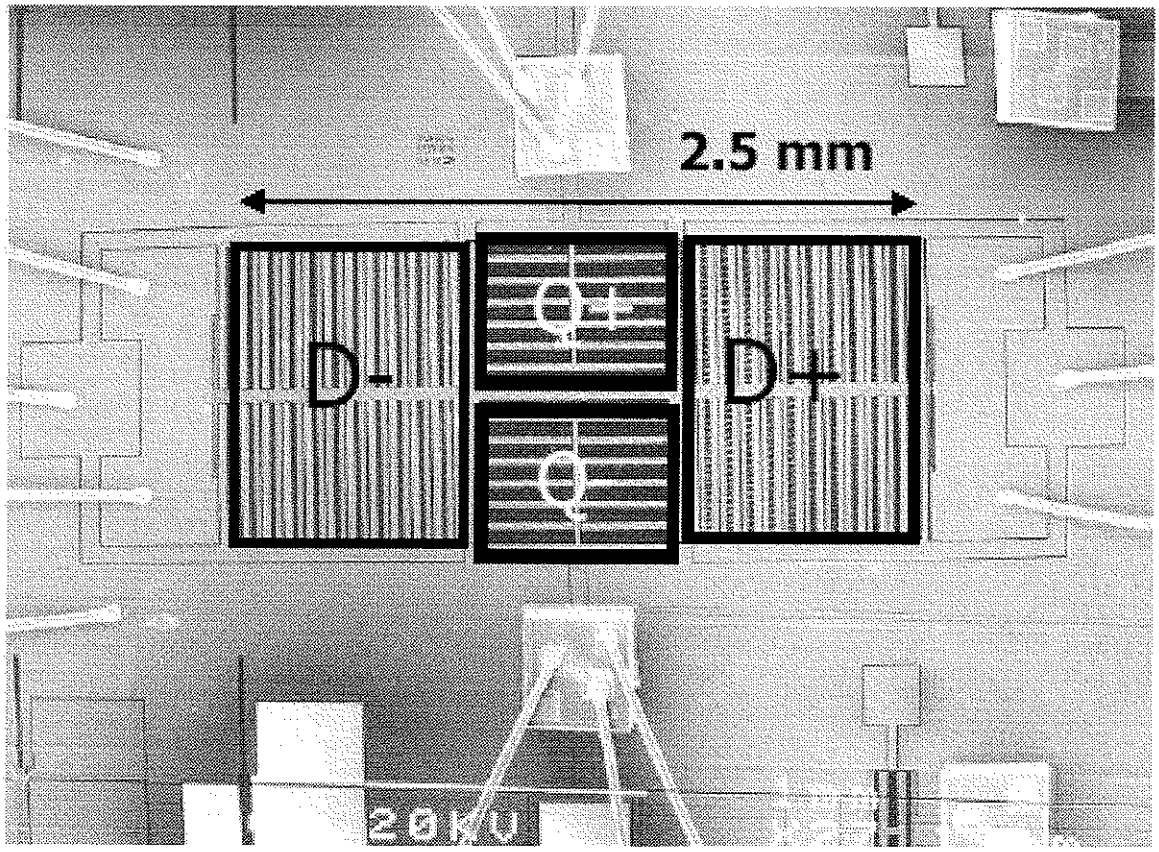

Figure 2 - 10: SEM of a micromachined electrometer resonator [9].

Chapter 3: THEORY

This chapter will review the basic electrostatic and mechanical theory required for this thesis. For more comprehensive works see *Engineering Electromagnetics* by Hayt [10] or *Industrial Electrostatics* by Taylor [2] or *Roark's Formulas for Stress and Strain* by Young [11]. *Engineering Electromagnetics* is an excellent introductory text, whereas *Industrial Electrostatics* focuses on practical measurement techniques. *Roark's Formulas for Stress and Strain* is a comprehensive work tabulating many useful mechanical deflection and deformation formulas.

3.1 ELECTROMAGNETIC FIELD THEORY

In 1785, Coulomb postulated that the force between two charged bodies was proportional to the magnitude of charges and the square of the distance between them. Today, this is known as Coulombs law, where $\mathbf{a}_r$ is a unit vector along the axis between the two charges.

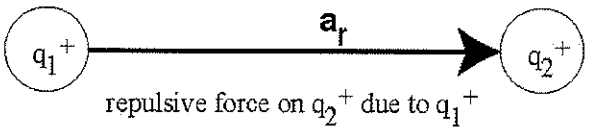

Figure 3 - 1: Repulsive forces between positively charged particles.

$$\mathbf{F} = \frac{q_1 q_2}{4\pi\varepsilon_r\varepsilon_o r^2}\mathbf{a}_r \quad \text{N} \tag{3.1}$$

$$\varepsilon_o = \frac{1}{4\pi}10^{-9} = 8.85\times10^{-12} \quad \text{F/m} \tag{3.2}$$

The electric field is simply a region of space in which the forces between electric charges interact. In defining an electric field, we assume that a positive unit test charge q_2 exist in the field and does not alter the existing field. The force exerted on this hypothetical charge is the electric field. Thus, equation 3.1 reduces to:

$$\mathbf{E} = \frac{\mathbf{F}}{q_2} = \frac{q_1}{4\pi\varepsilon_r\varepsilon_o r^2}\mathbf{a}_r \quad \text{N/C} \tag{3.3}$$

Field lines are a graphical representation of the path a hypothetical test charge would take through the electric field if it had no mass or momentum. As like charges repel, a positive test charge would move away from positive charges towards negative ones. These paths do not cross and are generally drawn such that their density is proportional to the relative field strength.

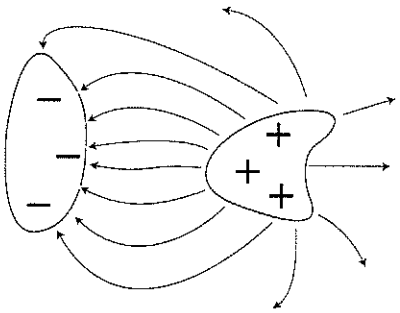

Figure 3 - 2: Example of electric field lines.

Being a conservative field, the mechanical work energy used to move a charge around is path independent. As the charge Q is moved from A to B, the potential energy gained or lost is given by:

$$W_{AB} = -Q\int_A^B \mathbf{E} \bullet d\mathbf{L} \quad \text{J} \tag{3.4}$$

Where $\mathbf{E} \bullet d\mathbf{L}$is the dot product of the electric field and an incremental distance along the path of the charge Q.

Potential energy is the work required to bring a unit charge from infinity to its current location. More commonly, we use voltage as a measure of the potential difference between two points.

$$V_{AB} = -\int_A^B \mathbf{E} \bullet d\mathbf{L} \quad \text{J/C or V} \tag{3.5}$$

Going beyond consideration of individual point charges, we have:

$$\mathbf{E} = -\nabla V \quad \text{N/C or V/m} \tag{3.6}$$

And W_e is the electrical work energy required to create a charge distribution.

$$W_e = \frac{1}{2}\int_{vol}(\mathbf{D}\bullet\mathbf{E})dv = \frac{1}{2}\int_{vol}\varepsilon\left(\mathbf{E}\bullet\mathbf{E}^*\right)dv = \frac{1}{2}\int_{vol}\varepsilon E^2 dv \quad \text{J} \tag{3.7}$$

Where;

$\mathbf{E}$= electric field vector in space	$\mathbf{D} = \varepsilon_r\varepsilon_0\mathbf{E}$
$\nabla a = \frac{\partial a}{\partial x} + \frac{\partial a}{\partial y} + \frac{\partial a}{\partial z}$	$\varepsilon = \varepsilon_r\varepsilon_0$
V = scalar potential	ε_r= relative dielectric constant
W_e= electrical work energy	ε_0= permittivity of free space

Finally, the negative gradient of the work energy of an electric field is the force it exerts on a charged body. Thus, we can use force based measurement techniques to determine the magnitude of an electric field.

$$\mathbf{F} = -\nabla W_e \quad \text{N or J/m} \tag{3.8}$$

Complete derivations can be found in both Hayt [10] and Cheng [12].

3.1.1 Force Derivation

Modeling the system as a parallel plate capacitor (neglecting fringing) [13], we can simplify equation 3.8 and determine a simple field to force relationship (equation 3.12).

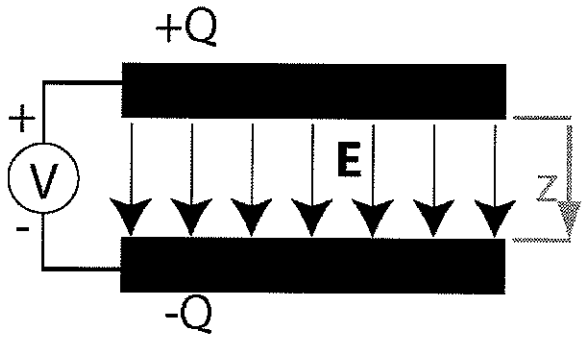

Figure 3 - 3: Parallel plate capacitor model.

The energy stored in a capacitive system is given as:

$$W_e = \frac{1}{2}CV^2 = \frac{1}{2}\frac{\varepsilon A}{z}(E_z z)^2 = \frac{1}{2}\varepsilon A E_z^2 z \quad \text{J} \tag{3.9}$$

Expanding out equation 3.8 with a uniform electric field in the z direction gives:

$$\mathbf{F} = -\nabla W_e = -\frac{\partial W_e}{\partial x}\mathbf{a}_x - \frac{\partial W_e}{\partial y}\mathbf{a}_y - \frac{\partial W_e}{\partial z}\mathbf{a}_z \quad \text{N} \tag{3.10}$$

$$\mathbf{F} = -\nabla W_e = 0\mathbf{a}_x - 0\mathbf{a}_y - \frac{\partial\left(\frac{1}{2}\varepsilon A E_z^2 z\right)}{\partial z}\mathbf{a}_z \quad \text{N} \tag{3.11}$$

Thus, as a simple relationship between field and force, we obtain.

$$F_z = -\frac{1}{2}\varepsilon A E_z^2 \quad \text{N} \tag{3.12}$$

Where F_z is a repulsive force between two positively charged bodies.

Generalizing this model to a charge distribution and its induced mirror image, we have:

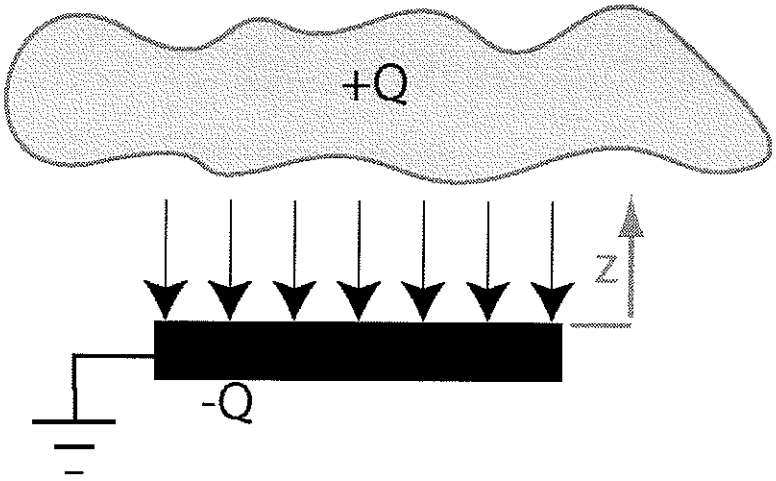

Figure 3 - 4: Earthed plate lying in an electric field.

$$F_e = \frac{1}{2}\varepsilon A E_z^2 \mathbf{a}_z \quad \text{N} \tag{3.13}$$

Where equation 3.13 and 3.12 are equivalent equations for the electric field force (F_e) in the z-direction ($\mathbf{a}_z$). And the sign change (in 3.13) from equation 3.12 is due to reversing the axis direction.

Using this induced charge model, we will be testing the sensor under AC, DC, and AC+DC conditions (Figure 3 - 5). Using the voltage and parallel plate capacitor relationships in equations 3.14 and 3.15 respectively, we obtain a usable force to voltage relationship in equation 3.16.

$$V = V_{dc} + V_{ac} \quad \text{V} \tag{3.14}$$

$$E_z = \frac{V}{z} \quad \text{V/m} \tag{3.15}$$

giving the relationship:

$$F_z = \frac{1}{2}\varepsilon A\left(\frac{V}{z}\right)^2 = \frac{1}{2}\varepsilon A\left(\frac{V_{DC}^2 + 2V_{DC}V_{AC} + V_{AC}^2}{z^2}\right) \quad \text{N} \tag{3.16}$$

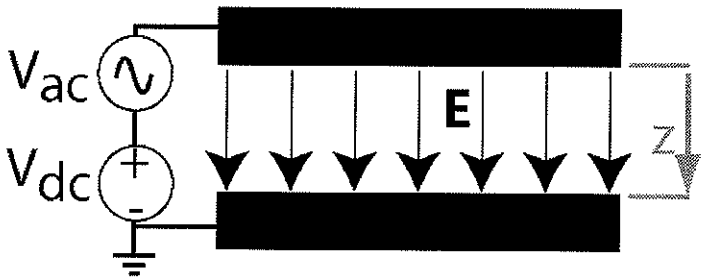

Figure 3 - 5: Parallel plate capacitor model with an AC signal and DC bias.

3.2 MECHANICAL THEORY

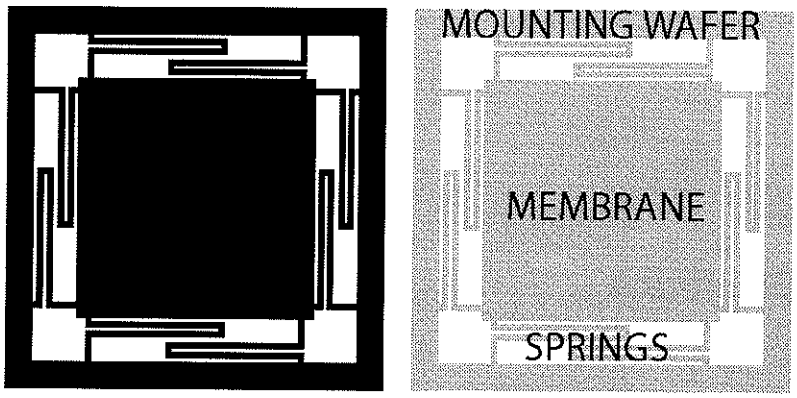

Figure 3 - 6: Transducer layout.

The two main mechanical problems considered in this design were the spring mechanics, and force equilibrium. The common equations used in MEMS literature will be presented here. However as explained in section 5.2, internal stress created during thermal evaporation (section 4.4) dominated the design, causing the spring beams to curl up about 180° significantly changing the spring dynamics as shown in Figure 3 - 7 below, and so the observed shape cannot be modeled by cantilever spring equations. With this in mind, characterization of the spring constants and deflection will be addressed by measurement in section 6.3.

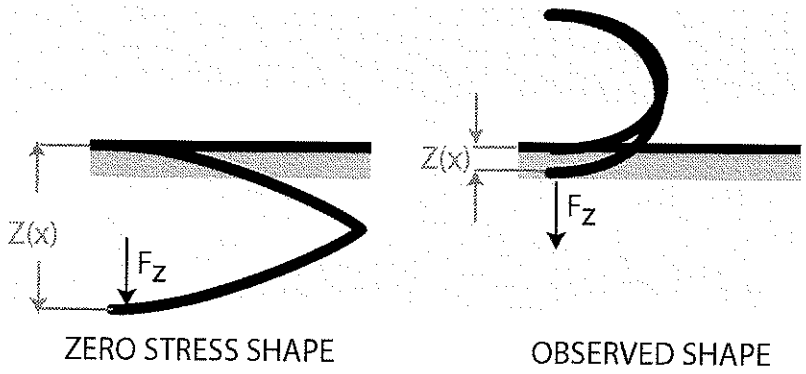

Figure 3 - 7: Theoretical and observed spring shape.

Using the zero stress shape, we can examine the forces involved in the membrane deflection and predict a useful spring geometry. The simplified model consists of a series/parallel combination of cantilever beams (zero stress). Each spring is constructed from five sections, two main beams and 3 short connecting segments. From which, we extract a series combination of the two main cantilever sections (beams 2 and 4).

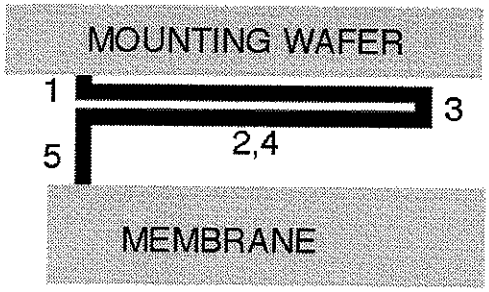

Figure 3 - 8: Spring layout.

The membrane is held up by two springs on each corner resulting in 8 parallel beams as shown in Figure 3 - 6. By using this symmetry in the spring placement we hope to create symmetry in the lateral forces on the membrane, allowing the springs to have a "guided" end condition. Thus allowing us to focus solely on the vertical motion.

In the three test cases, the main beams (2 and 4 in Figure 3 - 8 above) have lengths of 2.1 mm, 1.4mm, and 0.7mm as determined by work in iteration number 2 (section 5.2.1). Because these main beams are longer then the cross beams (700μm:282μm for

beams 2 and 5 respectively) for the shortest case, we will neglect the curvature of the shorter sections [1, 11, 14, 15, 16].

The simple (fixed-free) cantilever model and equation [1] for these beams is given in Figure 3 - 9 and equation 3.17 below.

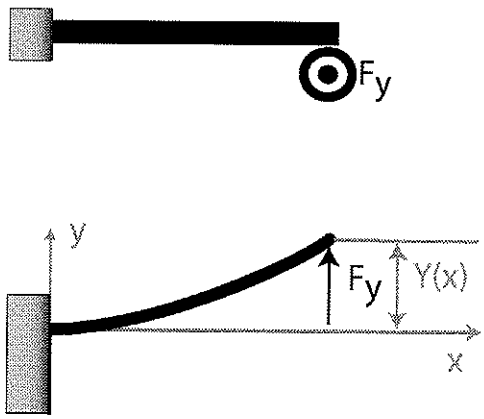

Figure 3 - 9: Deflection of an end loaded fixed-free rectangular beam.

$$Y(x) = \frac{F_y}{6E_{Young's}I}(3x^2L - x^3) \quad \text{m} \tag{3.17}$$

Where, the moment of inertia for a beam with rectangular cross-section is given by:

$$I = \frac{1}{12}wt^3 \quad \text{m}^4 \tag{3.18}$$

and

$Y(x)$ = vertical deflection
F_y = y directed applied force
$E_{Young's}$=Young's modulus
L = total beam length
x = distance from the fixed end
t = thickness of the beam
w = width of the beam
I = moment of inertia

At x=L, equation 3.17 solves to:

$$Y(x = L) = \frac{12F}{6E_{Young's}wt^3}(2L^3) = \frac{4FL^3}{E_{Young's}wt^3} \quad \text{m} \tag{3.19}$$

Rearranging to acquire the force, we have:

$$F(x = L) = \frac{E_{Young's} w t^3}{4L^3} Y \tag{3.20}$$

Continuing with the theoretical model, the use of two equal cantilever beams allows the curvature and deflection of each beam to cancel out. Thus, the fixed and guided endpoints of the spring remain in plane with each other (Figure 3 - 10). The midpoint is free to move giving us the series fixed-free cantilever approximation which is twice that of a single cantilever beam (Figure 3 - 10).

$$Y(x,\ 2 \text{ beams in series}) = 2 * \frac{F_y}{6E_{Young's} I}(3x^2L - x^3) \quad \text{m} \tag{3.21}$$

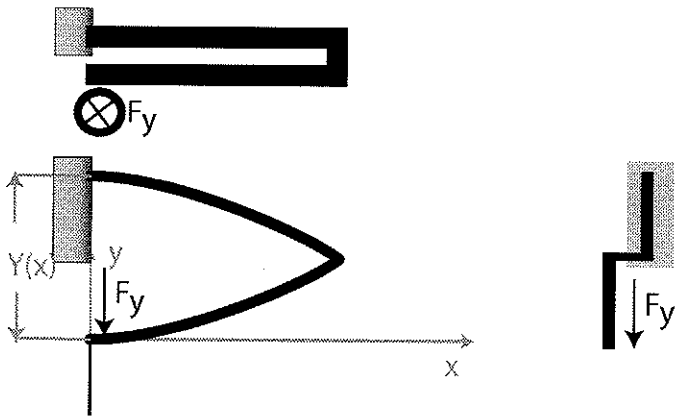

Figure 3 - 10: Cantilever beams in series.

Adding springs in parallel with this makes the system more ridged, raising its effective spring constant. Considering our target system of 8 parallel with 2 beams each, we obtain:

$$Y(x,8 \text{ springs}) = \frac{2}{8} * \frac{F_y}{6E_{Young's} I}(3x^2L - x^3) \quad \text{m} \tag{3.22}$$

Rearranging the theoretical model to obtain the spring force of the system we have:

$$F_m = -kz = -\left(\frac{N_{parallel}}{N_{series}}\right)\left(\frac{1}{4}\frac{E_{Young's}wt^3}{L^3}\right)z\mathbf{a}_z \quad \text{N} \tag{3.23}$$

Where F_m is the mechanical restoring force of the spring.

Chapter 4: MICROMACHINING

This chapter covers the stages of device fabrication from wafer preparation to the release etch. Each topic is addressed sequentially in the order of operations performed as shown in Figure 4 - 2 below.

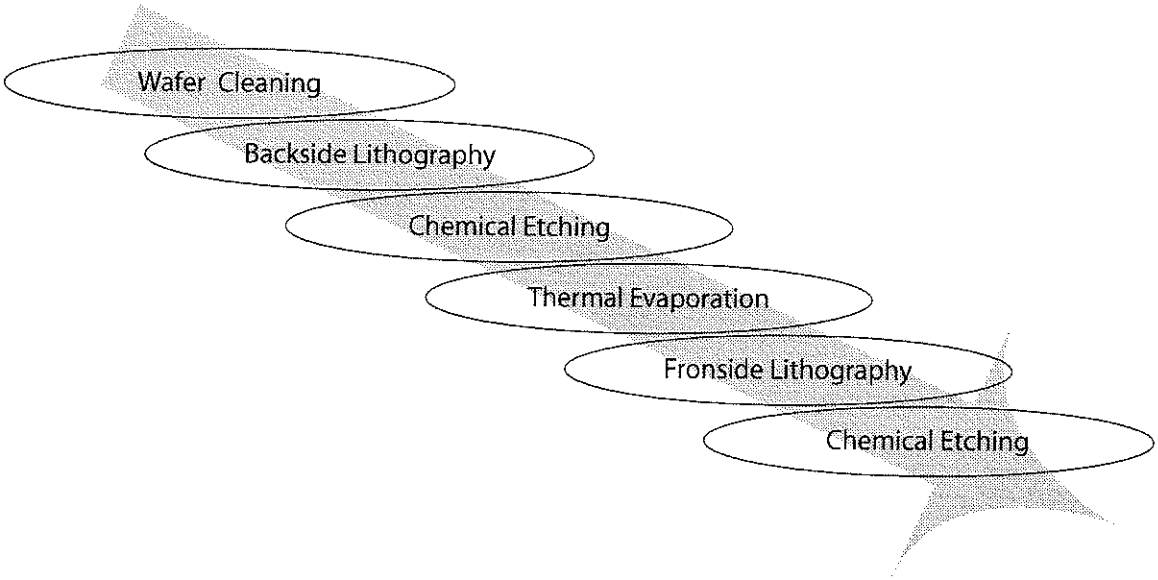

Figure 4 - 1: Micromachining processing steps.

4.1 WAFER CLEANING

In microelectromechanical system and integrated circuit manufacturing, proper cleaning and preparation of the wafer surface is required to minimize defects and allow for proper adhesion of materials. Most of this process is done at the factory, with both test and prime* wafers. During wafer in-house processing, prevention is the key tool in minimizing defects. Thus, the majority of wafer handling is performed in a class 1000 clean room†.

---

* Test wafers are seconds in the manufacture of prime wafers. They have more atomic defects and a wider range of resistance. These seconds are generally used for pre-production testing.
† Class 1000 clean room has less then 1000-0.5μm particles per cubic foot.

For test wafers, rinsing with de-ionized water and drying with nitrogen (optional) may be required to remove dust. However, hard (quartz) particulate matter may actually scratch the surface creating more defects in the final structure.

4.1.1 Piranha Etch

To remove any organic residue on the wafer and ensure good adhesion of the metal layers, a piranha etch is required. An acid piranha etch consists of 3 parts sulfuric acid and 1 part hydrogen peroxide. At which time, the mixture will violently dissolves any organic material on the wafer. When complete (no bubbles), the wafer is put through a triple rinse of de-ionized water and nitrogen stream drying.

Note: Because of the explosive potential of this reaction with organic material, Piranha etches are only to be handled by well-trained and alert personnel. Once cooled the mixture is still a pH1 sulfuric acid.

4.2 Backside Lithography

Optical lithography [17] is the process by which light is used to pattern small features in photoresist. For the design in this thesis, both front and backside lithography were performed. The backside processing was done before the copper deposition because KOH (potassium hydroxide) also dissolves evaporated aluminum [18]. Lithography on the front side of the wafer was performed after deposition of both the aluminum (adhesion) layer and the copper layer.

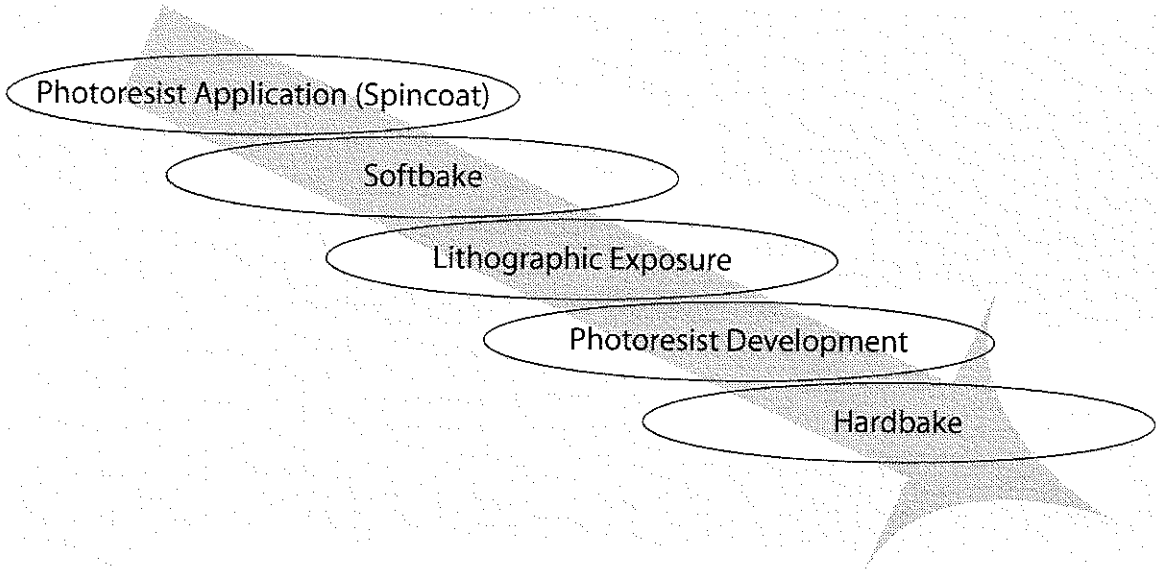

Figure 4 - 2: Lithography processing steps.

4.2.1 Photoresist Application

Positive photoresist (Olin Hunt HPR 506) was used in the fabrication of this design. During proper application, the wafer is mounted on a vacuum chuck, and covered with a large drop of photoresist. The wafer is then spun at 3000 RPM for 30 seconds, to thin the resist down to a uniform thickness (viscosity controlled).

4.2.2 Softbake

After photoresist deposition, the wafer is immediately placed on a hotplate (110°C) for 1 minute. This stage congeals the photoresist in preparation for use under the contact mask during lithography.

4.2.3 Lithographic Exposure

At this stage, the wafer is meticulously aligned with the mask. This alignment is a critical step both to align the current mask with the crystal geometry and to allow alignment of subsequent mask features. Alignment with the crystal geometry is important, because the KOH etchant used during the next step is anisotropic and preferentially etches along the crystal grain.

Once aligned, the mask is contacted (ink side down) with the photoresist. The mask ink blocks UV light from reaching the photoresist, thereby allowing it to be patterned. Figure 4 - 3 and Figure 4 - 4 below demonstrate this process. UV light passes through the clear Mylar film (used in linotronic printing). Where the ink is missing, light passes through, exposing the photoresist.

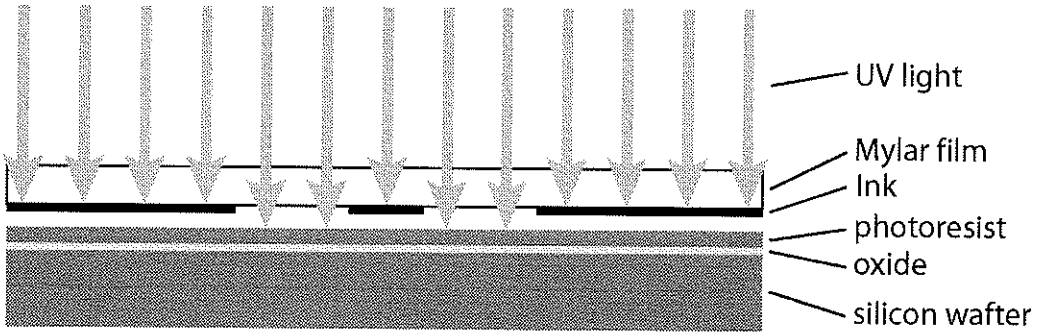

Figure 4 - 3: Schematic of an optical lithographic contact mask during UV exposure.

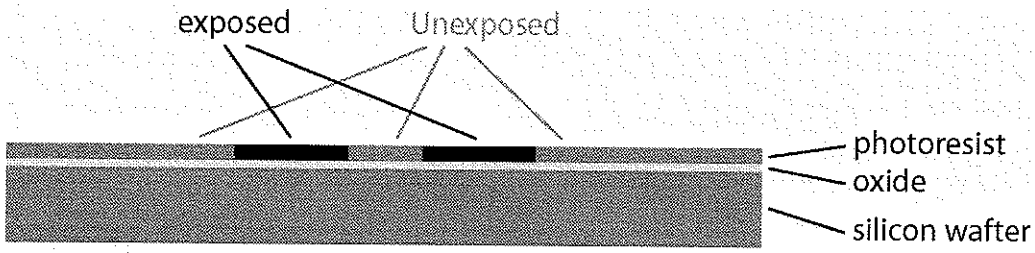

Figure 4 - 4: Photoresist condition after UV exposure.

4.2.4 PHOTORESIST DEVELOPMENT

During photoresist development, a complementary chemical is used to dissolve the exposed positive photoresist. During this process, the developer solution needs to be mixed to ensure even distribution of active solvent. Incomplete development may lead to the problems observed in chapter 6 where features remain attached or poorly defined.

4.2.5 HARDBAKE

Once developing is complete, a final hardbake is done to drive off all the solvents from the photoresist. Once complete, the wafer can be left for weeks without damage to the lithographic pattern. This hardbake is done at 120°C for 30 minutes.

4.3 BACKSIDE ETCHING

Backside processing of the silicon wafer is done to allow through wafer features without completely compromising the wafers structural integrity. In this step, sections of the wafer are thinned to 30μm in preparation for the frontside feature etching.

Backside etching consists of a 10:1 Buffered Oxide Etch (BOE) etch and a Potassium Hydroxide (KOH) etch. These dissolve first the oxide (Figure 4 - 5), then the wafer (Figure 4 - 6). For the BOE etch photoresist works as the mask. While for the KOH etch, the unetched oxide is used. KOH etching is done at 80°C giving it an etch rate of 1μm/minute.

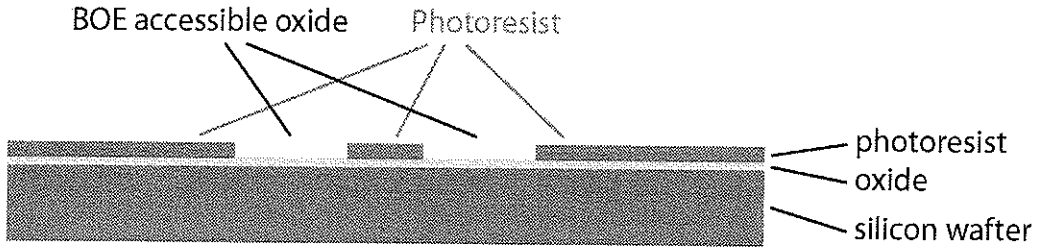

Figure 4 - 5: BOE etching of the oxide.

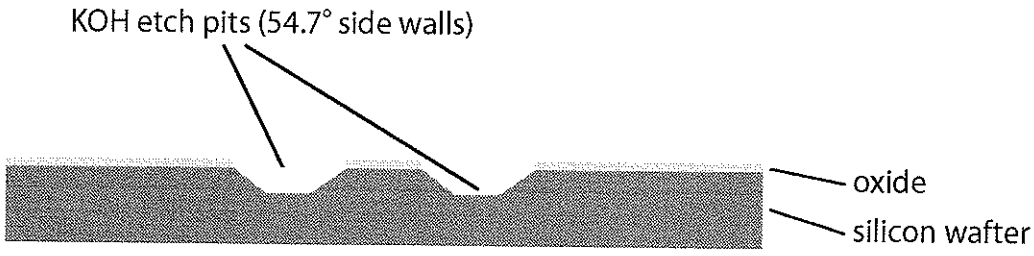

Figure 4 - 6: KOH backside etch.

4.4 THERMAL EVAPORATION

In thermal evaporation, metals and certain insulators are atomically deposited on a substrate. In this process, the target metal is placed on a tungsten boat or rod. Several hundred amps are passed through the tungsten boat, causing it to become white hot. This heat evaporates (liquid to gas, copper) or sublimes (solid to gas, chrome and aluminum) the target metal into a gas (see Figure 4 - 7, below).

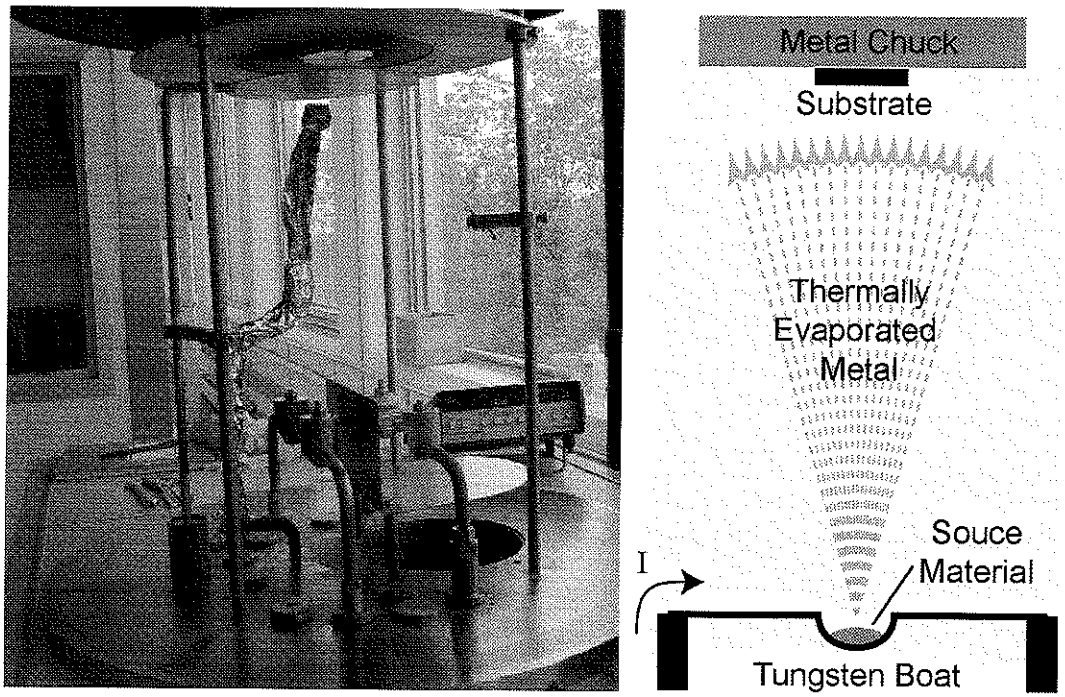

Figure 4 - 7: Thermal evaporator layout.

By controlling the amount of current through the tungsten rod/boat, we can maintain the rate of deposition around 20 $\overset{0}{A}$ per second onto the wafer. The picture in Figure 4 - 7, shows a thermal evaporator with two evaporation terminals. Typically one (left) is used for chrome or aluminum adhesion layers, while the other (right) is used for evaporating the bulk material.

When performing thermal evaporation, film quality is determined by the deposition rate, vacuum quality ($<10^{-6}$ torr)*, and organic debris in the system. This step is relatively easy, but does require diligence.

4.5 FRONTSIDE LITHOGRAPHY AND ETCHING

Frontside lithography is done in the same manner as the backside. The copper coated side is covered with photoresist, exposed to UV light, and developed. During chemical processing, the copper is removed using a commercially available "Chrome etch". Once complete, the mixture is washed and BOE used to break through the aluminum adhesion layer and underlying oxide Figure 4 - 8d below.

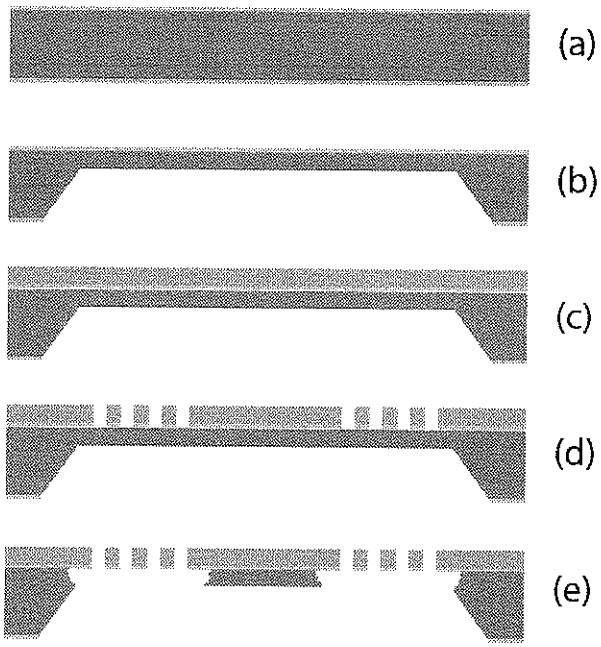

Figure 4 - 8: Summary of processing steps: (a) initial wafer, (b) backside KOH etch, (c) thermal evaporation, (d) copper and a 10:1 BOE etch, (e) XeF_2 release etch.

* The deposition rate needs to be much larger then the absorption rate which depends on the vacuum quality.

4.6 XENON DIFLUORIDE XeF_2

The final step in processing is the xenon difluoride (XeF_2) release etch Figure 4 - 8e above. XeF_2 is an isotropic dry (gas) etchant passes through the features etched in Figure 4 - 8d. The gas is highly selective, attacking the silicon while leaving the metals intact. Being isotropic, the XeF_2 etches a semicircular shape around the topside holes seen in Figure 4 - 8e.

Care during the final stages of the XeF_2 etching is very important, most fabricated devices fail during the N_2 purges at the end. This is because the devices are fully released and the N_2 gas creates differential pressures, which rip micro-springs apart quite easily.

XeF_2 etching starts with placement of the sample in the etching chamber. Once placed in the system and sealed, the following cycle is performed. All valve references (1,2,3,4) refer to Figure 4 - 9: XeF_2 etching system.

1. Purge with nitrogen (2 is closed for all steps)
   - Bring down pressure (4 and 3 open / 1 closed)
   - Flood with nitrogen (1and 3 open / 4 closed)
   - Repeat 4 to 5 times
2. XeF_2 etch (1 is closed for all steps)
   - Pump out the etching chamber (4 open / 2 and 3 closed)
   - prepare XeF_2 (2 open /1, 3, and 4 closed)
   - Wait 30 seconds
   - Close all (2,3, and 4 closed)
   - Expand XeF_2 into etching chamber (3 open, 2 and 4 closed)
   - Wait 90 seconds
   - Close all (2,3, and 4 closed)
   - Repeat until the device is released (approximately 2 hours)
3. Nitrogen Purge and return to atmosphere (2 is closed for all steps)
   - Close all (1, 2,3, and 4 closed)

- Open path to etching chamber (3 open)
- **Crack** N_2 control valve (1 open)
- Allow pressure to rise **SLOWLY so as not to damage your devices**
- Purge (3 and 4 open, 1 closed)
- Repeat several times at low pressure to remove the remaining XeF_2 and prevent poisonous HF gas from forming

4. Bring the system up to atmosphere
   - Close valve 4, open 1 and 3, slowly increase chamber pressure
   - When the etching chamber reaches atmosphere, open and remove your device

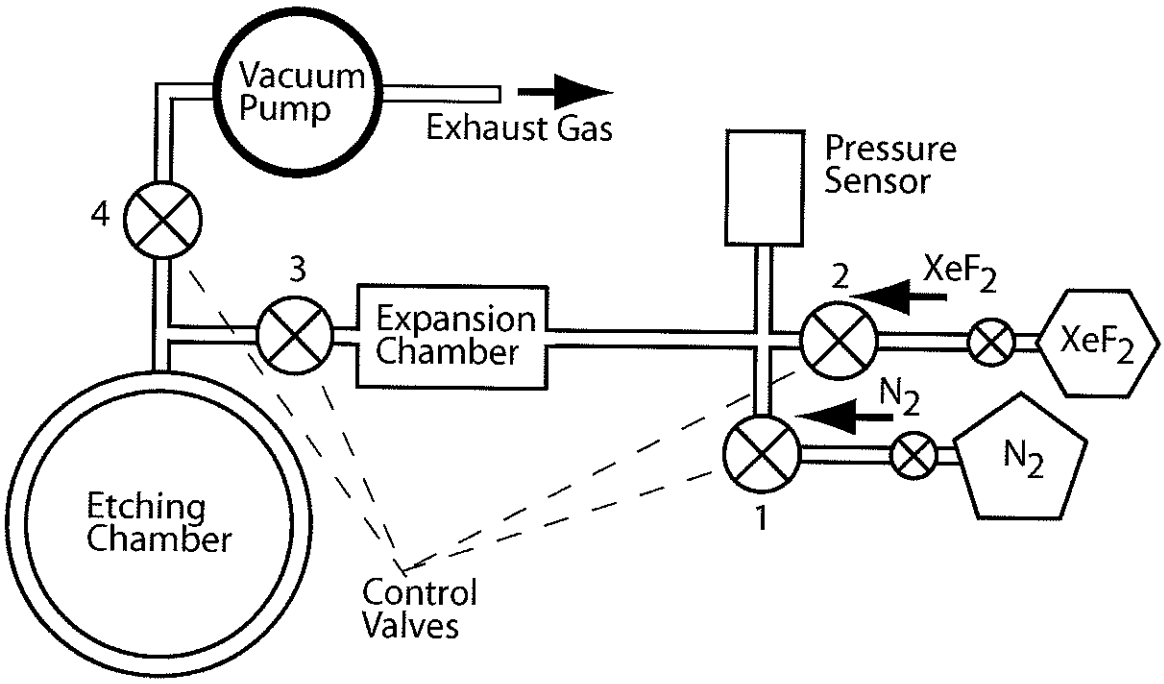

Figure 4 - 9: XeF_2 etching system.

Chapter 5: SENSOR DESIGN

5.1 SENSOR CONCEPT

This sensor detects electrostatic fields by optically observing the deflection of a 500μg membrane (equation 5.1) due to electrostatic attraction. During measurement the copper membrane deflects a laser beam off its surface into a quad-cell photodiode. As the membrane moves up and down, the reflected beam translates across the detector's surface ΔS creating a differential signal between quadrants (Figure 5 - 1).

Copper was selected as the membrane surface because of good conduction characteristics and availability. However, using copper on a silicon substrate requires the addition of an adhesion layer (chrome or copper). As an adhesion layer, Chrome provides good adhesion but unfortunately, "chrome etch" preferentially dissolves copper. Conversely, aluminum provides moderate adhesion (deposited at <10-6 torr) and the "10:1 BOE etch" reacts minimally with the copper. Thus for the final design (#3), the metal layers comprised of a 10nm aluminum adhesion layer and 1μm of copper.

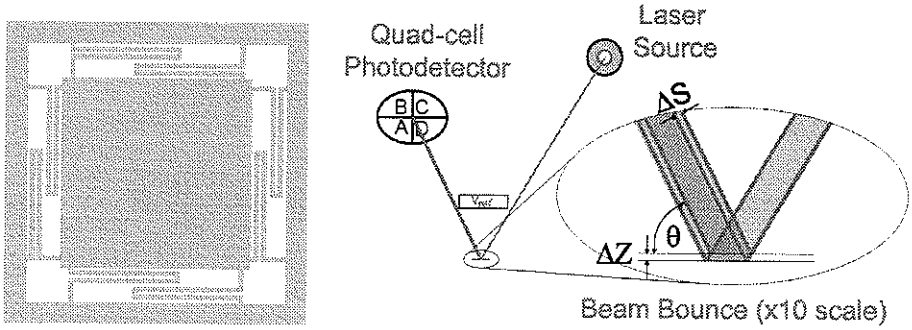

Figure 5 - 1: Membrane mounting (left) and sensor optical geometry (right).

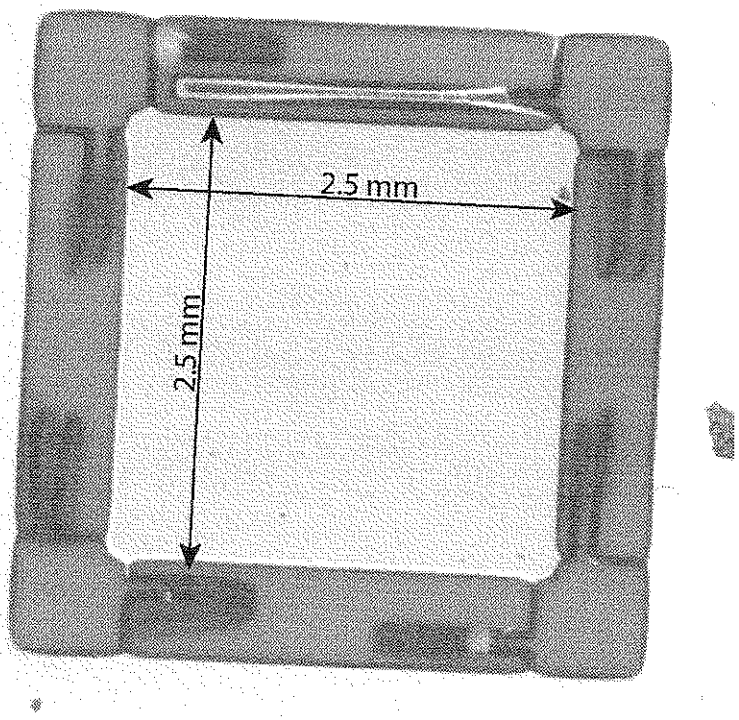

Figure 5 - 2: Completed membrane supported by eight folded beam springs (each beam 2.1mm in length).

5.2 TRANSDUCER DESIGN

The transducer consists of a 2.5mm x 2.5mm central membrane held up by eight 70 μm wide springs, constructed from 10nm of aluminum and 1μm of copper. These metal layers are fabricated by thermal evaporation as described in section 4.4. Using the back and front side etching techniques in chapter 4, the wafer is thinned down to 30μm using KOH, with the springs released by XeF_2 under-etching (Figure 4 - 8 and Figure 5 - 3).

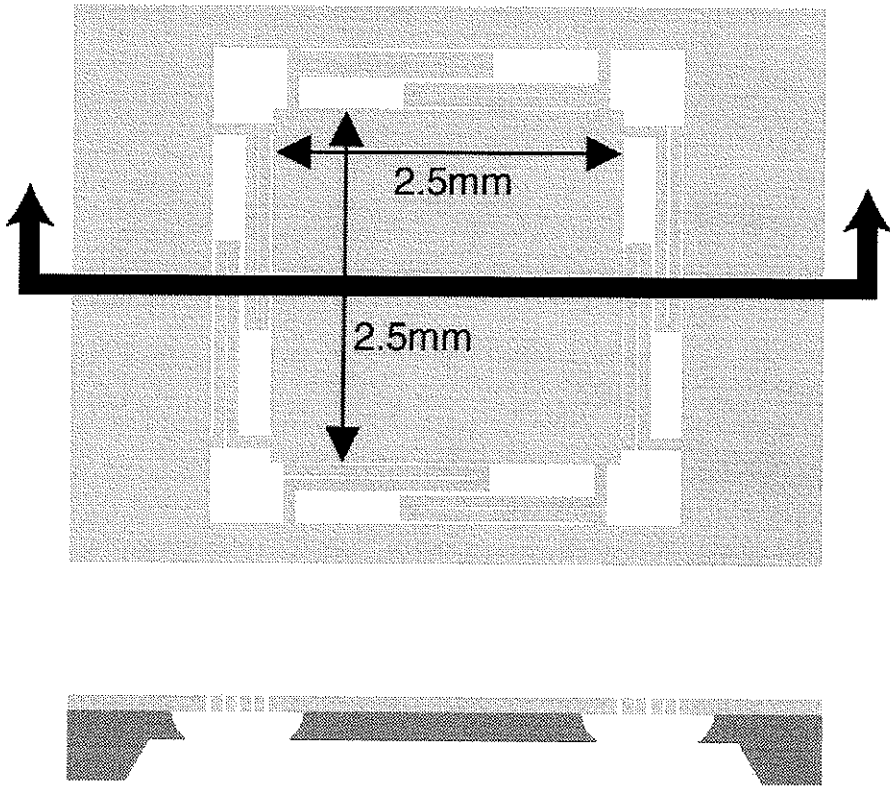

Figure 5 - 3: Transducer cross-section, plan view (top), profile view (bottom).

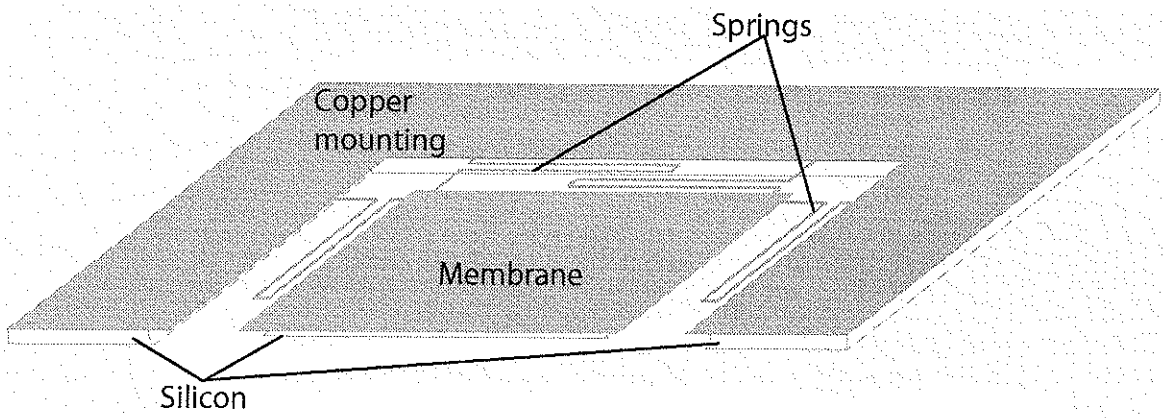

Figure 5 - 4: Transducer cross-section, 3D view (zero stress).

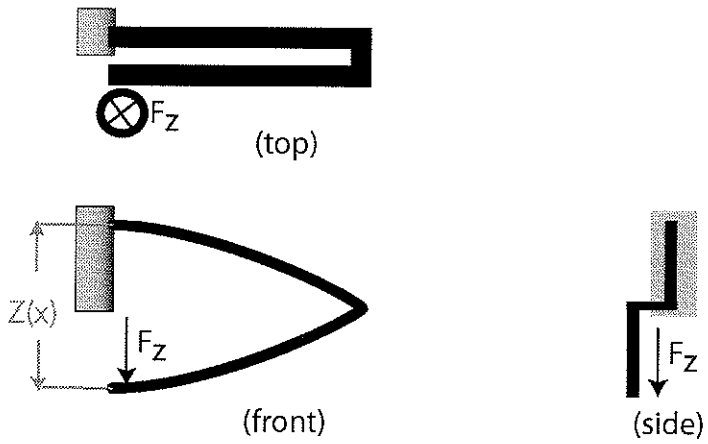

Figure 5 - 5: Spring deflection without intrinsic stress.

The membrane mass is approximately 500μg as calculated in equation 5.1 below.

$$m = \left(\left(2330\frac{kg}{m^3}\right) * \left(30\times10^{-6}m\right) + \left(8890\frac{kg}{m^3}\right) * \left(1\times10^{-6}m\right)\right) * 62.5\times10^{-6}m^2 \qquad (5.1)$$

$$m = 4.9\times10^{-7}\ \text{kg} \qquad (5.2)$$

The membrane is held up by eight springs, two at each corner. The placement of which is done to maximize both spring length and symmetry in the system. The individual springs are shaped to minimize the effects of stress on the membrane's position.

The interleaved spring design was chosen because it maximized spring length, allowed relief of stress within the beams, and set up a symmetrical geometry in which lateral forces on the membrane from the springs should balance out.

Figure 5 - 5 shows that the spring is made up of two equal length beams that deflect in a similar manner. By using the same deflection twice, the endpoint of the beam moves in only one-dimension. This idea applies equally to stressed beams. Canceling out the curvature due to stress by opposing two beams allows the intrinsic stress to be relieved, while the displacement of the membrane remains on the Z-axis (Figure 5 - 6).

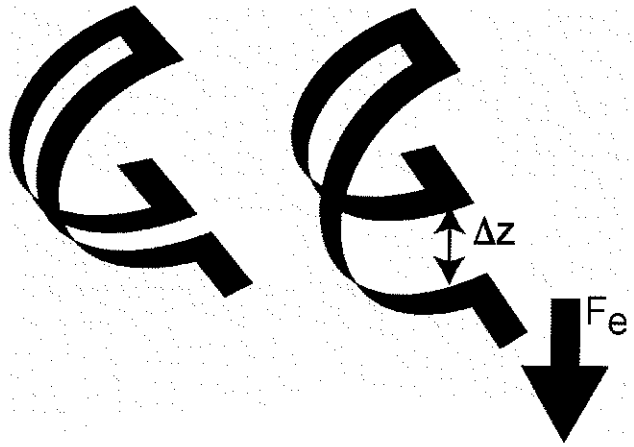

Figure 5 - 6: Spring curvature.

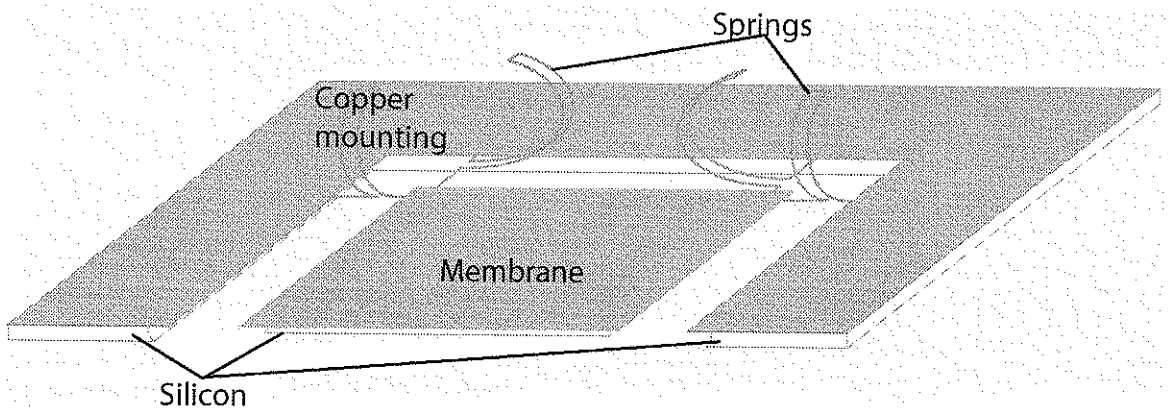

Figure 5 - 7: Transducer cross-section, 3D view (with stress).

In the final fabrication, three transducer beam lengths of 2.1mm, 1.391mm, and 0.698mm were tested (Figure 5 - 8). These beam lengths were chosen to both test designs sensitivity to different beam lengths and to keep the spring constant ratios relatively simple (1, $(2/3)^3$,$(1/3)^3$). As two sets have been constructed, these lengths correspond to membranes (1 and 4), (2 and 5), and (3 and 6) respectively.

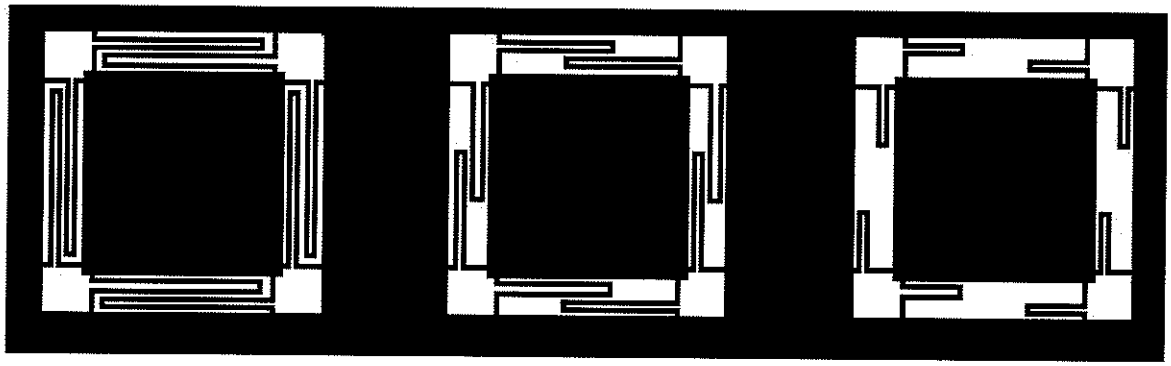

Figure 5 - 8: Mask image of different beam lengths -- 2.1mm (left), 1.4 mm (centre), 0.7 mm (right).

The symmetric placement of springs at each corner also anchors the membrane corners during processing. This is done to minimize wafer twisting due to air gusts catching a corner during and after fabrication. As discussed in section 4.6, significant pressure differentials can occur during the XeF_2 etching and nitrogen purge cycle. These differentials lift up the membranes potentially destroying the micro-springs.

5.2.1 PRELIMINARY DESIGNS

Two prior designs were attempted before the final design. The first used capacitive sensing to measure electric fields. However, once constructed (8 months), testing revealed that intrinsic stress dominated the system, rendering the design useless.

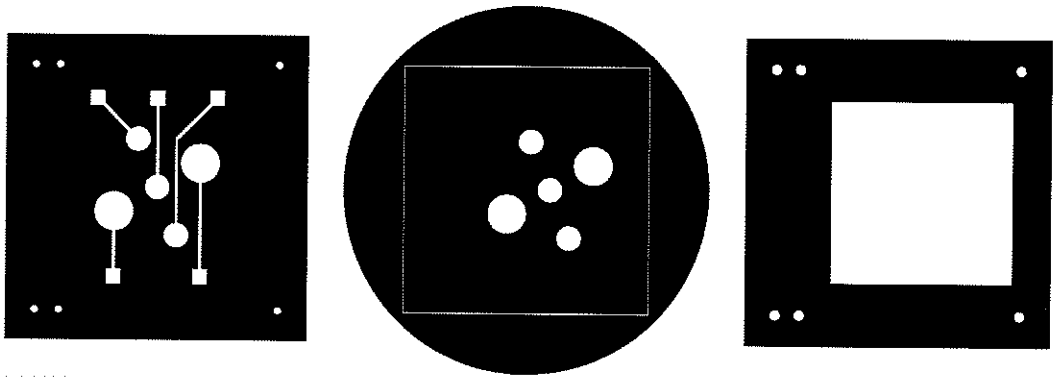

Figure 5 - 9: Masks used in prior iteration #1.

The second design (8 months) served to overcome the stress limitations of the first design by using a membrane suspended over its own XeF_2 etch pit. Although reasonably successful in surviving fabrication the intrinsic stress of the metal again came into play. In this design, the membranes curled up, literally pulling their springs along with them (Figure 5 - 10 and Figure 5 - 11).

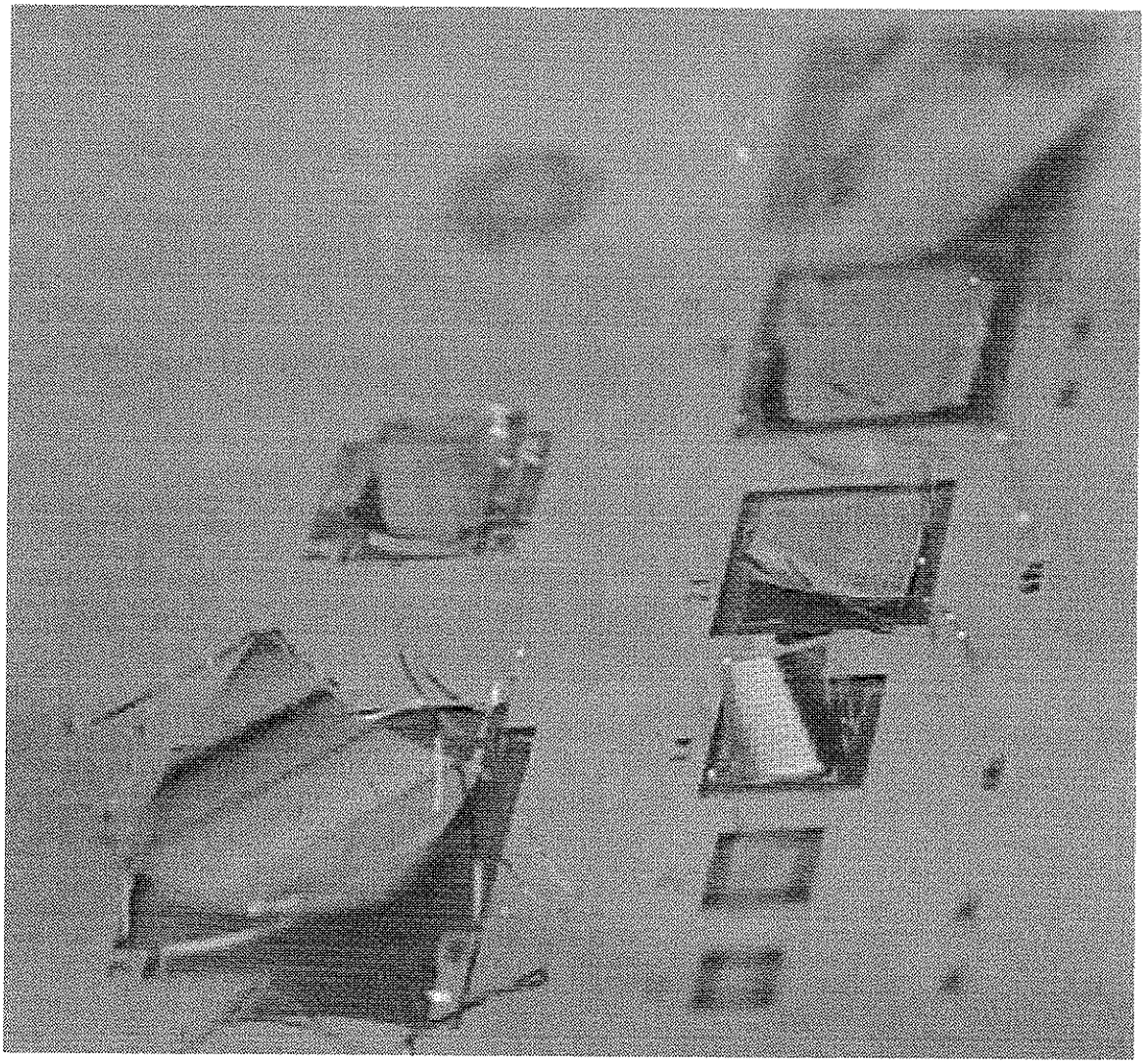

Figure 5 - 10: Effects of intrinsic stress, prior iteration #2.

During the fabrication of design iteration #2, both 5mm * 5mm membranes with 35 and 70μm wide beams were severely damaged. Specifically, during the XeF_2 process pressure spikes during the nitrogen purging cycle picked up the membranes, ripping

springs. For the 35μm beam case, the membrane flipped over onto its topside, ripping all by one or two springs. Compared to this, the 2.5mm x 2.5mm membranes fared significantly better, only being pushed around in the process. Overall, the 70μm beam devices survived fabrication better, making them the choice for the final design iteration (#3).

5.2.2 Material Stress

During the design #2, the effects of stress became clearly evident. The membranes and springs were deformed into a non-usable shape Figure 5 - 10. This section will look at the extrinsic and intrinsic stress associated with using a copper/aluminum structure. Specifically, the extrinsic bimetal stress due to thermal expansion and the intrinsic stress created by temperature variation during the deposition process. Of the two stresses, intrinsic stress within the copper is expected to dominate the system because the aluminum is both softer than copper and 1/100 the thickness.

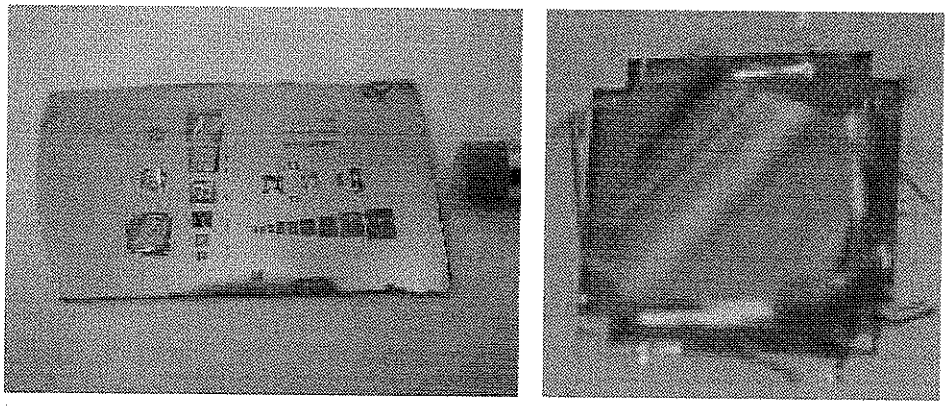

Figure 5 - 11: Membrane curl (intermediate design #2) due to stress.

Bimetal stress occurs because of different expansion coefficients between materials. In the case of thin films, as the device cools after deposition, the different material layers will expand or contract at different rates. This difference in expansion coefficients is observed as a net curvature of the structure (like Figure 5 - 11 above).

An example of this technique can be seen in thermal reed switches or Christmas light blinkers. When a current passes through the switch, it heats up the metal in the switch causing it to bend. Once the temperature becomes large enough, the reed fully deflects, breaking the electrical contact. Upon cooling, the switch closes again repeating the cycle.

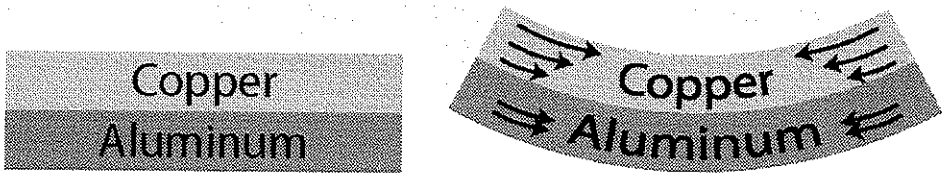

Figure 5 - 12: Bimetal stress.

Change in wafer temperature during evaporation also introduces a stress gradient into the metal. As the metals move from the gas phase back to a solid, they release energy back into the wafer and surrounding chamber. Given that the chamber needs to be water cooled to prevent the steel sidewalls from heating up, it is reasonable to expect the uncooled wafer to rise in temperature.*

This change in temperature causes the structure of the metal to change significantly. The same material still exist throughout, however each atomic layer experiences a slightly different depositon environment and cool down profile. This results in one side having a greater tensile stress then the other and hence a net curvature..

After the material has been released from the wafer, the metal will exhibit either a net tensile or compressive stress. Typically, thermal evaporation result in tensile stress (curvature up off the wafer), however compressive stress (into the wafer) has also been observed.

---

[*] The system energy is likely close to 2MJ, as thermal evaporation requires about 10 minutes, and the breaker is rated for 15A @ 230V.

As an example of how changing the propeties of the metal during deposition can be used. Here is an excerpt from the Xerox PARC website descibing their new stressed metal contacts for high denisity chip packaging.[19]

> "[Using a magnetron sputter system]... scientists change the deposition parameters for each layer of atoms. They create two to five layers of stress-engineered metal by depositing the atoms with varying amounts of energy. They use a high level of energy for the bottom layer, causing the atoms to be packed very tightly. In successive layers, they use progressively less energy, until, at the top layer, the atoms land with very little force, analogous to that of gently falling snow.
>
> This technique harnesses both tensile and compressive stress of metal. Pairs of metal atoms act as springs, causing them to push apart (compressive stress) or pull closer (tensile stress) in order to maintain a consistent distance between them.
>
> Tensile stress is caused when the loosely spaced atoms at the top pull more tightly together, as their electron clouds overlap and bond to one another. Compressive stress is caused when the tightly packed atoms on the bottom layer expand and push away from each other. When the metal is freed from the sacrificial layer, the compressive and tensile stresses in each layer bend the metal into the prescribed shapes."[19]

5.3 Design Considerations

Many design aspects from the membrane size to the optical alignment system were guided by requirements from the laser beam. The 2.5mm by 2.5mm membrane was chosen as it could easily accommodate the 1mm diameter beam. While the laser beam size was a significant factor, printing resolution and the optoelectronic circuit also came into play. Each of these subjects is covered in more detail below.

5.3.1 Printing Resolution

Although micromachining can be done with sub-micron resolution in IC foundries, our in house techniques sacrifice resolution for cost and convenience. Using

locally printed masks* we obtain masks with 7μm resolution and 28μm feature sizes. Each dot on the linotronic printer is 7μm in size; and to obtain a continuous line a minimum of 4 ink dots are required. With large features, excess ink can bleed between adjacent regions. As such a minimum 28μm void is also used around features to prevent the merging of adjacent features.

This design uses 35μm (five ink dots) as a base unit for this mask. This size allows for easy drawing, good reproduction and easy alignment of the lithography mask.

5.3.2 ALIGNMENT

An interesting limitation in micromachining is the alignment between lithographic steps. Quite simply each stage will have some error; the design's ability to tolerate that error will directly and significantly affect the time required for mask alignment. In this design, a back to front side tolerance of 0.1mm required about 5 to 10 minutes of alignment per wafer side.

Figure 5 - 13 however demonstrates how this alignment issue is sidestepped in this design. By using a self aligned front side XeF_2 etch, the springs can still be released despite nearly 0.5mm of misalignment. However, the membrane itself does need to lie on a KOH thinned portion. A note of caution however is that if misaligned, the springs may not drop and flex as expected because of interference from remaining silicon features.

---

* GB Graphics, Winnipeg, Manitoba

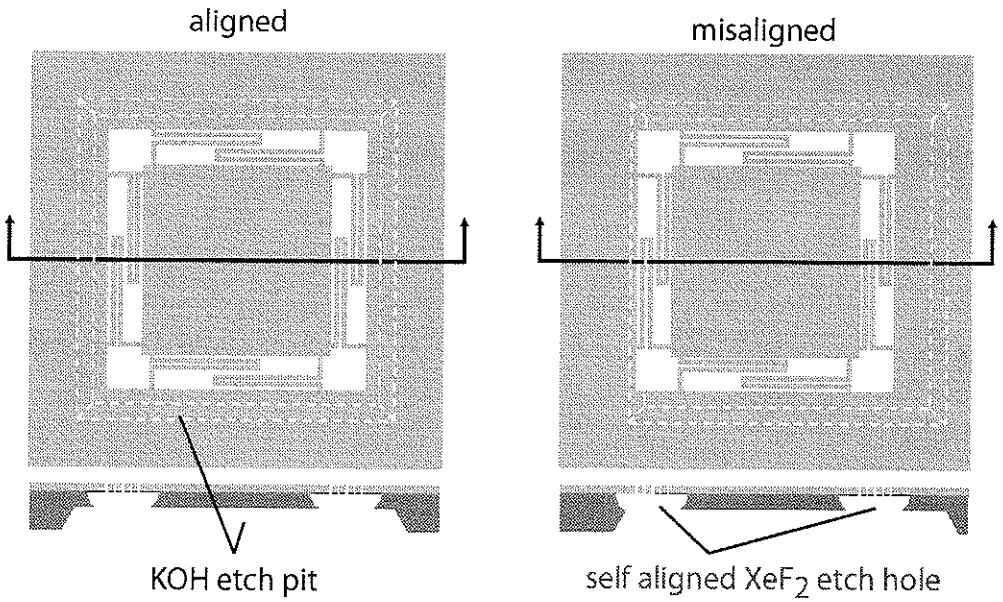

Figure 5 - 13: Transducer lying within an aligned (left) and misaligned (right) KOH etch pit.

5.4 OPTOELECTRONICS

In order to use the transducer for electric field measurments, a method to measure the deflection of the membrane is needed. Three techniques considered were a beam bounce system (selected), an interferometer, and differential capacitance. Of these three, the beam bounce system was chosen because of its current use in high resolution deflection measurements in the University of Manitoba SPM research facility.

Optically, this system consists of a laser, fixed mirror, movable mirror (the transducer), and a photo-detector conductor (Figure 5 - 14 and Figure 6 - 4). To be safe to use without goggles, a class II laser was chosen [20]. With this class of laser, the visible laser light will trigger a blink reflex before eye damage occurs.

During testing, the transducer was excited by an overhead conductor (Figure 5 - 14). The electrostatic attraction (section 3.1.1) between the two devices caused the transducer to deflect upwards towards the applied voltage. Micron sized deflections of the overhead conductor are also reasonable, however this deflection was not measured as its spring constant should be orders of magnitude larger then the 70μm x 1μm beams

used to support the membrane. As verified in section 6.2.4 less than 40μm of membrane deflection is expected from a 17kV/m field (120V@7mm). Given these ratios, the E-field should vary by less then 1% due to membrane deflection during testing.

The vertical deflection of the membrane (Δz) causes the laser beam to shift (Δs) on the detector surface (Figure 5 - 15). Using differential current measurements between the matched quadrants of the photodiode, nanometer resolution is possible.

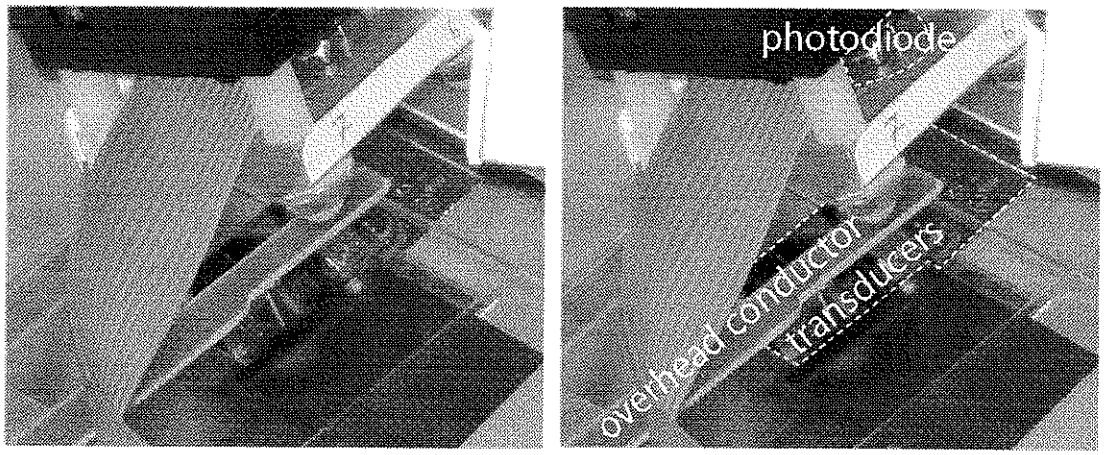

Figure 5 - 14: Test apparatus (close-up).

5.4.1 Optics

This transducer and quad-cell photodiode are aligned onto the reflected laser beam. This is done by aligning each part in sequence on the laser beam:

1. Adjusting the incoming angle of the laser beam on the transducer by alignment of the mirror (Figure 5 - 22).
2. Aligning the membrane position square with the beam path.
3. Zeroing the photodetector using the X-Y alignment stage (difficult).

As discussed in further sections, manual adjustment using an 80 thread per inch screw resulted in an output offset of ±200mV.

The angle at which the laser strikes the detector is calculated using equation 5.3. In this equation, ϕ and θ are the incoming and outgoing laser beam angles respectively. These angles calculated from measurements of the beam position on the mirror, membrane, and photodiode.

$$\theta = \tan^{-1}(20\pm2 / 10\pm2),\ \phi = \tan^{-1}(51\pm2 / 30\pm2),\ \theta = \phi \tag{5.3}$$

$$56.310° < \theta < 70.017°,\ 56.853° < \phi < 62.152° \tag{5.4}$$

As aligned, the laser hits the transducer at approximately 60°. Calculating the ratio of photodiode observed deflection (Δs) to vertical deflection (Δz) in equation 5.5, we obtain a value between 1.1 and 1.2. Thus, the change in spot position is very close to the change in membrane height.

$$\frac{\Delta z}{\Delta s} = \sin\left[\tan^{-1}\left(\frac{51\pm2}{30\pm2}\right)\right] \tag{5.5}$$

$$1.1 < \frac{\Delta s}{\Delta z} < 1.2 \tag{5.6}$$

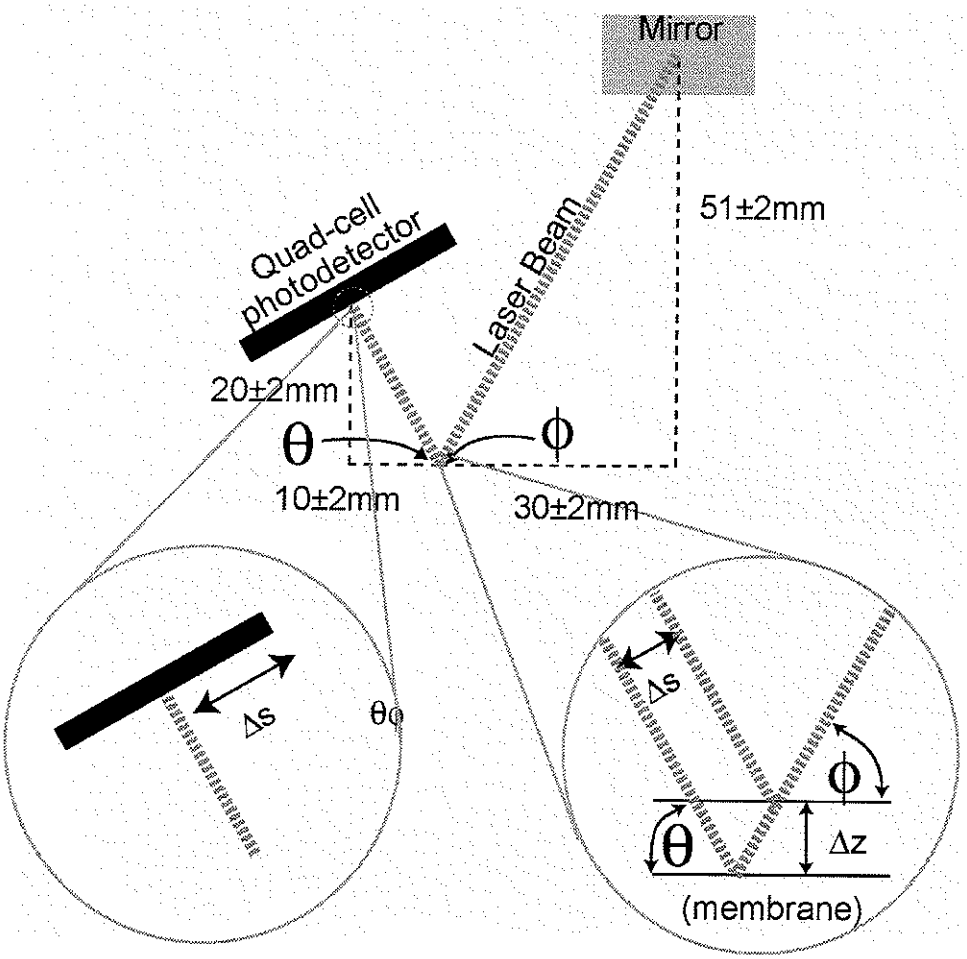

Figure 5 - 15: Beam bounce alignment and optical gain.

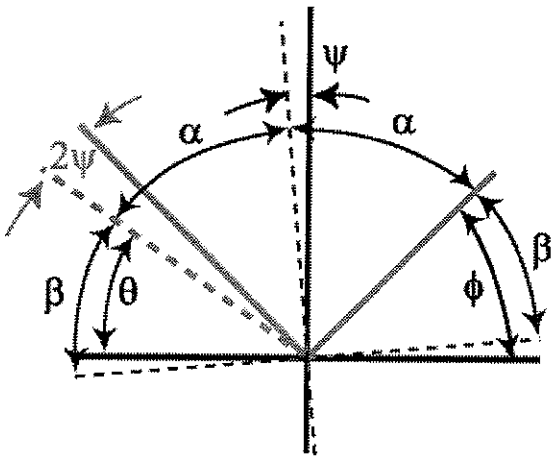

Figure 5 - 16: Effect of angular displacement (ψ) of the membrane.

However, this design is also sensitive to one side of the membrane being less stiff than another. If the membrane surface tilts ψ degrees during actuation (Figure 5 - 16), the laser angle leaving the membrane will change by 2ψ degrees. Given the apparatus dimensions, the beam has to change tilt 0.001° to cause a 1μm change in the photodiode observed deflection (Δs) as calculated from equation 5.7 below.

$$\Delta s = \sqrt{x^2 + z^2}\tan(2\psi) \tag{5.7}$$

$$\psi = \frac{1}{2}\tan^{-1}\left(\frac{1\times10^{-6}}{\sqrt{\left(20\times10^{-3}\right)^2 + \left(10\times10^{-3}\right)^2}}\right) = 1.28\times10^{-3} \text{ degrees} \tag{5.8}$$

Where x and y are 20±2 mm and 10±2 mm respectively as measured on the test jig (Figure 5 - 15). These values are also used for determining the incident angles of the laser beam in equations 5.3 to 5.8.

5.4.2 ELECTRONICS

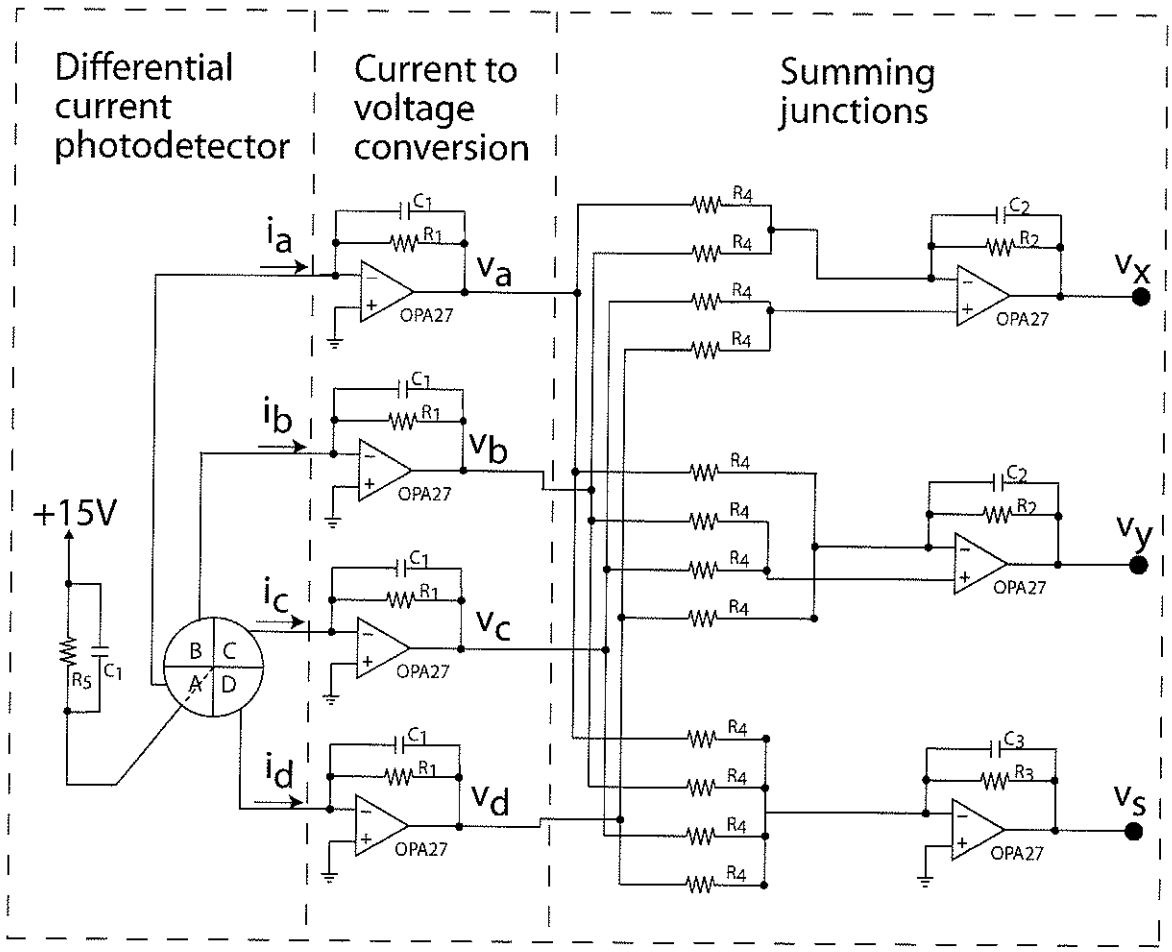

R_1,R_2 =10kΩ
R_3 = 1kΩ
R_4 = 1kΩ
R_5 = 1.5kΩ

C_1, C_2, C_3, C_5=10nF*

Figure 5 - 17: Circuit diagram.

The electronics is drawn heavily from circuit recommendations by UDT [21]. It is comprised of a quad-cell (matched) photodiode, current to voltage converters, and summing/difference junctions (see Figure 5 - 17). The circuit was wire-wrapped to minimize noise while controlling development time and costs (Figure 5 - 18).

* The 10nF capacitors were selected to prevent high frequency oscillations of the op-amps. This inclusion was done at the recommendation of the University of Manitoba, Electrical Engineering support staff.

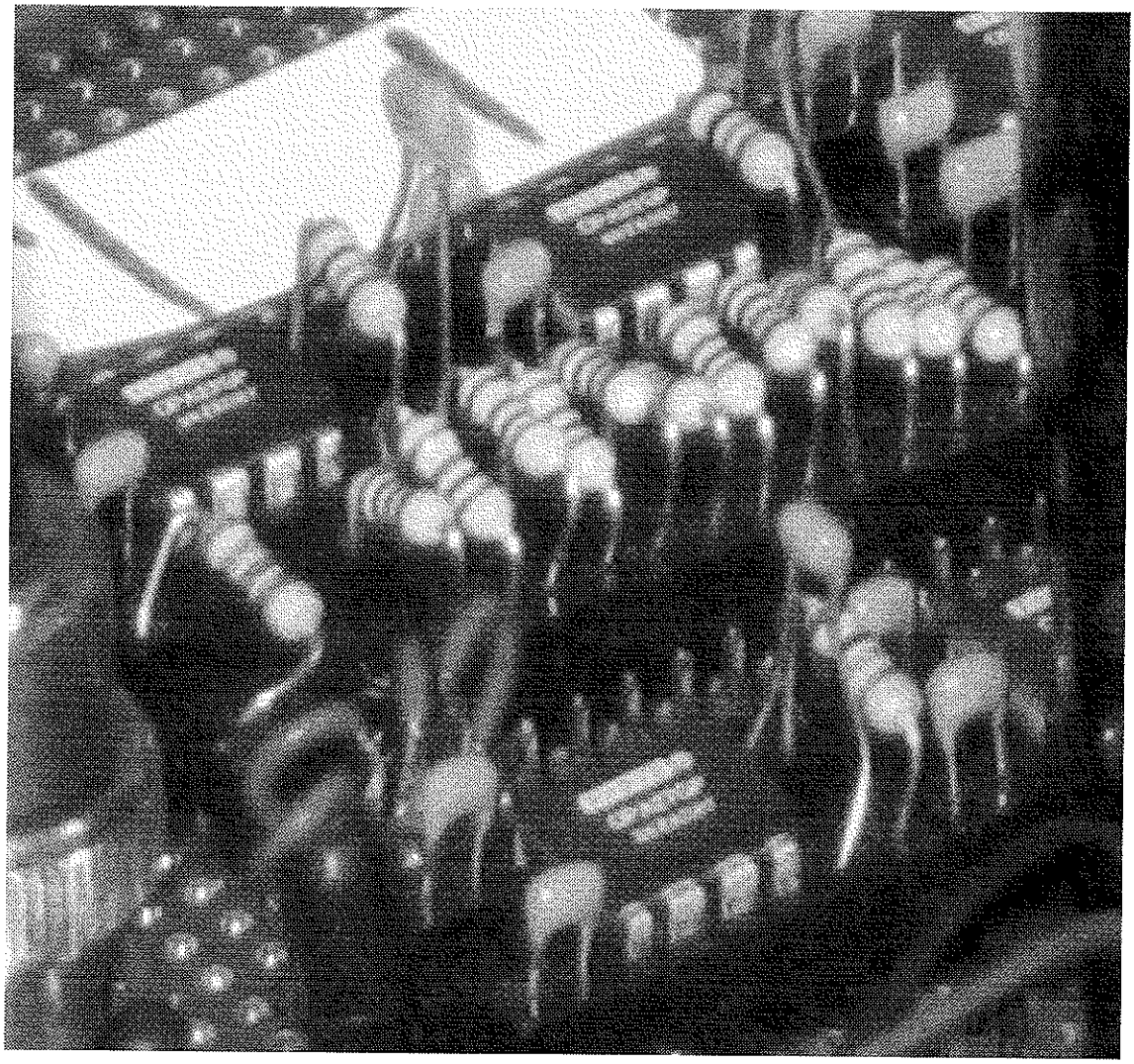

Figure 5 - 18: Electronic amplifier assembly.

5.4.2.1 Differential Current Photodetector

The quad-cell photodiode works by having incoming photons excite electrons from the valence band into the conduction band thus allowing current to flow. The four quadrants are electrically matched during construction, so the differential current out of the device is proportional to the difference in optical power between quadrants. At 632.8nm, the datasheet [22] specified response is 0.32 (A/W) minimum with 0.38 (A/W)

being typical. For the 635nm, 0.87mW laser chosen*, the total output current from all 4 quadrants ($i_a+i_b+i_c+i_d$) would be 330μA. Coupling this current through 10kΩ of resistance gives a maximum output voltage (V_s) of 3.3V. During testing, the actual current sum was measured to be 2.2±0.1V. This implies that 1/3 of the optical power in the laser beam was lost due to scattering off the mirror, transducer, and photodiode packaging. The remaining signal however is more than sufficient to perform high-resolution displacement measurements.

5.4.2.2 Current to Voltage Conversion

In the second stage, current from the photodiode is passed through an op-amp circuit which converts the incoming currents i_a, i_b, i_c, i_d into the voltages v_a, v_b, v_c, v_d respectively. In each of the for op-amp circuits, a 10kΩ (R_1) resistor in parallel with a 10nF capacitor (C_1) forms the feedback path (Figure 5 - 19). Because input noise can severely hinder the overall effectiveness of this device, OPA27 "ultra-low noise precision" op-amps were selected [23].

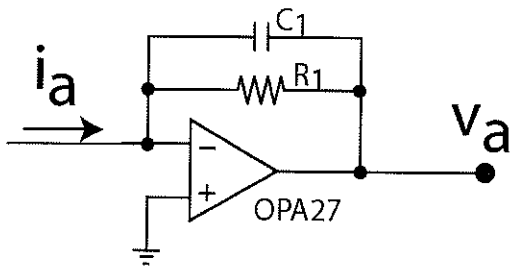

Figure 5 - 19: Current to voltage conversion circuit.

Using RC combination in the feedback of the op-amp, it is important to estimate the cutoff frequency of the circuit. In the equation 5.9 below, ω is the actual frequency of the system, while ω_1 is the cutoff frequency at $1/(R_1C_1)$ in radians/second. From this transformation, we can identify that this stage of the electronics has a break frequency at 1.6kHz.

---

* PTI technologies continuous wave, constant power laser, model number PM01(635-5B)G3.

$$Z_1 = R_1 \| C_1 = \frac{R_1}{1 + R_1 C_1 s} = \frac{R_1}{1 + j\frac{\omega}{\omega_1}} \quad \Omega \tag{5.9}$$

$$\omega_1 = \frac{1}{R_1 C_1} = \frac{1}{10k\Omega \times 0.01\mu F} = 10000 \frac{radians}{s} = 1.6kHz \tag{5.10}$$

Now, relating the output voltage v_a back to the input current i_a in Figure 5 - 9, we have:

$$-v_a = Z_1 \times i_a = \frac{10K\Omega}{1 + j\frac{\omega}{10000}} \times i_a \quad \text{V} \tag{5.11}$$

While v_b,v_c, and v_d have corresponding transformations.

5.4.2.3 Summing Junctions

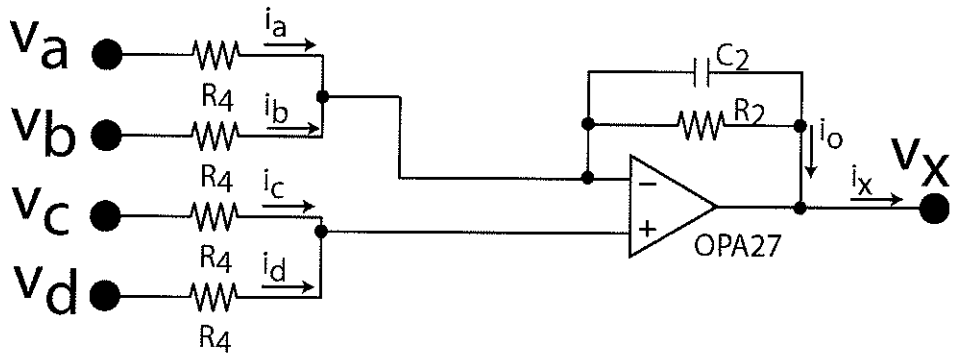

Figure 5 - 20: Summing junction circuit for V_x.

The summing junctions initially had 10nF capacitors across them, but these were later removed during testing without effect on the observed results. However, these calculations will be done assuming the capacitors are in place as drawn in Figure 5 - 17.

Like the current to voltage stage (Figure 5 - 19), the summing junction (Figure 5 - 20) also requires a calculation of its break frequency ω_2. As the R, C values are the same, we get $\omega_1 = \omega_2 = 1.6$kHz.

$$Z_2 = R_2 \| C_2 = \frac{R_2}{1 + R_2 C_2 s} = \frac{R_2}{1 + j\frac{\omega}{\omega_2}} \quad \Omega \tag{5.12}$$

$$\omega_2 = \frac{1}{R_2 C_2} = \frac{1}{10k\Omega \times 0.01\mu F} = 10000 \frac{radians}{s} = 1.6kHz \tag{5.13}$$

Overall, this results in a double pole system at 1.6kHz. Given the measured response in Chapter 6, we find that this break frequency is an order of magnitude away from the resonant response of the system (section 6.2.2).

In analyzing op-amps, Horowitz and Hill [24] outline simple "Golden Rules" for easy analysis of the circuits. They are given in the following quote:

> " Here are the simple rules for working out op-amp behaviour with external feedback. They're good enough for almost everything you'll ever do.
>
> First, the op-amp voltage gain is so high that a fraction of a millivolt between the input terminals will swing the output over its full range, so we ignore that small voltage and state golden rule I:
>
> ***I.*** The output attempts to do whatever is necessary to make the voltage difference between zero.
>
> Second, op-amps draw very little input current (0.2nA for the LF411; picoamps for low-input current types); we round this off, stating golden rule II:
>
> ***II.*** The inputs draw no current.

One important note of explantion: Golden rule I doesn't mean that the op-amp actually changes the voltage at its *inputs*. It can't do that. (How could it and be consistent with golden rule II?) What it does is swing its output terminal around so that the external feedback network brings the input difference to zero (if possible)." [24]

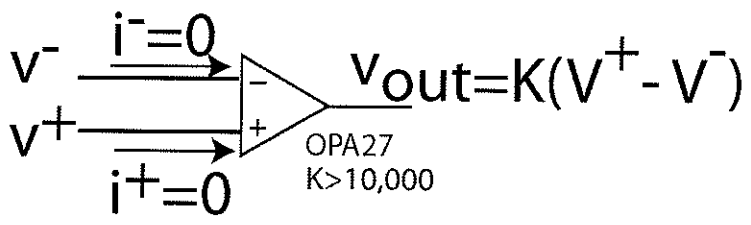

Figure 5 - 21: Basic op-amp assumptions.

Thus, using the golden rules and basic circuit analysis, we can find the summing/difference junction gain.

Solving for the output voltage V_x in Figure 5 - 20, we start with the Kirchoff's laws on the positive input terminal

$$i_c + i_d = i^+ = 0 \quad \text{A} \tag{5.14}$$

therefore

$$v^- = \frac{v_c + v_d}{2} \quad \text{V} \tag{5.15}$$

For the negative input terminal, we have.

$$i_o = i_a + i_b + i^- = i_a + i_b + 0 \quad \text{A} \tag{5.16}$$

$$v^- = v^+ \quad \text{V} \tag{5.17}$$

where

$$i_a = \frac{v_a - v^-}{R_4} = \frac{v_a - \frac{v_c + v_d}{2}}{R_4} \quad \text{A} \tag{5.18}$$

$$i_b = \frac{v_b - v^-}{R_4} = \frac{v_b - \frac{v_c + v_d}{2}}{R_4} \quad \text{A} \tag{5.19}$$

$$i_o = \frac{v^- - v_x}{Z_2} = \frac{\frac{v_c + v_d}{2} - v_x}{Z_2} \quad \text{A} \tag{5.20}$$

Substituting 5.18 through 5.20 into 5.16, we have.

$$\frac{v^- - v^x}{Z_2}_{o} = \frac{v_a - v^-}{R_4} + \frac{v_b - v^-}{R_4} \quad \text{A} \tag{5.21}$$

Substituting v^- with v^+ and solving for v_x step by step gives:

$$v_x = -\left[v^+ + Z_2\left(\frac{v_a - v^+}{R_4} + \frac{v_b - v^+}{R_4}\right)\right] \quad \text{V} \tag{5.22}$$

$$v_x = -\left[v^+ + \frac{Z_2}{R_4}\left(v_a + v_b - 2v^+\right)\right] \quad \text{V} \tag{5.23}$$

$$v_x = -\left[v^+\left(1 - \frac{2Z_2}{R_4}\right) + \left(v_a + v_b\right)\frac{Z_2}{R_4}\right] \quad \text{V} \tag{5.24}$$

$$v_x = -\left[\left(\frac{v_c + v_d}{2}\right)\left(1 - \frac{2Z_2}{R_4}\right) + \left(v_a + v_b\right)\frac{Z_2}{R_4}\right] \quad \text{V} \tag{5.25}$$

$$v_x = -\frac{Z_2}{R_4}\left[\left(v_c + v_d\right)\left(\frac{R_4}{Z_2} - 1\right) + \left(v_a + v_b\right)\right] \quad \text{V} \tag{5.26}$$

and finally

$$v_x = -\frac{Z_2}{R_4}\left[v_a + v_b - (v_c + v_d)(1 + \frac{R_4}{2Z_2})\right] \quad \text{V} \tag{5.27}$$

Similarly, for v_y:

$$v_y = -\frac{Z_2}{R_4}\left[v_b + v_c - (v_a + v_d)(1 + \frac{R_4}{2Z_2})\right] \quad \text{V} \tag{5.28}$$

Solving for v_s we have

$$v_s = -\frac{Z_3}{R_4}\left[v_a + v_b + v_c + v_d\right] \quad \text{V} \tag{5.29}$$

where

$$Z_3 = R_3 \| C_3 = \frac{R_3}{1 + R_3 C_3 s} = \frac{R_3}{1 + j\frac{\omega}{\omega_3}} \quad \Omega \tag{5.30}$$

$$\omega_3 = \frac{1}{R_3 C_3} = \frac{1}{1k\Omega \times 0.01\mu F} = 100000 \frac{radians}{s} = 16kHz \qquad (5.31)$$

Transforming equations 5.27 to 5.30 using break frequencies and the current to voltage relationships in section 5.4.2.2 we have:

$$v_x = \frac{R_2}{R_4\left(1 + j\frac{\omega}{\omega_2}\right)} \frac{R_1}{R_4\left(1 + j\frac{\omega}{\omega_1}\right)} \left[i_a + i_b - (i_c + i_d)\left(1 + \frac{R_4}{2R_2}\left(1 + j\frac{\omega}{\omega_2}\right)\right)\right] \quad V \qquad (5.32)$$

$$v_y = \frac{R_2}{R_4\left(1 + j\frac{\omega}{\omega_2}\right)} \frac{R_1}{R_4\left(1 + j\frac{\omega}{\omega_1}\right)} \left[i_b + i_c - (i_a + i_d)\left(1 + \frac{R_4}{2R_2}\left(1 + j\frac{\omega}{\omega_2}\right)\right)\right] \quad V \qquad (5.33)$$

$$v_s = \frac{R_3}{R_4\left(1 + j\frac{\omega}{\omega_3}\right)} \frac{R_1}{R_4\left(1 + j\frac{\omega}{\omega_1}\right)} \left[i_b + i_c + i_a + i_d \right] \quad V \qquad (5.34)$$

For the selected resistor values of 10kΩ and 1kΩ for R_1 and R_4 respectively, we find that the $R_4/2R_2$ terms in equations 5.31 and 5.32 equal 0.05. Because of this, v^+ is only weighted 5% higher then v^- and could reasonably be neglected for simple approximations. Additionally, if measurements are done at 1/10 of the break frequencies, the $j\frac{\omega}{\omega_{(1-3)}}$ terms can also be ignored. Using both these simplifications we find V=IR representations of...

$$v_x \cong \left(1 \times 10^5\right) \times \left[i_a + i_b - (i_c + i_d) \right] \quad V \qquad (5.35)$$

$$v_y \cong \left(1 \times 10^5\right) \times \left[i_b + i_c - (i_a + i_d) \right] \quad V \qquad (5.36)$$

$$v_s \cong \left(1 \times 10^4\right) \times \left[i_b + i_c + i_a + i_d \right] \quad V \qquad (5.37)$$

5.5 SECONDARY ISSUES

5.5.1 SETUP AND ALIGNMENT

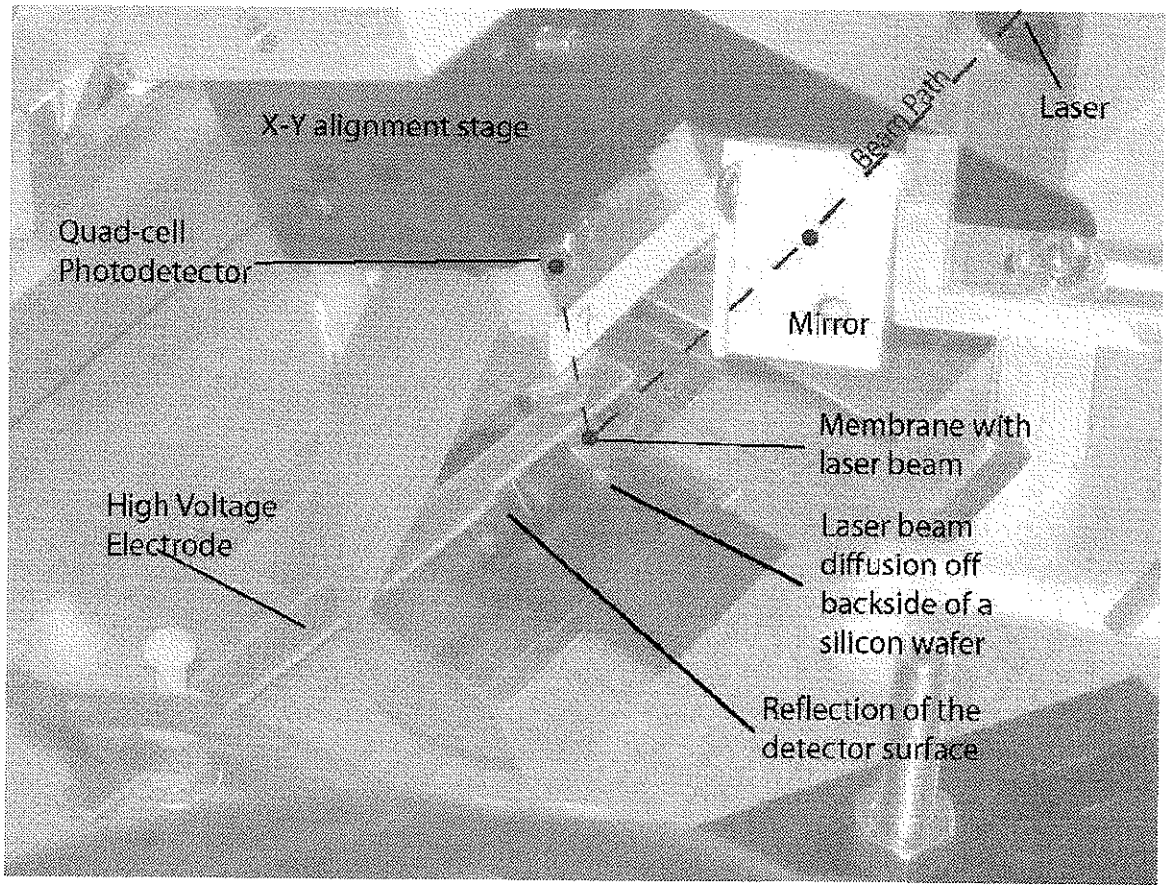

Figure 5 - 22: Measurement setup.

The test setup was fabricated out of 3/4-inch aluminum stock in order to provide sufficient mass and rigidity to hold the photodetector in place during testing. The laser is fixed onto the chassis, while the mirror mount and X-Y alignment stages are held in place using multi-axis mounts.

The initial alignment of the system consisted of setting the mirror position (Figure 5 - 23) and angle in such a manner that it fell on the beam path, reflected down onto the transducer surface at nearly a 90° angle (as seen from the top). The transducers mounting

plate was then shifted back and forth, until the transducer under test was centered on the incoming beam and reasonably square with the remaining structure. As a proof-of-concept design this visual alignment was sufficient for collecting given that the photodiode detects both lateral and vertical displacements from the null position. Once the transducer was in place, the X-Y stage was manually aligned using its support arms to bring the photodiode square with the incoming beam and reasonably centered (Figure 5 - 24). Finally, the laser beam was focused on the transducer surface by adjusting the optical focusing packaged with the laser.

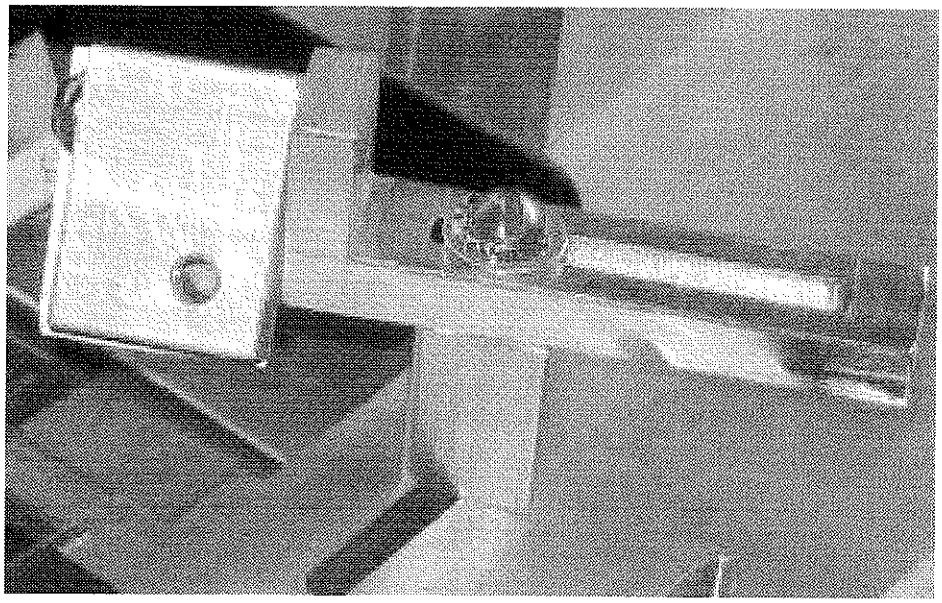

Figure 5 - 23: Mirror mount.

Between test runs, the transducers were slid around (in plane) and re-aligned with the laser beam. Due to changes caused by moving the transducer stage, the photodetector was realigned on the incoming beam using 80 thread per inch alignment screws on the X-Y stage (Figure 5 - 24). As mentioned in section 5.4, nulling was done to 0 ± 200mV.

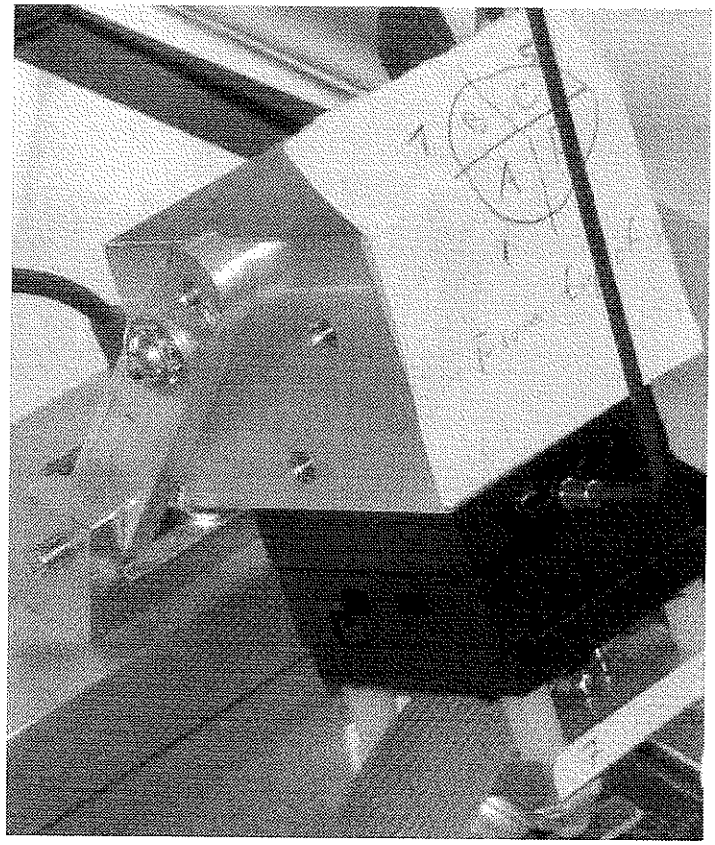

Figure 5 - 24: Photodiode mount.

5.5.2 Environmental Isolation, The aluminum box

During testing, three environmental factors had to be removed. First any external electric fields, second air drafts on the transducer, third vibrations from outside sources.

The first two issues were addressed by enclosing the system inside a large aluminum enclosure. The enclosure was grounded to the same conductor as the test jig and membrane. This enclosure limited the fields under consideration to those caused by the overhead conductor and associated wiring. Fields from the analog electronics were assumed to drop off quickly and thus, not a concern.

This sensor can best be thought of as a spring mass system. As the system vibrates, it introduces oscillations in the membrane as well. When trying to measure the

deflection of the membrane, these vibrations can easily introduce μm sized differences in the transducer's position. This problem was clearly demonstrated by three phenomena. Firstly, when the table was tapped or bumped, the output signals envelope would become larger than the onscreen range of 160 mV. Secondly, a heavy object was dropped on the floor above, caused a visible spike in the output. Thirdly, numerous students moving around the laboratory caused the output voltage to swing over 400mV.

To get around the problem of vibrations caused by nearby people walking around, the experiment was moved onto an isolation table. Once properly isolated, the data presented in the next chapter were collected.

5.5.3 Field Source

In the proposal for this project, testing in accordance with IEEE STD 1308-1994 [24] was given. This standard recommends using a capacitor plate system that is 10x larger then the field meter under test, and suggests using banded conductors to ensure field uniformity. The ultimate objective of this system is to provide a known field, with minimal field deviations. Unfortunately, alignment of the optical system, and the path of the laser beam within the test jig made the use of a large parallel plate capacitor system extremely unwieldy. As such, a 4-5mm wide overhead conductor was placed 7 to 9 mm above the membrane under test (DC and AC cases respectively). While the membranes were grounded along with the surrounding chassis and enclosure (see Figure 5 - 22).

Calculations of the electric field are performed neglecting fringing effects. In reality, the aspect ratio between conductor width and its distance above the ground plane would introduce fringing effects that would lower the electric field strength and potentially improve the resolution of this sensor. In future work, electromagnetic simulation could be used to determine the exact field during testing.

Chapter 6: MEASUREMENTS AND OBSERVATIONS

In this chapter, optical inspection (section 6.1), measured response (section 6.2) and membrane deflection (section 6.3) will be covered. These three sets of test allowed us to confirm the membranes were fabricated properly, establish their response to an electric field, and approximate the membrane deflection.

6.1 OPTICAL INSPECTION

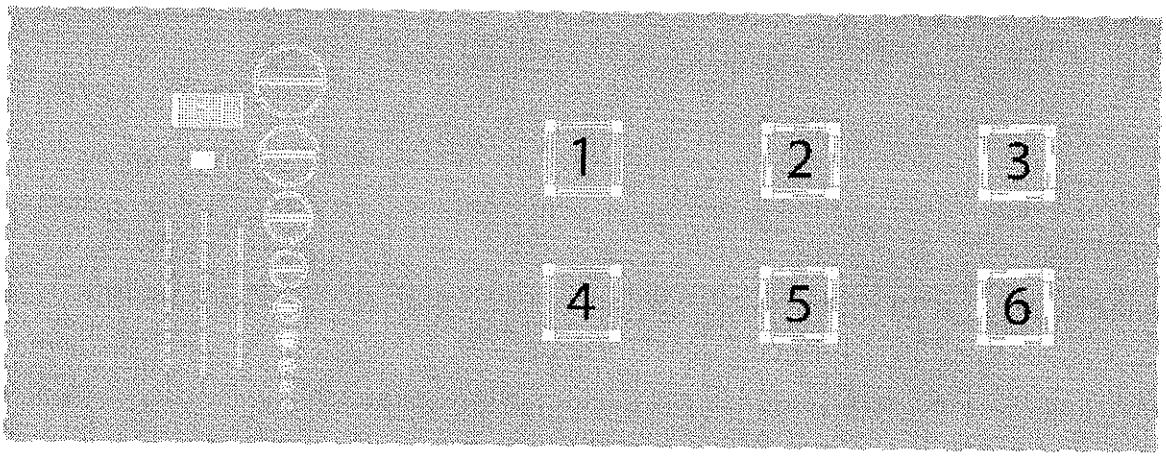

Figure 6 - 1: Wafer layout and transducer numbering.

Optical inspection revealed that as expected, the silicon backing on the membranes allowed them to remain flat while the under-etched springs curled upwards (Figure 6 - 2). Overall, five of the six transducers survived fabrication with minor problems ranging from attached beams to broken springs. Transducers 1 and 4 (top and bottom left) had a top spring fail to release. Transducer 3 (top-right) had a broken spring on the bottom left corner. While the worst damage occurred to Transducer 5 (bottom-centre) where most of its springs were deformed and completely unusable. Additionally, each transducer had beams within the spring remaining attached (Figure 6 - 3).

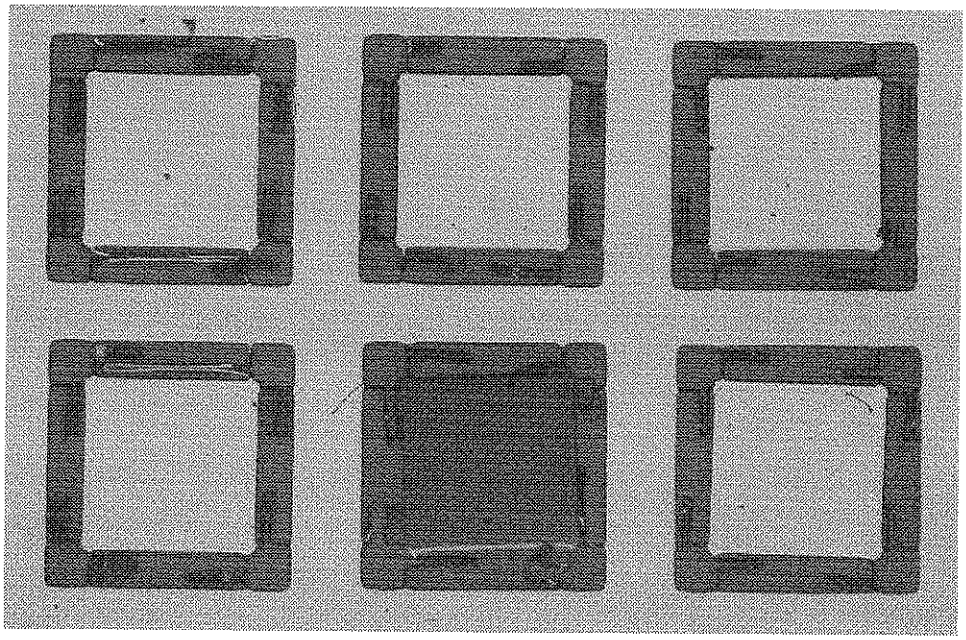

Figure 6 - 2: Composite image of the fabricated membranes – 1,2,3 top, 4,5,6 bottom.

The problem of adjacent spring beams being attached together (Figure 6 - 3) is likely a result of incomplete photoresist developing (section 4.2.4) or etching of the copper (section 4.5). By failing to remove either all the exposed photoresist or copper (section 4.5), the inter beam spacing could easily be compromised. In either case awareness of the problem and more diligent checking at each step could eliminate this problem.

For photoresist developing, poor mass transport and insufficient mixing of the developer solution will cause the problems observed in Figure 6 - 3. If the chemicals are not well mixed, the developer solution becomes locally depleted of active chemicals, creating a dead zone in the mixture. To prevent this, the developer is typically stirred by tipping the developer solution back and forth over the silicon wafer in a glass baking pan.

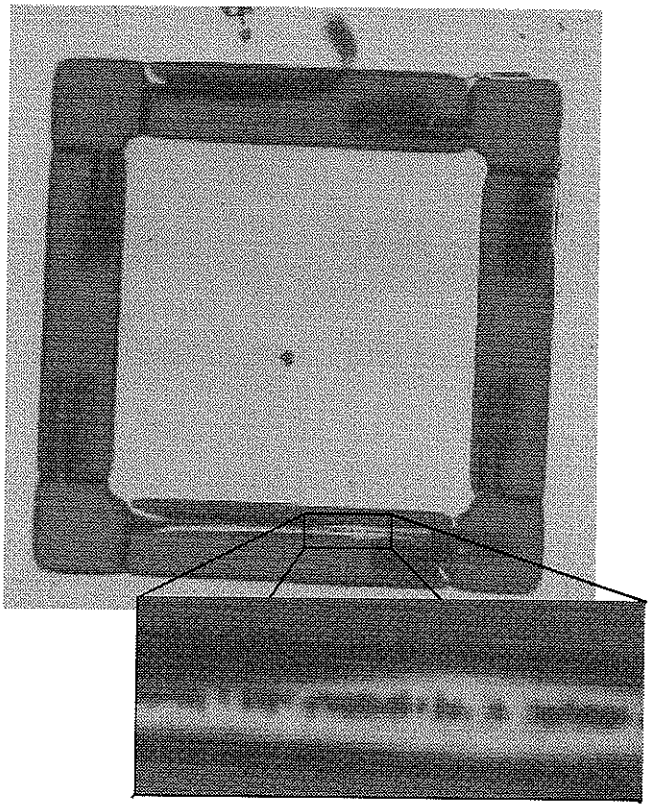

Figure 6 - 3: Attached spring sections in membrane 1.

6.2 FIELD MEASUREMENTS

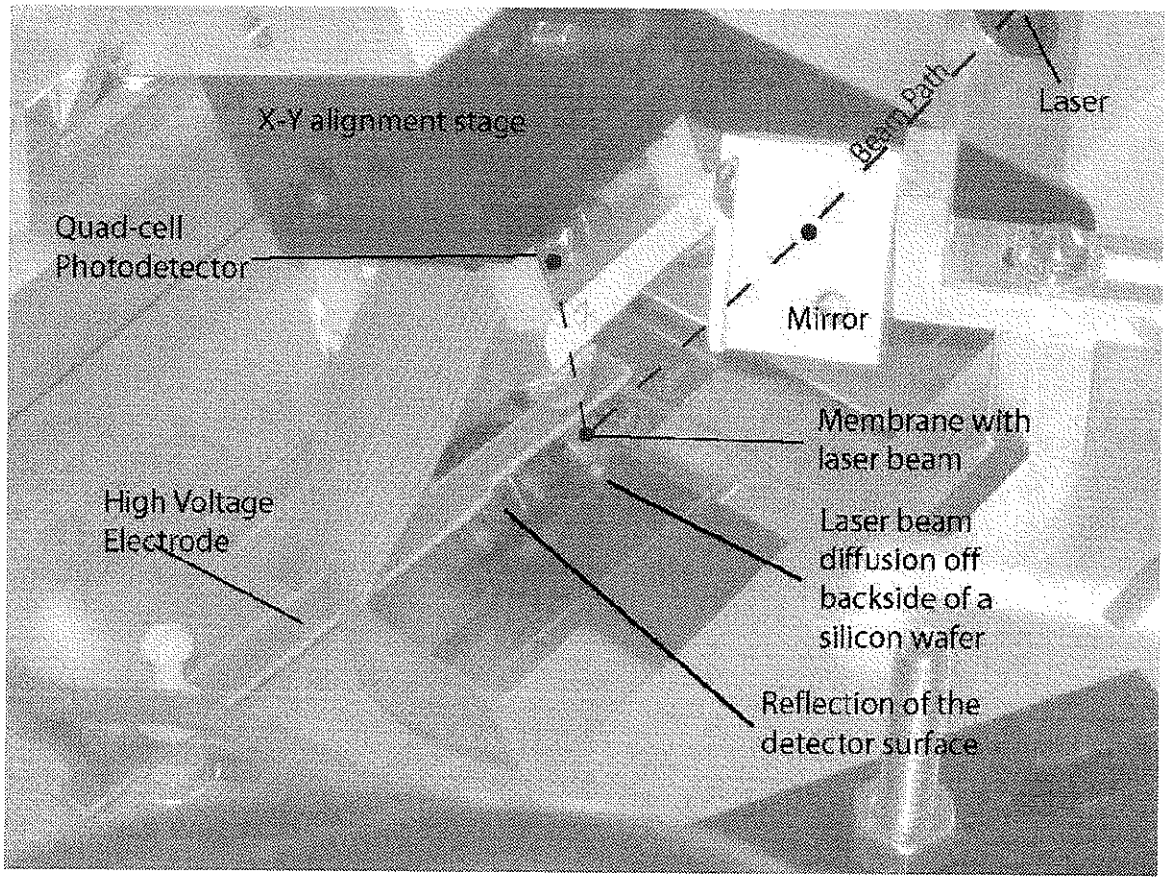

Figure 6 - 4: Test assembly.

To prove the concept of measuring electric field via deflection of a micromachined membrane, several known fields (neglecting fringing) were applied to generate F_e in equation 6.1 (copied from equation 3.16). The DC (V_{DC}^2) and biased AC ($2V_{DC}V_{AC}$) response of each membrane was measured using an oscilloscope. While a lock-in-amplifier was used to measure the biased and unbiased (V_{AC}^2) AC performance. Results for membrane 4 are presented here both for continuity and comparison, selected results from the other membranes are available in the appendices.

$$F_z = \frac{1}{2}\varepsilon AE^2 = \frac{1}{2}\varepsilon A\left(\frac{V_{DC}^2 + 2V_{DC}V_{AC} + V_{AC}^2}{d^2}\right) \quad \text{N} \qquad \text{(6.1) and (3.16)}$$

Using a digital oscilloscope, the values of V_x and V_y were recorded with 8 bit resolution. Through arbitrary selection, membrane 4 was further tested using a lock-in-amplifier*. In this test, both the biased($2V_{DC}V_{AC}$) and unbiased (V_{AC}^2) terms of equation 6.1 were measured. The purpose of this testing was to demonstrate the substantial resolution improvement possible with advanced filtering techniques.

It should be noted that the actual measurements were of the change in spot position on the photodetector Δs. Combining equations 3.16 and 5.4 we obtain the change in spot position with respect to the applied voltage(s):

$$\Delta s \approx 1.15 \frac{\frac{1}{2}\varepsilon A\left(\frac{V_{DC}^2 + 2V_{DC}V_{AC} + V_{AC}^2}{d^2}\right)}{-\left(\frac{N_{parallel}}{N_{series}}\right)\left(\frac{1}{4}\frac{E_{Young's}wt^3}{L^3}\right)} \quad \text{m} \tag{6.2}$$

6.2.1 DC TESTING

For DC testing the AC component of equation 5.3 is zero, which leaves us with:

$$F_{DC} = \frac{1}{2}\varepsilon A\left(\frac{V_{DC}^2}{d^2}\right) \quad \text{N} \tag{6.3}$$

In which:

F_{DC} = is the force on the membrane N
ε = $1*8.854\text{x}10^{-12}$ F/m
A = the area of the membrane m^2
V_{DC} = applied voltage V
d = distance between overhead conducter and the ground plane m

* Stanford Research Systems SR510 lock-in-amplifier. This amplifier behaves like a 12^{th} order filter, literally singling out a single frequency through multiplication and signal processing of the reference frequency. The output of which is the signal's RMS amplitude and noise.

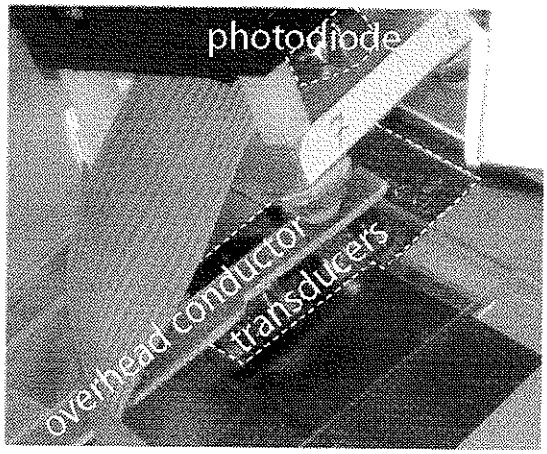

Figure 6 - 5: Overhead conductor to transducer geometry.

For the DC measurements, a 120V pulse was applied to the bottom of the overhead conductor (Figure 6 - 5). This pulse was generated by turning a DC power supply on and off within a 1 second period. During DC testing, this conductor was located 7±1mm above the membrane, producing a 17kV/m field (±15%). During testing, the excitation (input) voltage V_{ext}, and output responses (V_x and V_y) were recorded using a pair of 8-bit digital oscilloscopes (Figure 6 - 7). In Figure 6 - 6 below, the input voltage to response V_y is shown.

Dividing the input pulse into five stages consisting of *off / ramp up / pulse / ramp down / off*, the consistent performance of all the working membranes is visible. Additionally, a slower ramp up time on several membranes makes the E^2 response of the transducer easier to observe. The graphs of the other DC pulse tests can be found at the beginning of appendix 2.

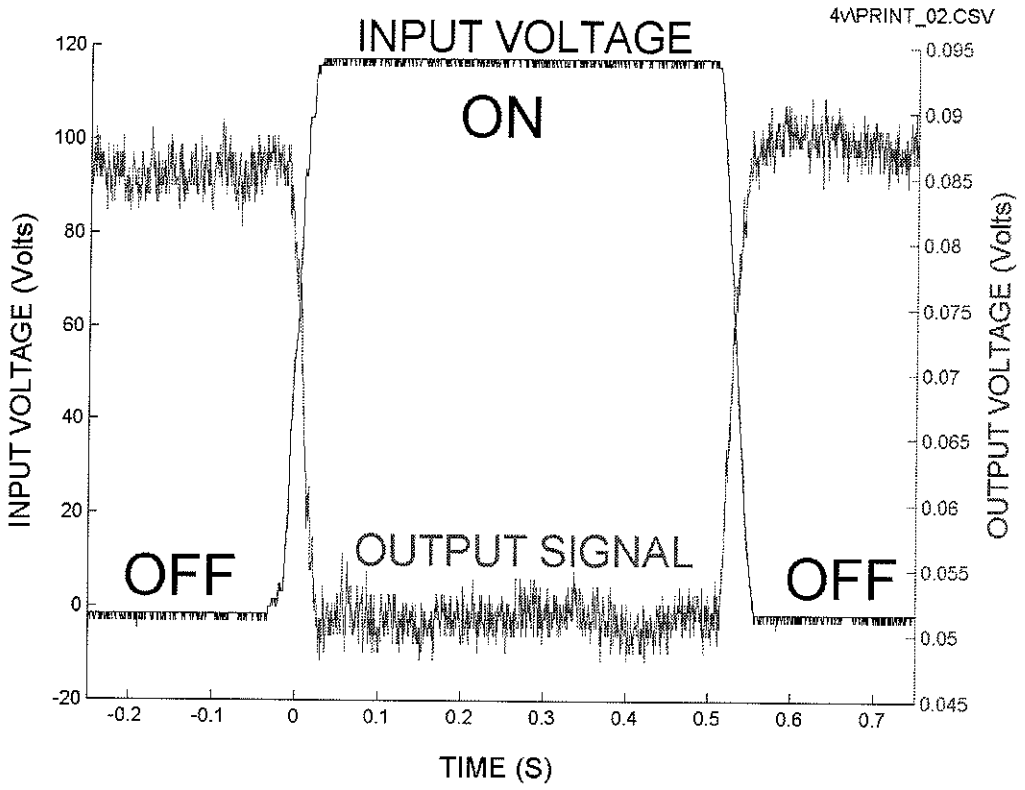

Figure 6 - 6: DC pulse response (membrane 4, run 2).

In Figure 6 - 6 above, the signal moves ≈37mV in response to the 120V signal on the overhead conductor. For the off and on states, the output is 87±3.75mV and 50±2.5mV. The noise envelope is taken as 7.5mV, as it includes the full deviation of off state during the test. Using only the V_y data we can determine the ratio of change in output signal to applied field, determining the sensitivity of the system. For the V_{DC}^2 case, deflection is proportional to E_{DC}^2. Thus, to calculate the effective field enclosed within the noise, we take the square root of the ratio between noise envelope and signal response as shown in equation 6.5 below.

$$\frac{\text{Noise Envelope}}{E_n^2} = \frac{\text{Response}}{\text{E}_{\text{DC}}^2} \tag{6.4}$$

$$E_n = \sqrt{\frac{\text{Noise Envelope}}{\text{Response}} \frac{|\text{Applied Voltage}|}{\text{distance}}} \quad \text{V/m} \tag{6.5}$$

Solving equation 6.5 we have

$$E_n = \sqrt{\frac{7.5mV}{37mV}}\left(\frac{120V}{7mm}\right) = 7.7kV/m \tag{6.6}$$

Thus 7.7kV/m represents an easily discernable DC resolution for this device.

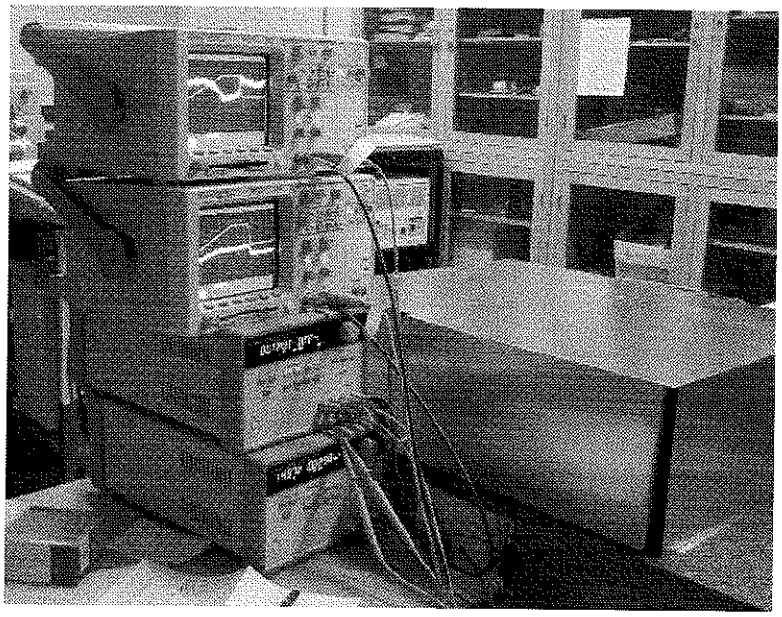

Figure 6 - 7: Supporting test equipment.

In Figure 6 - 8 below another run of membrane 4 shows how both the outputs V_x and V_y change with applied pulse. As a quad-cell photodiode was used, the movement along both axis could be attributed to either the membrane changing angle, or the optical system not being perfectly square. Optimizing the alignment and the magnitude/phase response is left for future work.

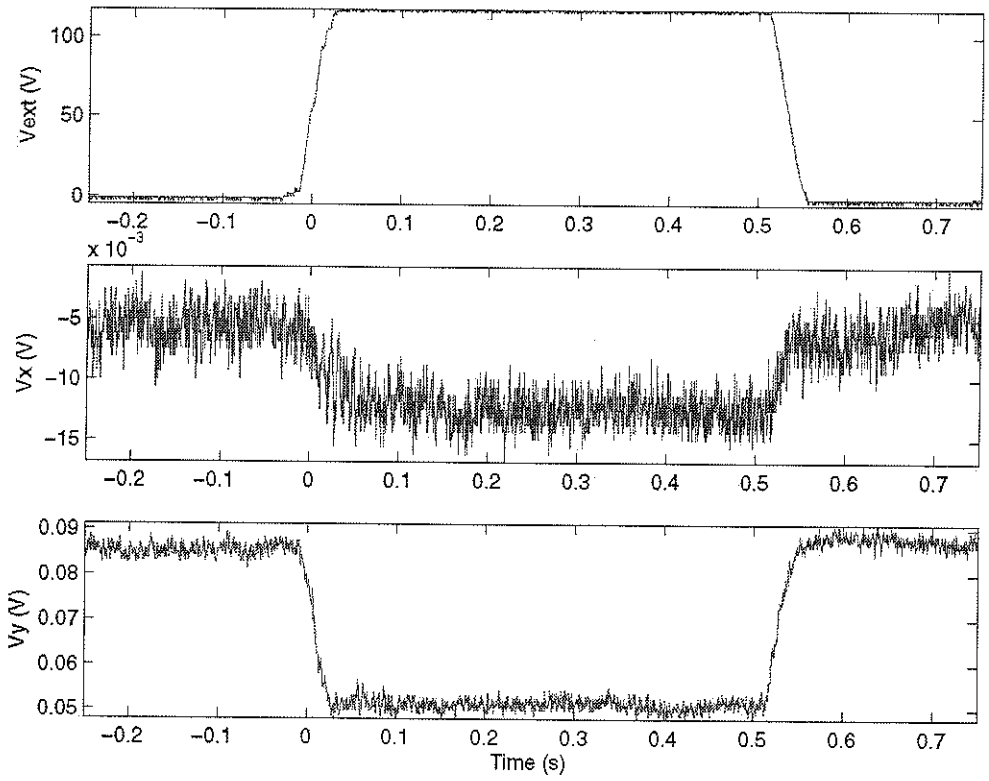

Figure 6 - 8: DC pulse testing, membrane 4, run 2.

As outlined in section 5.5, the apparatus was zeroed using the X-Y stage to within ±200mV. For comparison, if the entire beam fell on one quadrant of the photodetector it would cause a 22V response in both V_x and V_y based on the 2.2±0.1V output observed in V_s.

6.2.2 AC TESTING

In the DC pulse case, we observed the force due to the V_{DC}^2 term of equation 6.1. For the biased AC testing (DC+AC), we examine the response due to the ($2V_{DC}V_{AC}$) term as seen in equation 6.7 below.

$$F_{ACDC} = \frac{1}{2}\varepsilon A\left(\frac{2V_{DC}V_{AC}}{d^2}\right) \quad \text{N} \tag{6.7}$$

Since the DC bias is constant for these tests, the signal and noise measured are in direct response to the AC signal. By selecting a natural frequency * of the system the maximum signal envelope is observed. Hence the best signal to noise envelope ratio can be obtained.

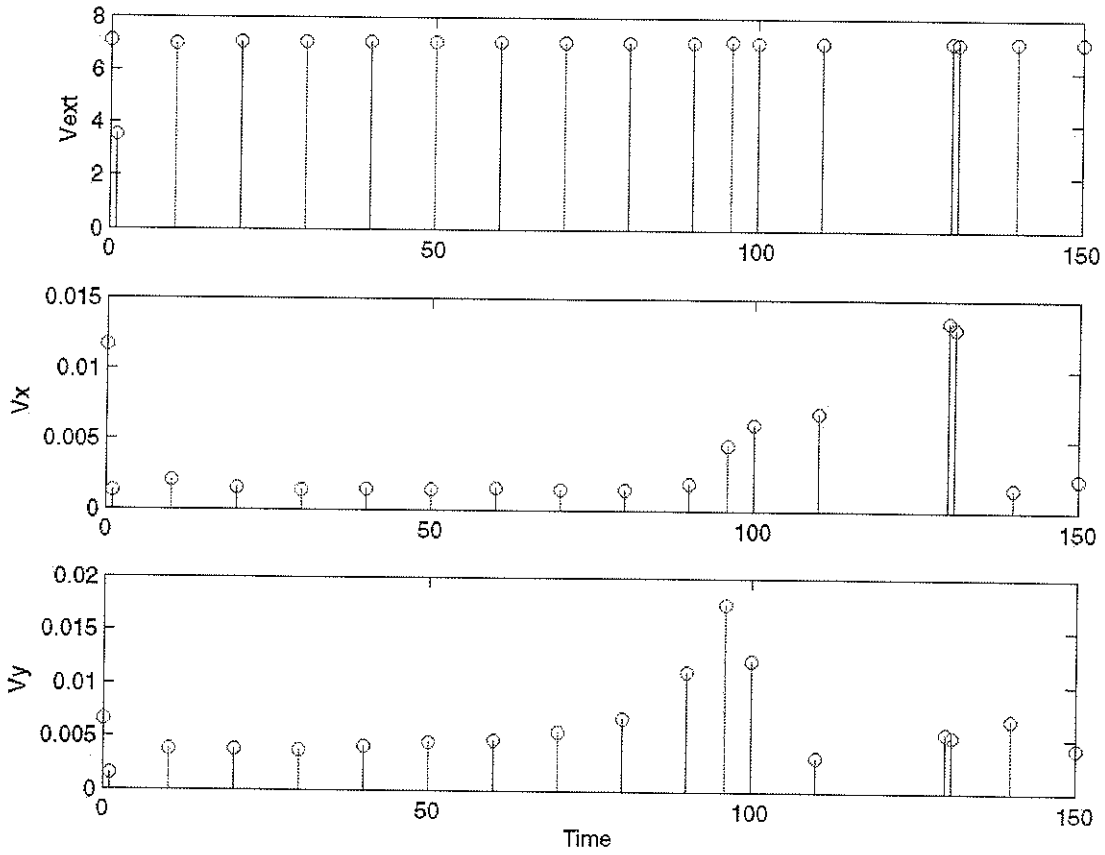

Figure 6 - 9: RMS response vs. frequency of membrane 4.

To determine the natural frequency of the system, the excitation voltage $10\sin(\omega t)$ was swept from 1Hz to 120Hz, with the RMS power shown in Figure 6 - 9 above. The

* Resonant frequency implies a known transfer function with explicit poles and zeros. As many factors and phase shifts occur in this system, the term natural frequency was chosen to correspond with the peak AC response. Additionally, different peaks exist for both vertical and horizontal directions of travel.

response of membrane 4, operating at a vertical natural frequency is shown Figure 6 - 10. For an excitation voltage (V_{ext}) of 5V at 131 Hz below, 1/9 of the V_y response is easily discernable, allowing a 61V/m field to be confidently measured (see equation 6.10).

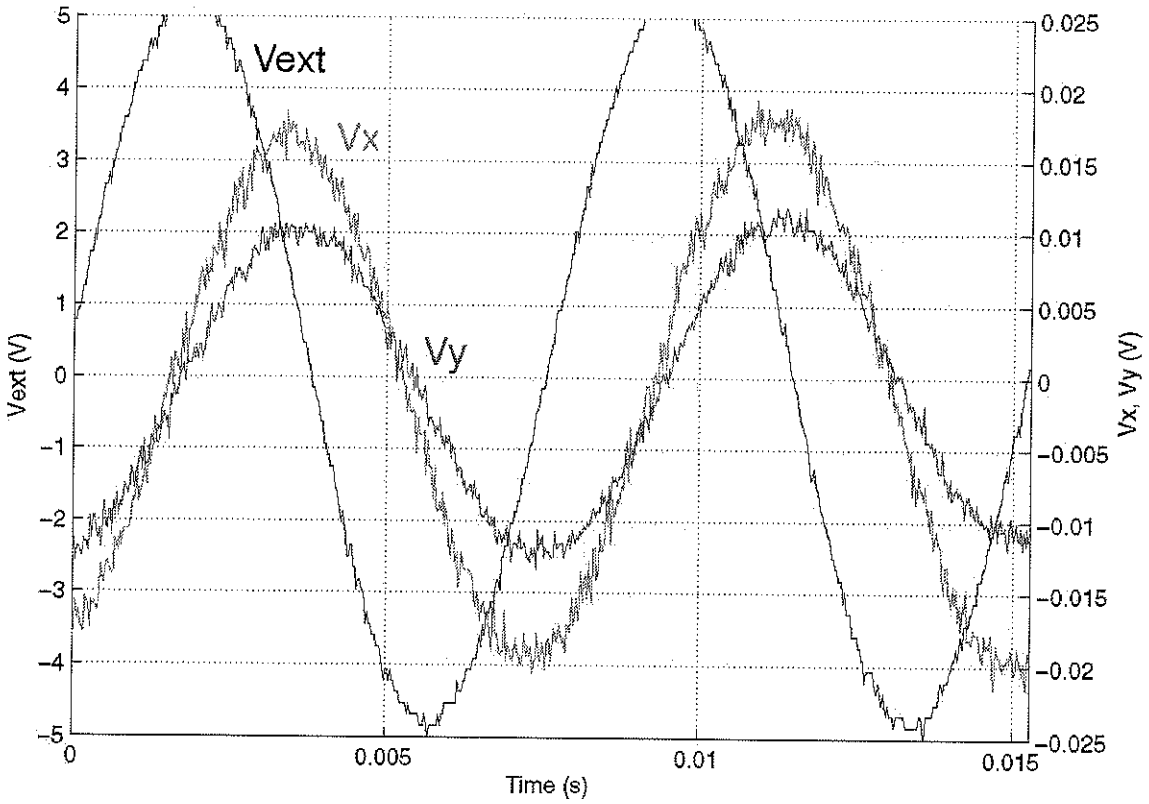

Figure 6 - 10: Membrane 4, 5V, 131Hz AC signal with 120V DC bias.*

Based on the noise envelope (2.5mV) and peak-to-peak response (22.5mV) of Figure 6 - 10 we can calculate the equivalent E field contained within the noise envelope (equation 6.8). Note, that because the DC component is constant, we are considering only the AC effects.

$$\frac{\text{Noise Envelope}}{E_n} = \frac{\text{Signal}}{E_{AC}} \qquad (6.8)$$

* file: f4v1\print15.csv

$$E_n = \frac{\text{Noise Envelope}}{\text{Response}} \frac{V_{AC}}{\text{distance}} \quad \text{V/m} \tag{6.9}$$

Using the V_y curve in Figure 6 - 10 and solving equation 6.9 we have:

$$E_n = \frac{2.5mV}{22.5mV} \frac{5V}{9mm} = 61 \text{ V/m} \tag{6.10}$$

Thus 61V/m represents an easily discernable biased AC resolution for this device.

6.2.3 AC Testing With Lock-In-Amplifier

Membrane 4 was also selected for additional testing using a lock-in-amplifier. These amplifiers use digital signal processing to isolate single frequencies buried within much larger noise. This process involves multiplying the signal with a frequency reference and integrating out the non-integer multiples, allowing the target waveform and its harmonics to be easily obtained.

For these tests, the lock-in-amplifier was used on membrane 4 with a 10-second integration time. The system was driven with 97 and 49 Hz signals for the biased ($2V_{DC}V_{AC}$) and unbiased (V_{AC}^2) cases respectively. This choice came from another natural frequency of the membrane, at 97Hz. While half this frequency (49Hz) was chosen to excite the 97Hz resonance based on equation 6.11.

$$\sin^2\theta = \frac{1-\cos 2\theta}{2} \tag{6.11}$$

From the previously recorded data sets, the peak response occurred between 96Hz and 100Hz. Additionally, each test was allowed about one minute of settling time before the measurement was taken. Measuring the first harmonic response to a 97Hz signal with 120V DC bias we obtain the results in shown in Table 6 - 1 and Figure 6 - 11. Measuring the second harmonic to a 49Hz signal with no bias we obtain Table 6 - 2 and Figure 6 - 12. Where noise equivalent field formulas for each case are given in equations 6.13 and 6.16 respectively.

Table 6 - 1: Measured results, AC+120V bias.

AC signal (mV)	Dist. (mm)	Response (μV)	E-Field (V/m)	Noise equivalent field (V/m)
100mV	9±1	360±10	11.11	.31
50mV	9±1	170±10	5.55	.33
25mV	9±1	70±10	2.77	.40

$$\frac{\text{RMS Noise}}{E_n} = \frac{\text{RMS Signal}}{\text{E}_{AC}} \tag{6.12}$$

$$E_n = \frac{\text{RMS Noise}}{\text{RMS Signal}} \frac{|\text{V}_{AC}|}{\text{distance}} \quad \text{V/m} \tag{6.13}$$

solving 6.13 we have:

$$E_n = \frac{10\times10^{-6}}{360\times10^{-6}} \frac{100\times10^{-3}}{9\times10^{-3}} = 0.308 \quad \text{V/m} \tag{6.14}$$

Thus 0.31V/m represents the biased AC resolution with this device using a lock in amplifier.

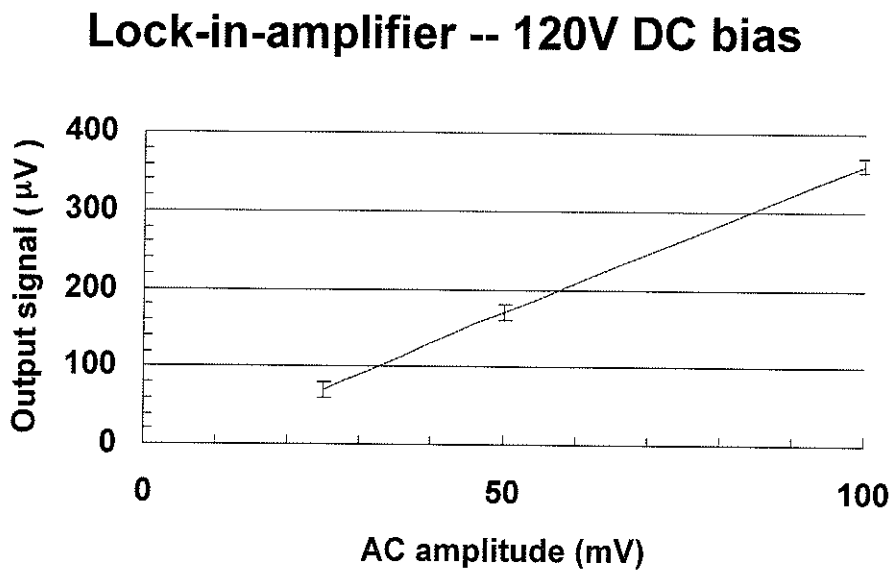

Figure 6 - 11: Lock-in-amplifier results, biased ($2V_{DC}V_{AC}$) case.

Where the results graphed in Figure 6 - 11 confirm the linear relationship between the AC excitation $|V_{AC}|$ and the RMS output as predicted in the $2V_{DC}V_{AC}$ term of equation 3.16.

Table 6 - 2: Measured results, unbiased (V_{AC}^2) case.

AC signal (V)	Dist. (mm)	Response (μV)	E-Field (V/m)	Noise equivalent field (V/m)
10	9±1	410±10	1111	174
5	9±1	120±10	555	160
2.5	9±1	40±10	277	139

$$\frac{\text{RMS Noise}}{E_n^2} = \frac{\text{RMS Signal}}{\text{E}_{\text{AC}}^2} \quad \text{m}^2/\text{V} \tag{6.15}$$

$$E_n = \sqrt{\frac{\text{RMS Noise}}{\text{RMS Signal}}}\frac{|\text{V}_{\text{AC}}|}{\text{distance}} \quad \text{V/m} \tag{6.16}$$

solving equation 6.16 we have:

$$E_n = \sqrt{\frac{10}{40}}\frac{2.5}{9\times10^{-3}} = 138.88 \quad \text{V/m} \tag{6.17}$$

Thus 139V/m represents the resolution of the unbiased AC response using a lock-in-amplifier.

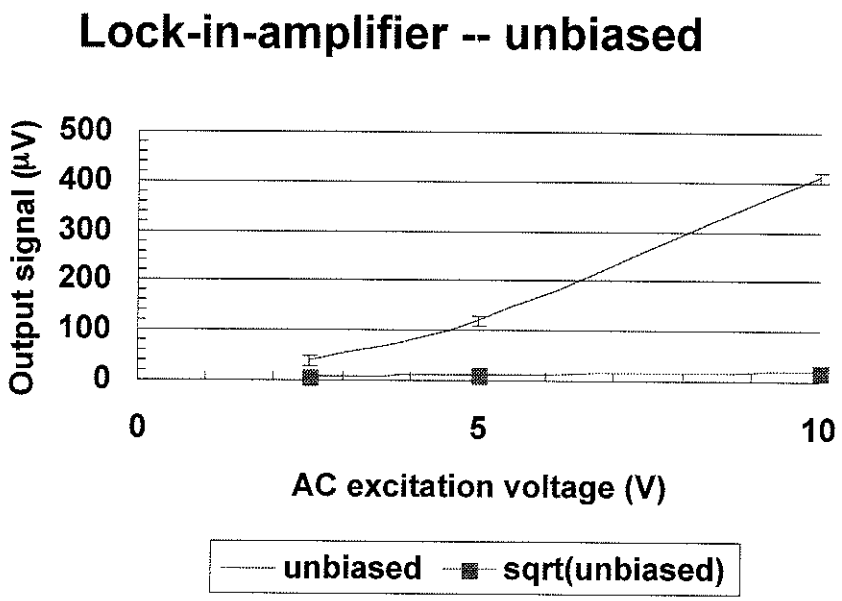

Figure 6 - 12: Lock-in-amplifier results, unbiased (V_{AC}^2) case.

Where the results graphed in Figure 6 - 12, show how the force causing membrane deflection is proportional to the V_{AC}^2. Taking the square root of the measurement, we obtain a straight-line relationship with $|V_{AC}|$.

6.2.4 SUMMARY OF MEMBRANE 4 RESULTS

In equation 6.2 (repeated as 6.18 below), we determined the relationship between applied voltage and spot movement to be:

$$\Delta s \approx 1.15 \frac{\frac{1}{2}\varepsilon A\left(\frac{V_{DC}^2 + 2V_{DC}V_{AC} + V_{AC}^2}{d^2}\right)}{-\left(\frac{N_{parallel}}{N_{series}}\right)\left(\frac{1}{4}\frac{E_{Young's}wt^3}{L^3}\right)} \qquad (6.18) \text{ and } (6.2)$$

Measuring the response to each of the voltage terms, we were able to calculate the equivalent field contained within the noise envelope. The relationships of which were given in sections 6.2.1 and 6.2.2.

Table 6 - 3: Summary of resolutions for membrane 4.

Measurement	Relationship	Field strength represented by noise
DC^2 (oscilloscope)	$\frac{\text{Response}}{\text{Noise Envelope}} = \frac{E_{DC}^2}{E_n^2}$	$E_n = \sqrt{\frac{7.5mV}{37mV}\left(\frac{120V}{7mm}\right)^2} = 7.7$ kV/m
DC*AC (oscilloscope)	$\frac{\text{Response}}{\text{Noise Envelope}} = \frac{E_{AC}}{E_n}$	$E_n = \frac{2.5mV}{22.5mV}\frac{5V}{9mm} = 61$ V/m
DC*AC (lock-in)	$\frac{\text{RMS Response}}{\text{RMS Noise}} = \frac{E_{AC}}{E_n}$	$E_n = \frac{.01mV}{.36mV}\frac{100mV}{9mm} = .31$ V/m
AC^2 (lock-in)	$\frac{\text{RMS Response}}{\text{RMS Noise}} = \frac{E_{AC}^2}{E_n^2}$	$E_n = \sqrt{\frac{.01mV}{.04mV} * \left(\frac{2.5V}{9mm}\right)^2} = 139$ V/m

6.3 SPRING CONSTANT ESTIMATION

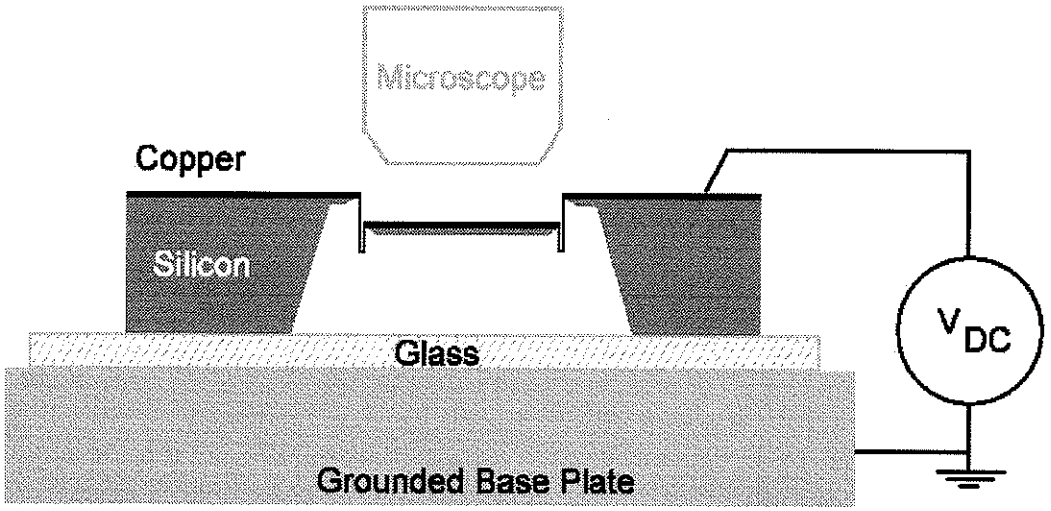

Figure 6 - 13: Deflection vs. voltage test jig.

The simple relationship $F = kz$ (equation 6.20 below) can be used to derive the spring constant of the membrane. By applying a known voltage/field to the membrane and measuring the deflection z, we can calculate k in equation 6.20 in a similar manner to section 3.2. However, because of the presence of insulating glass, an effective dielectric constant (6.19) must be used.

$$\varepsilon_r = \frac{\varepsilon_{air}\varepsilon_{glass}}{\varepsilon_{air} + (\varepsilon_{glass} - \varepsilon_{air})\dfrac{d_{air}}{d_{air} + d_{glass}}} \tag{6.19}$$

$$\Delta z = \frac{\dfrac{1}{2}\varepsilon A\left(\dfrac{V_{DC}^2 + 2V_{DC}V_{AC} + V_{AC}^2}{d^2}\right)}{k} \quad \text{m} \tag{6.20}$$

Where,

F_{DC} = DC electric field force
V_{DC} = applied voltage
$\varepsilon_{air} = 1$
$\varepsilon_{glass} = 6.2$
$\varepsilon_O = 8.854 \times 10^{-12}$ F/m
$A = 6.25$ mm^2
$d_{total} = d_{glass} + d_{air}$
$0 \le d_{air} \le 400$ μm
$d_{glass} = 100$ μm
k = spring constant N/m

Each working membrane was tested in the apparatus illustrated in Figure 6 - 13 at voltages of 0, 40, 80, and 120 volts. The deflection was measured optically using a microscope with 4μm of accuracy, giving us a resolution of ±2μm.

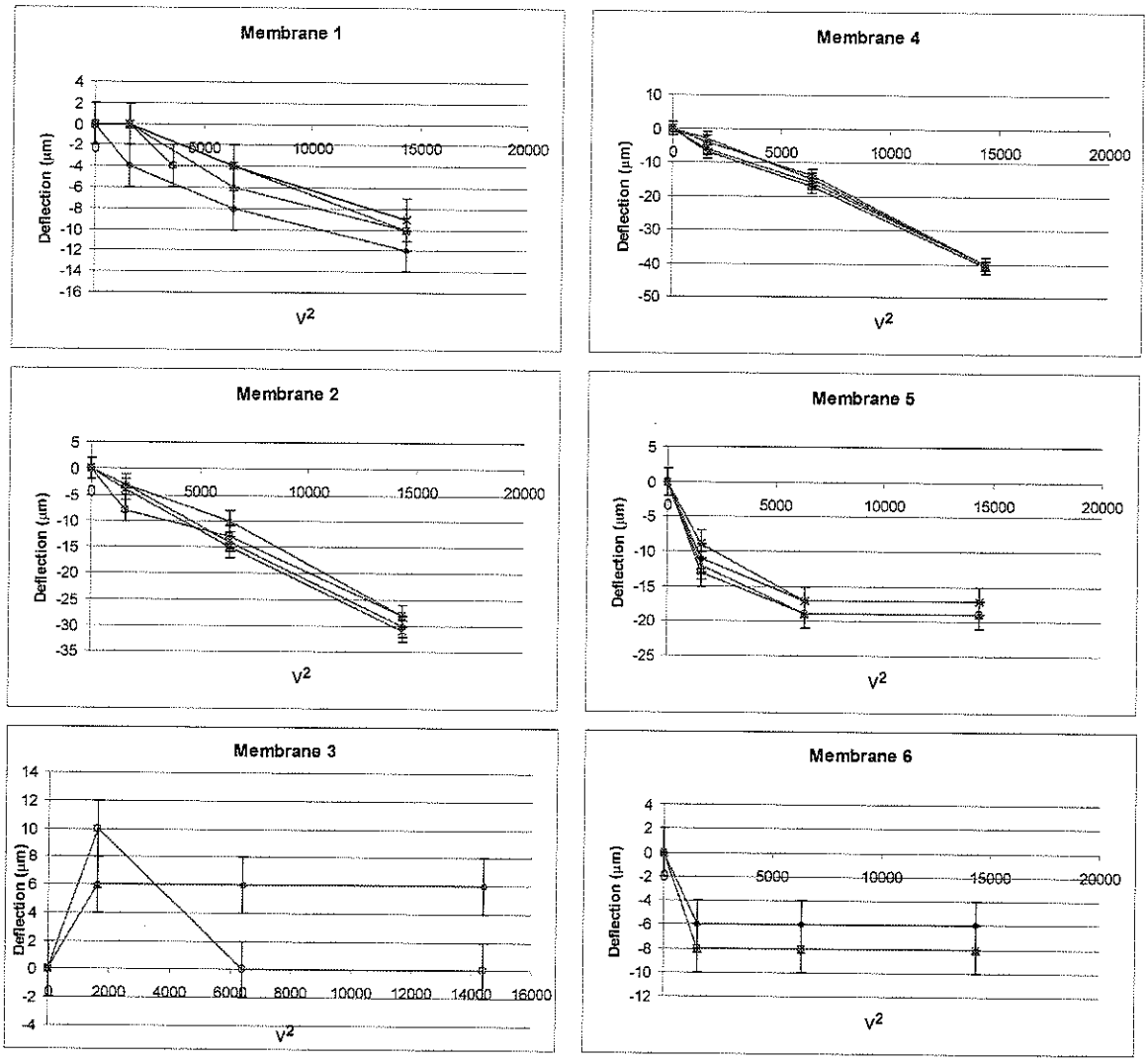

Figure 6 - 14: Membrane deflection vs. applied voltage squared.

Unfortunately, membranes 3 and 6 bottomed out (Figure 6 - 14) during this experiment. An effect which is likely seen because the membranes are actuated from the bottom, hence the electric field force is additive with gravity, instead of ***opposition*** like the previous tests.

Using the average value for 0 and 120 Volts, and assuming the membrane is originally in plane with the surrounding copper z_0=0, we can calculate the spring constants of membranes 1, 2 and 4. Solving equation 3.16 with a non-uniform dielectric consisting of a 400μm air gap and 100μm AF-45 insulating glass plate (ε_{glass}= 6.2) we have

$$F_z = \frac{1}{2}\frac{\varepsilon_{air}\varepsilon_{glass}}{\varepsilon_{air} + (\varepsilon_{glass} - \varepsilon_{air})\dfrac{d_{air}}{d_{air} + d_{glass}}}\varepsilon_0 A\left(\frac{V_{DC}^2}{z^2}\right) \quad \text{N} \tag{6.21}$$

$$F_z = \frac{1}{2}\frac{1*6.2}{1 + (6.2-1)\left(\dfrac{400}{400+100}\right)}\left(8.854\times10^{-12}\right)\left(6.25\times10^{-6}\right)\left(\frac{120^2}{\left(500\times10^{-6}\right)^2}\right) \quad \text{N} \tag{6.22}$$

$$F_z = -1.9149\times10^{-6} \tag{6.23}$$

And obtain the values in Table 6 - 4.

Table 6 - 4: Estimated spring constants for membranes 1, 4, and 2

Membrane	Δz (m) (measured)	F_{DC} (μN) (theory)	k N/m ($F_{DC}/\Delta z$)
1 (2.1mm beams)	-10.25μm	-1.9	0.187
2 (1.4mm beams)	-29.25μm	-1.9	0.066
4 (2.1mm beams)	-40.25μm	-1.9	0.048

Table 6 - 4 comes from the assumption that the wafer was 400 μm thick and the membrane initially lay in plane with the surrounding copper. If the membrane was offset some initial distance z_0, the force exerted on the membrane and the resulting spring constant would increase substantially.

Based on these estimated spring constants, the deflection of membrane 4 with a 17kV/m field would be 0.17μm based on the relationship in equation 6.24 below.

$$\frac{F_{DC}}{F_{optical}} = \frac{k\Delta z_{DC}}{k\Delta z_{optical}} = \frac{\frac{1}{2}\varepsilon_r\varepsilon_0 A E_{DC}^2}{\frac{1}{2}\varepsilon_{eff}\varepsilon_0 A E_{optical}^2} \quad \text{N} \tag{6.24}$$

Simplifying and then solving for Δz_{DC} we have:

$$\Delta z_{DC} = \Delta z_{optical} \frac{\varepsilon_r E_{DC}^2}{\varepsilon_{eff} E_{optical}^2} \tag{6.25}$$

Giving,

$$\Delta z_{DC} = (-40.25\mu m) \frac{1\left(\frac{120}{7\times10^{-3}}\right)^2}{1.2\left(\frac{120}{0.5\times10^{-3}}\right)^2} = -0.17\mu m \tag{6.26}$$

Thus we have an approximate deflection for the DC test of membrane 4 to be +0.17μm. Where the sign change comes from the forces being orientated in opposite directions.

Following the above derivation (6.24 to 6.26) with an atmospheric field of 3MV/m, we obtain a Δz of 5.2mm. Which implies that stiffer springs would likely be required to measure the upper range of electric fields expected in practice.

In future work, more care can be taken to measure the total deflection of each spring. Besides measuring the rest position of the membranes, it will also allow for the effect of angular changes (equation 5.4) to be accounted for. However, the 4μm error due to backlash (mechanical slip) of the optical microscope make measurements using this apparatus challenging.

Chapter 7: FUTURE WORK

7.1 STRESS

The spring design of the transducer was dominated by concerns about stress. It is important to note however that this problem is primarily a function of the manufacturing technology chosen. Different manufacturing techniques which allow you to control intrinsic stress such as sputtering will allow designers more freedom in how to suspend the membrane. However, the two equal length beams used in this design did resolve the problem of releasing stress within the transducer springs.

7.2 CARE AND HANDLING

The membranes survived testing well, however during subsequent demonstrations and storage (on a klim wipe), they dropped noticeably out of plane with the surrounding copper structure. This could be a tell-tale sign of the springs catching on the wipe, charging effects in the Petri-dish, or the connections between beams breaking during handling (Figure 6 - 3). To prevent this, a small frame to lift up the wafer and protect the springs should be considered.

7.3 ELECTRONIC CIRCUIT

The original electronics design was based heavily on recommendations from literature, support staff, and professors. In the culmination of this information, a current path to ground for the V^+ inputs in the summing/difference junction amplifiers was omitted. Although the net effect on the system was minimal because of the resistance values chosen, the problem could be avoided in subsequent runs altogether.

Secondly, because of the low frequency of membrane operation, the capacitive filtering used to smooth out noise could be eliminated or reduced. This would simplify both the design and manufacture of future projects.

7.4 Future Setup

As an alternative setup and recommendation for future work, this sensor was very sensitive to low frequency vibrations and air currents. Subsequent designers will likely find much shorter springs viable and less prone to vibration. The resulting higher spring constants would increase the resonant frequency providing some immunity to noise.

To combat air drafts, the system will need a housing which both completely surrounds the sensor without isolating it from the electric fields to be measured. Most likely, this will take place in a conductive chassis with a periodically grounded conductive top.

Finally, nulling the photodetector position is an important aspect of a beam bounce based sensor. Future designers should consider how to mount the X-Y stage directly to the chassis. During testing, torque from turning the adjustment screws and slip in the mechanism made offsets less then ±200mV hard to achieve. Additionally, the X-Y stage represented a heavy mass on the end of a mechanical arm. Thus, it's own vibrations likely contributed to the noise envelope of the system.

Chapter 8: CONCLUSIONS

This proof-of-concept was a success. It met the stated goal of demonstrating a micromachined electric field sensor.

The eight-spring design presented in section 5.1 supported a 500μg copper/silicon mass. An optical beam bounce system measured the membrane deflection allowing both AC and DC fields to be measured. Unlike other field sensors, the presence of ionic space charge should not cause drift in this device. In the proof of concept, the membrane was connected directly to ground. However, because the small forces involved, this sensor is prone to noise, especially from low frequency vibration. The optoelectronic circuit performs well, measuring picometers of movement. Development as a whole was a success, the micromachined parts survived fabrication, testing, and general use better then expected. The test platform worked reliably and has potential to be used in future research. Finally, the testing was a success. Working from the results of membrane four, 7kV/m resolution was obtained in DC mode, while 60V/m was obtained in AC mode. However, an astounding 1/3 V/m resolution was obtained in the biased AC testing. As a proof-of-concept, this design is worthy of future consideration.

APPENDICIES

Appendix 1: MEMBRANE CLOSE-UPS

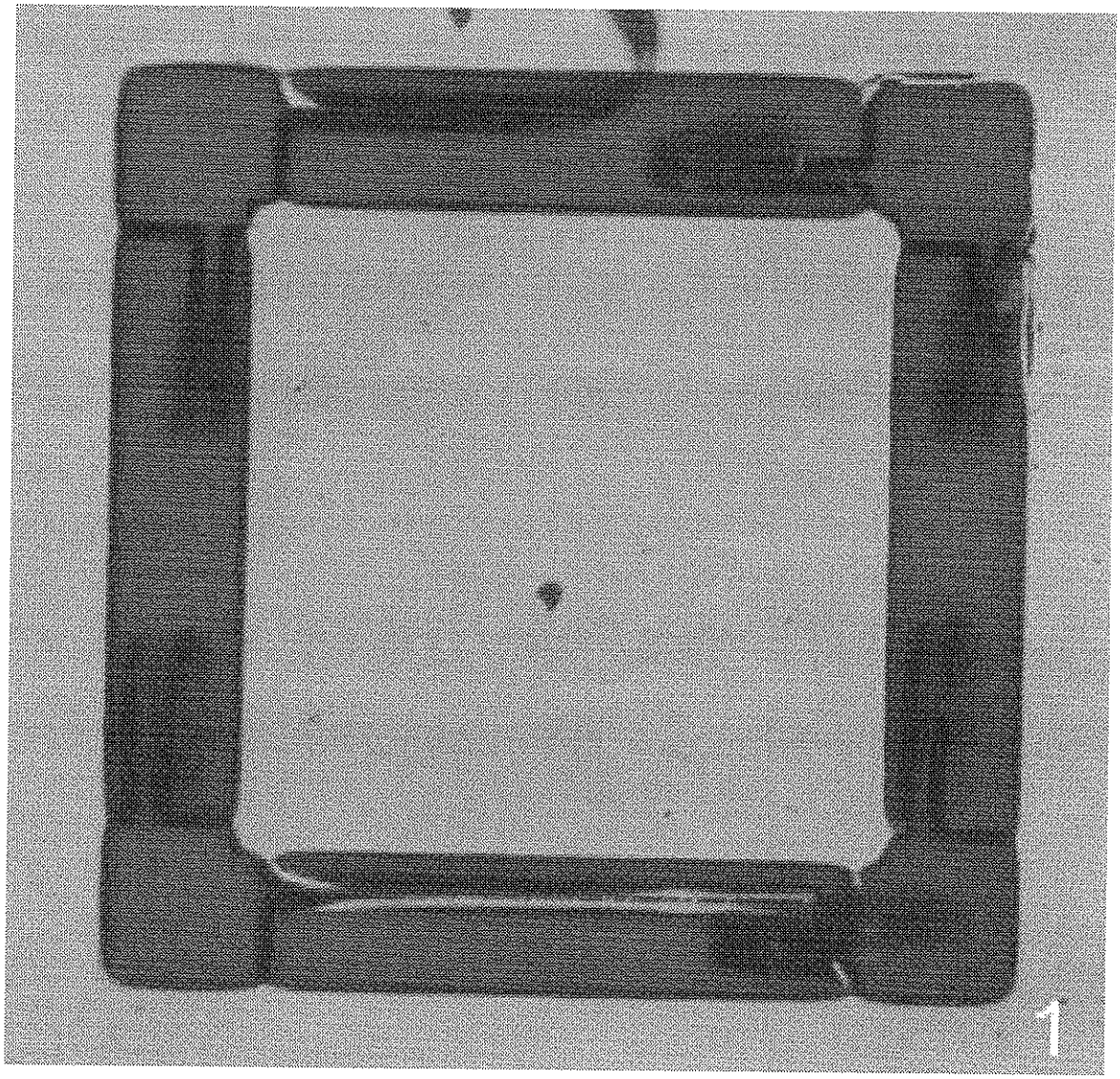

Figure A1 - 1: Membrane 1.

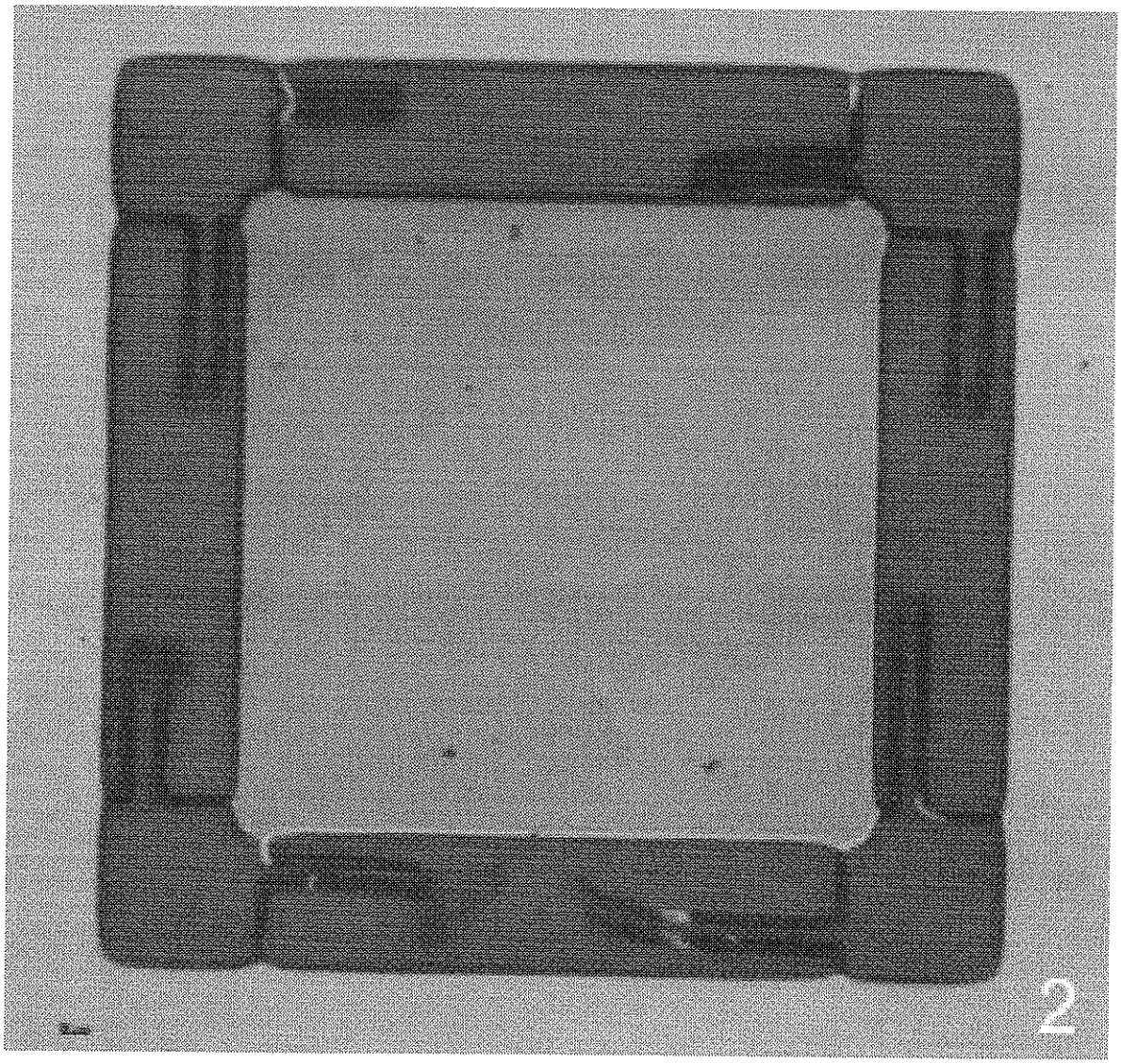

Figure A1 - 2: Membrane 2.

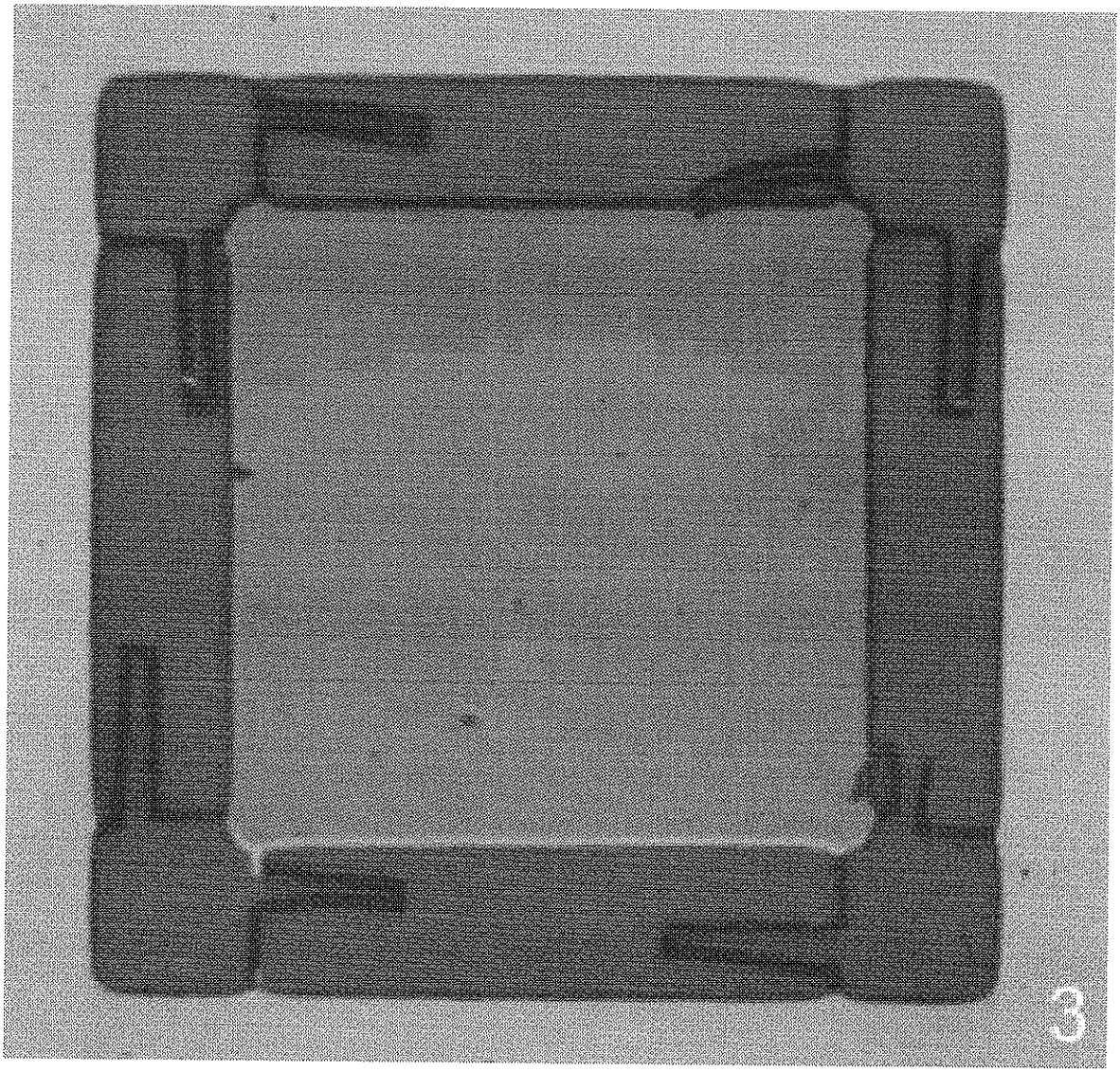

Figure A1 - 3: Membrane 3.

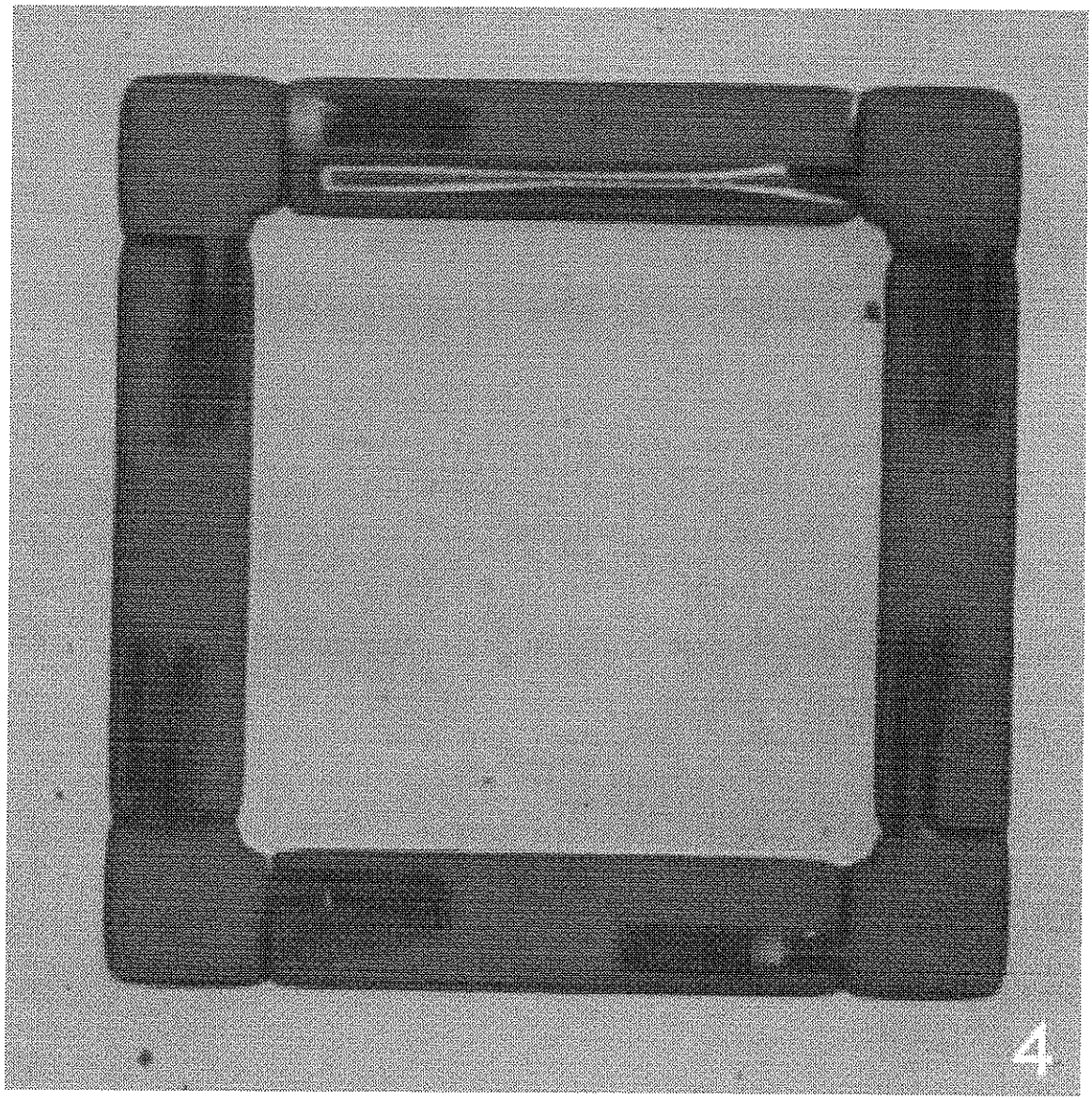

Figure A1 - 4: Membrane 4.

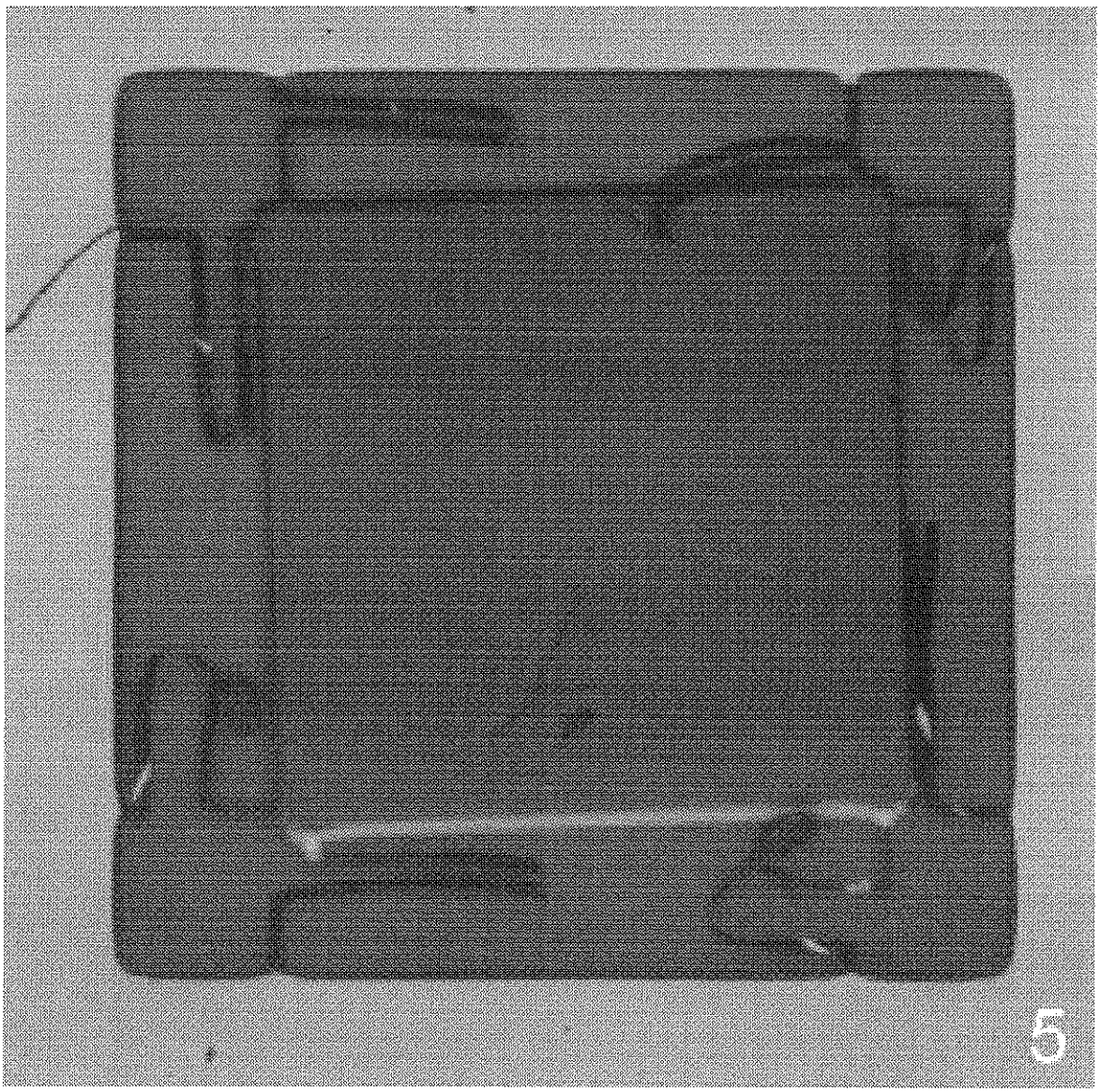

Figure A1 - 5: Membrane 5.

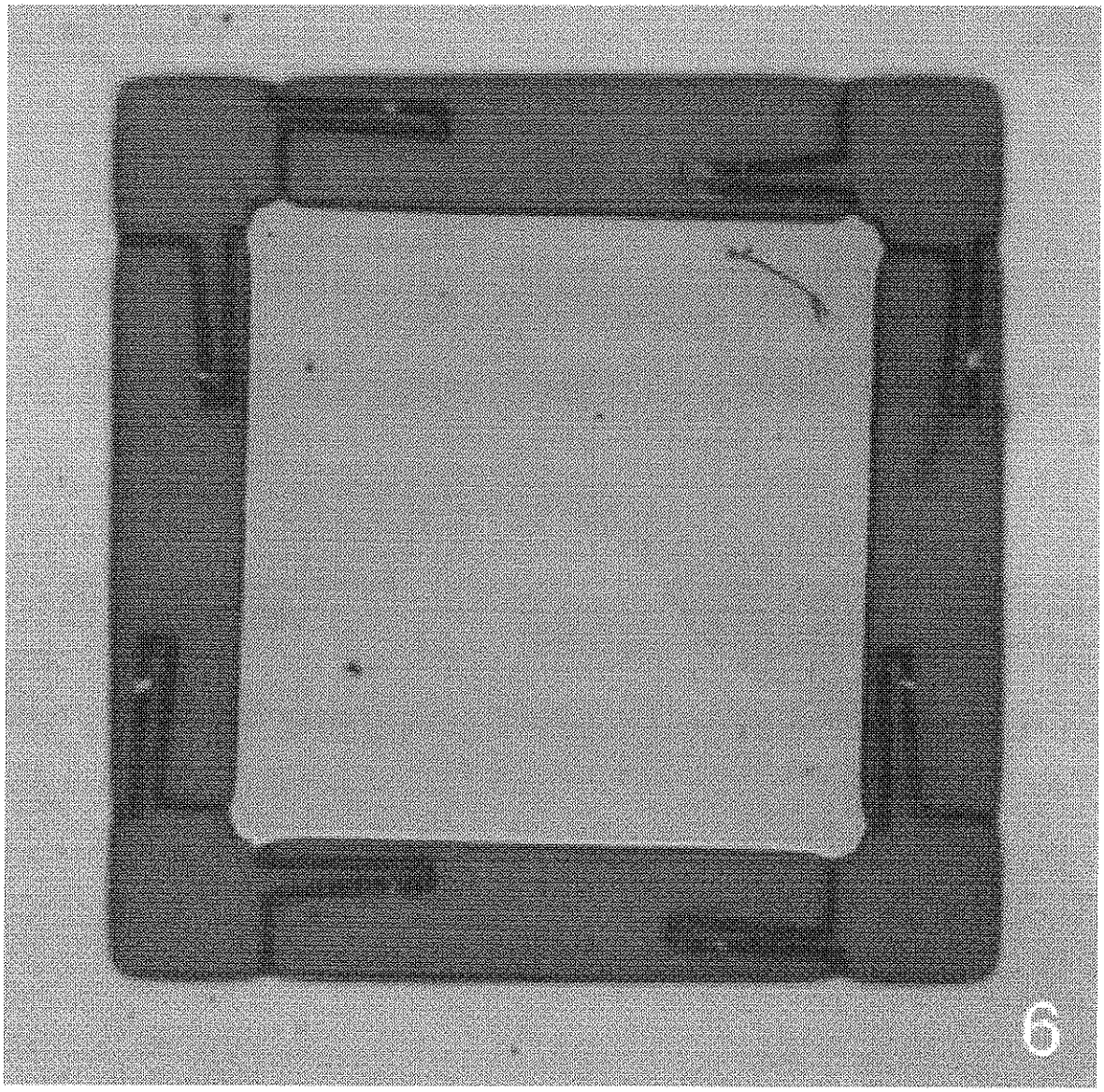

Figure A1 - 6: Membrane 6.

Appendix 2: OUTPUT GRAPHS

The following are graphs produced in MATLAB of the DC and AC response of the system. Data for these graphs was taken using a 60MHz Agilent digital oscilloscope with 8-bit resolution. Typically, the vertical measurement scale was set to 20mV per division, giving a resolution of 625±312μV per bit.

Graphs A2-1 to A2-18 show the DC pulse response values. The excitation voltage V_{ext}, and measured output voltages V_x and V_y are given for each membrane. All of the runs on each membrane are indexed from 0 (run 0,1,2).

While the remaining graphs (A2-19 to A2-49) show the AC response of each membrane. For the AC case, each membrane was sampled at 1, 10, 20, 30, 40, 50, 60, 70, 80, 90, 100, 110, 120Hz and additional frequencies measure the natural frequency. These AC results are organized to show the RMS response and then the actual measured data. Because of the large number of data sets, groups of 5 plots were used for simplification.

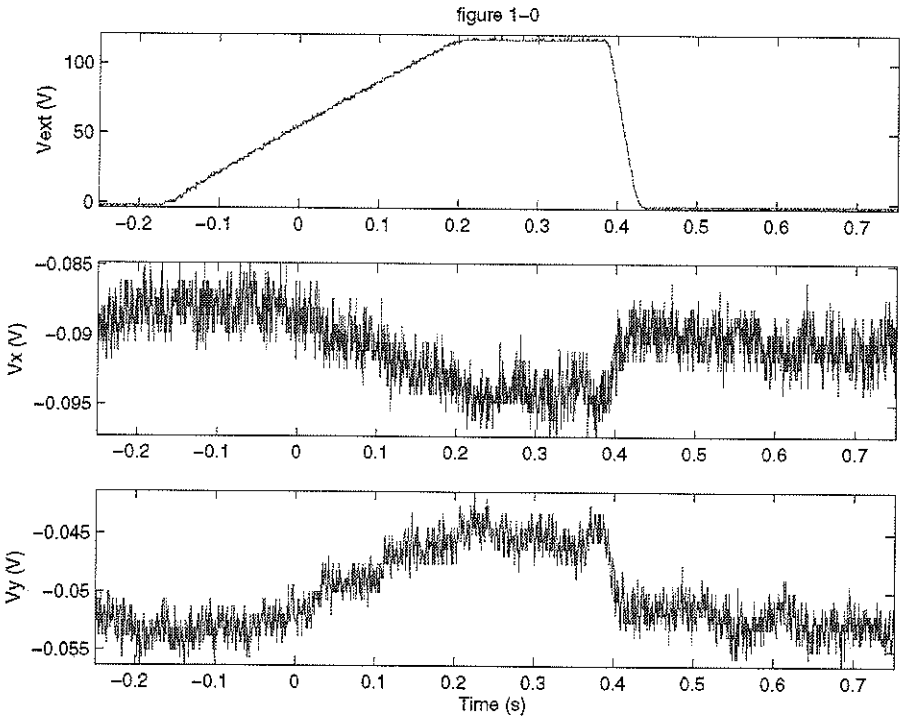

Figure A2 - 1: DC testing, membrane 1, run 0.

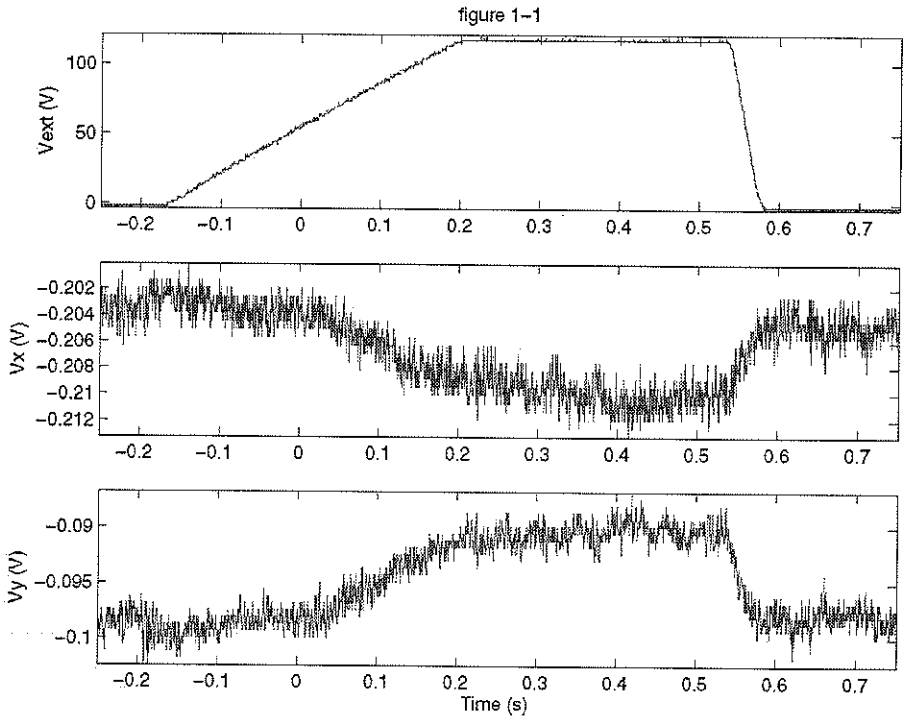

Figure A2 - 2: DC testing, membrane 1, run 1.

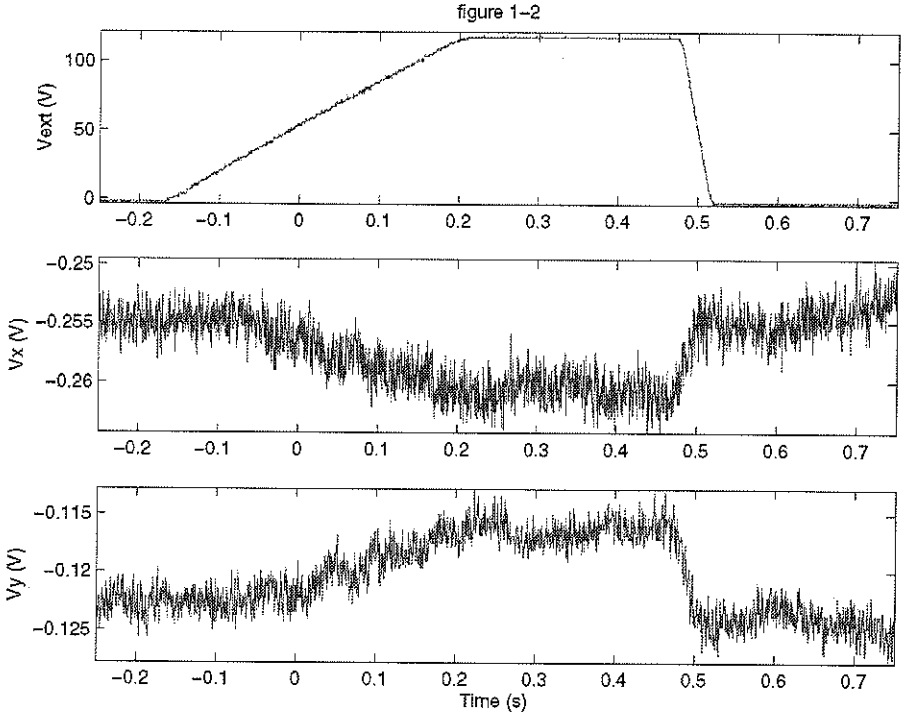

Figure A2 - 3: DC testing, membrane 1, run 2.

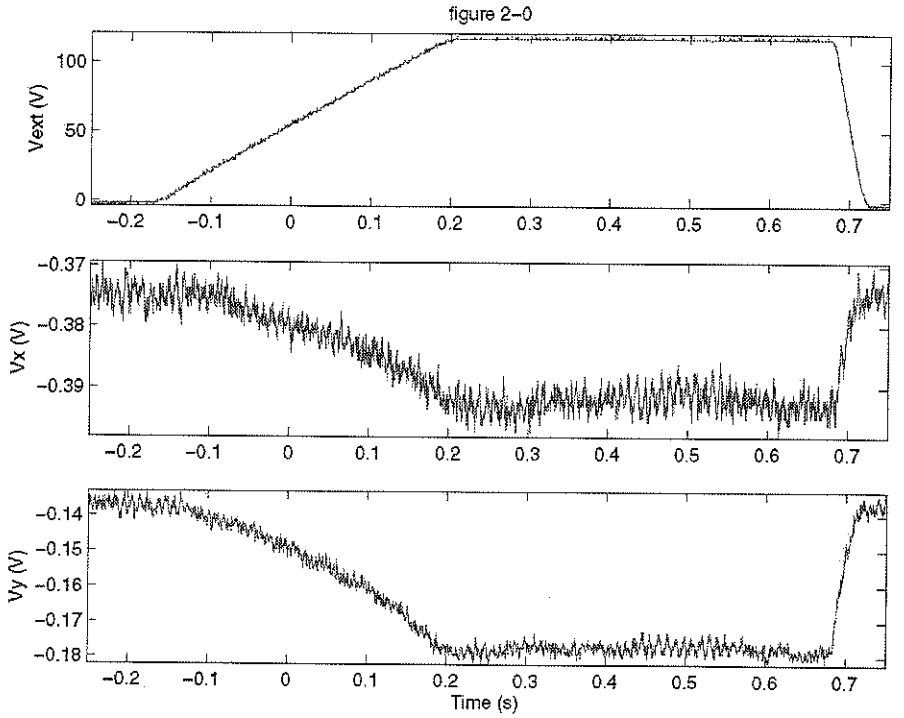

Figure A2 - 4: DC testing, membrane 2, run 0.

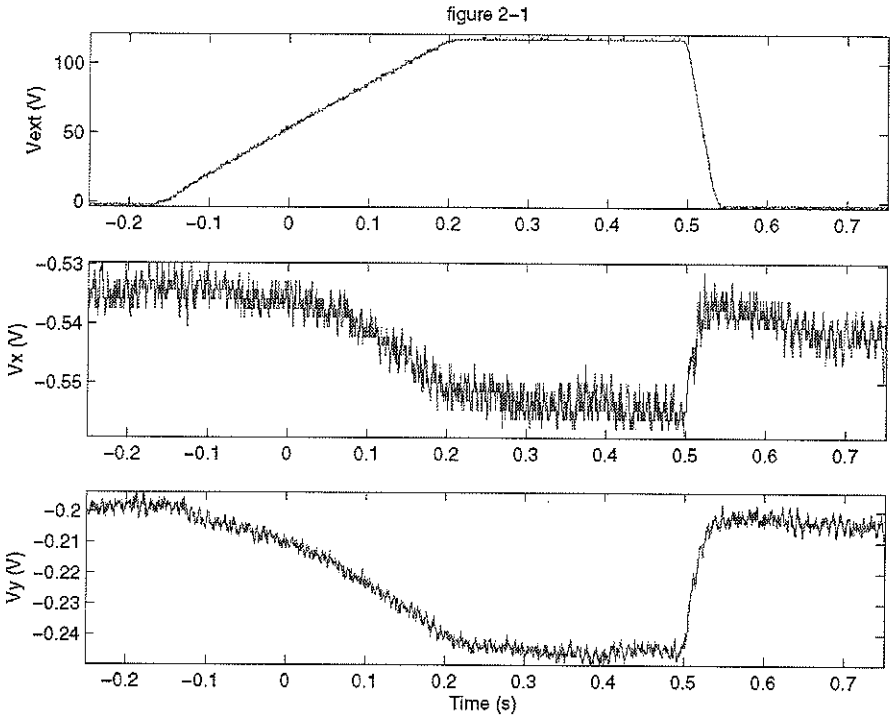

Figure A2 - 5: DC testing, membrane 2, run 1.

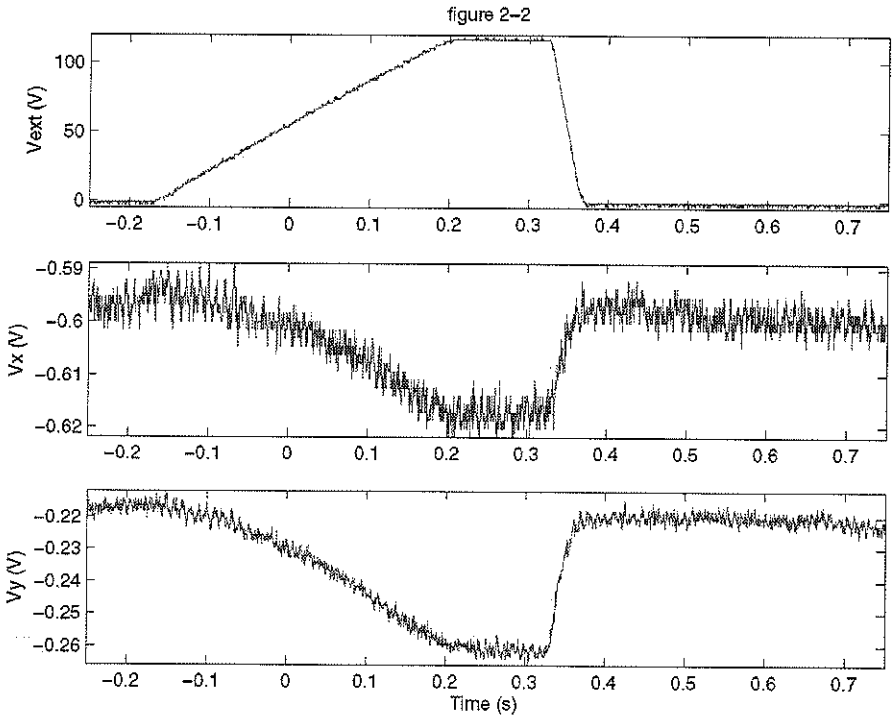

Figure A2 - 6: DC testing, membrane 2, run 2.

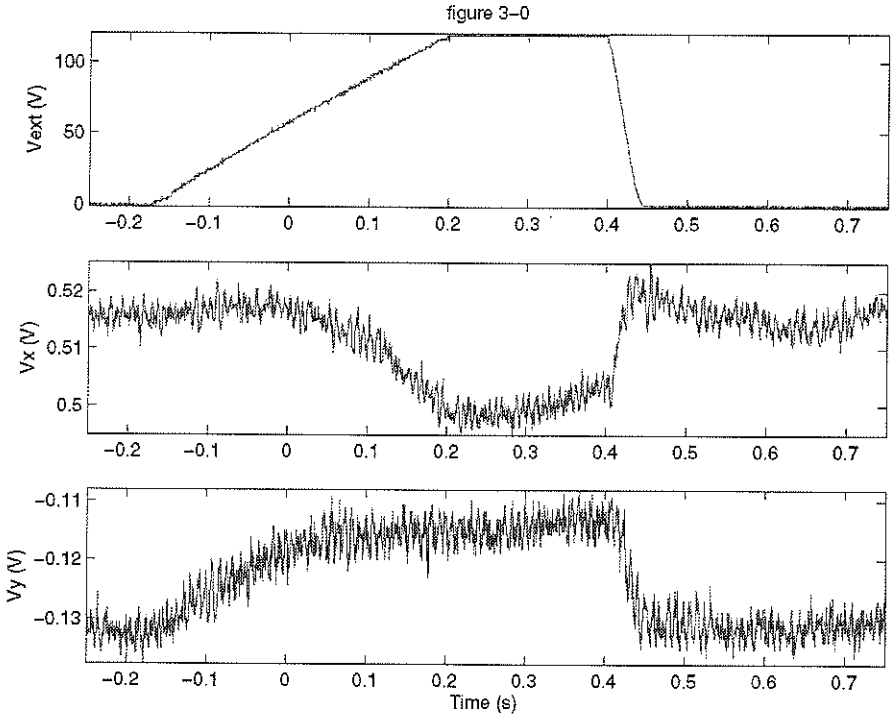

Figure A2 - 7: DC testing, membrane 3, run 0.

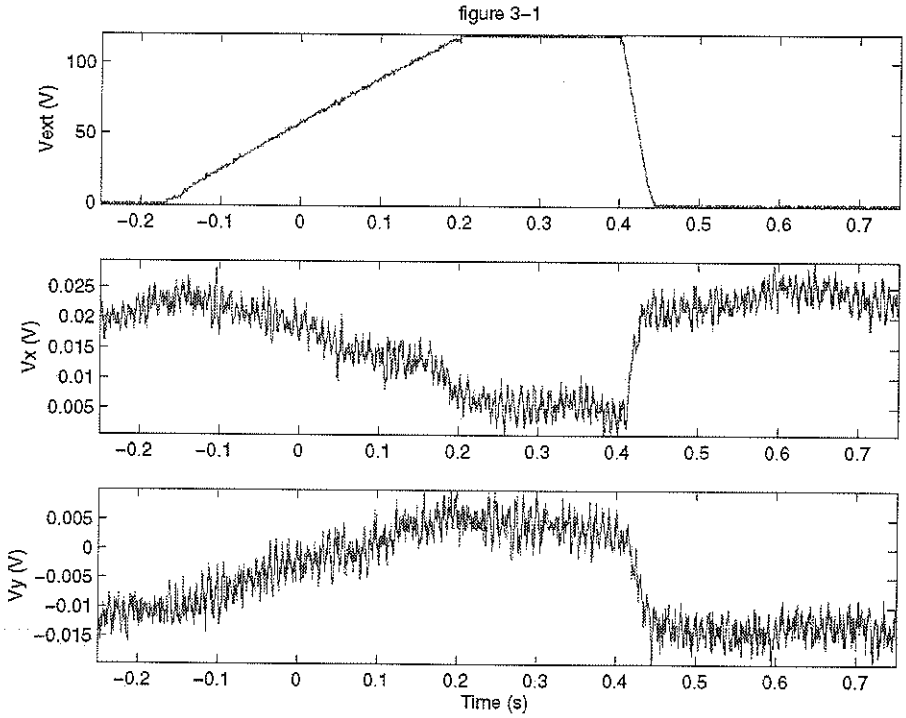

Figure A2 - 8: DC testing, membrane 3, run 1.

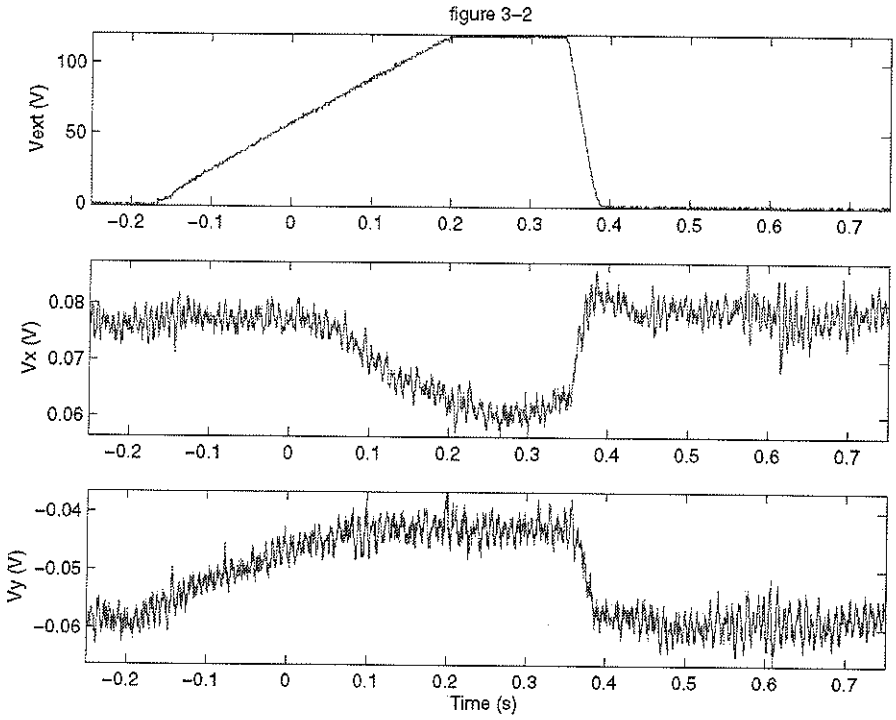

Figure A2 - 9: DC testing, membrane 3, run 2.

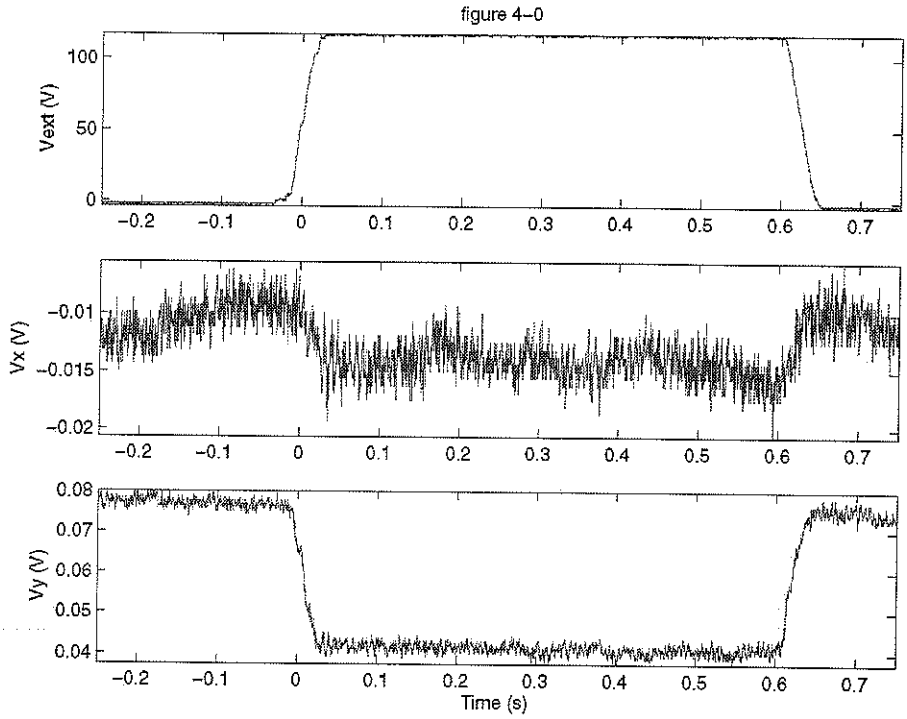

Figure A2 - 10: DC testing, membrane 4, run 0.

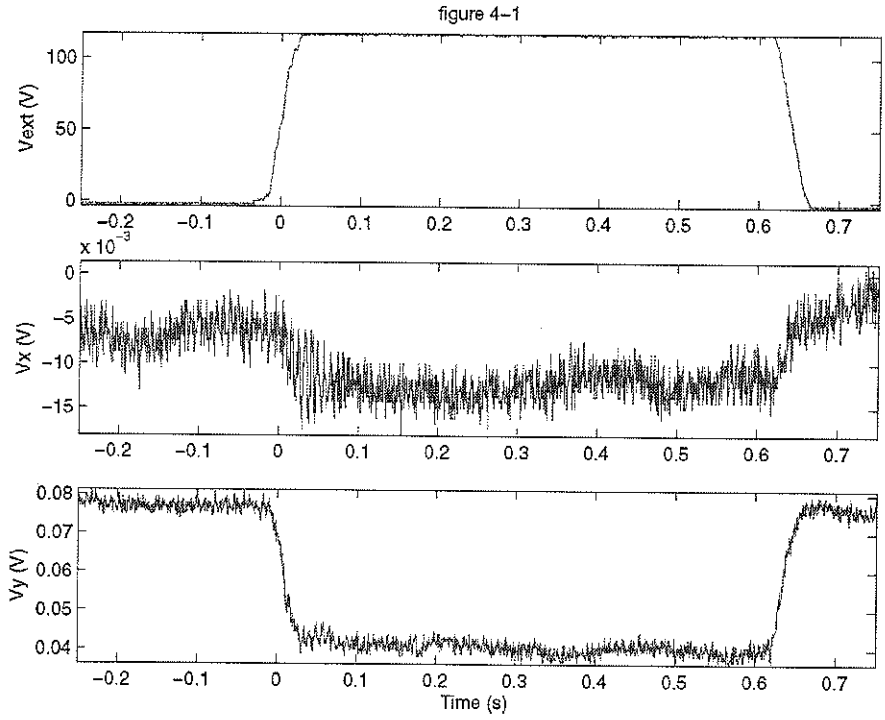

Figure A2 - 11: DC testing, membrane 4, run 1.

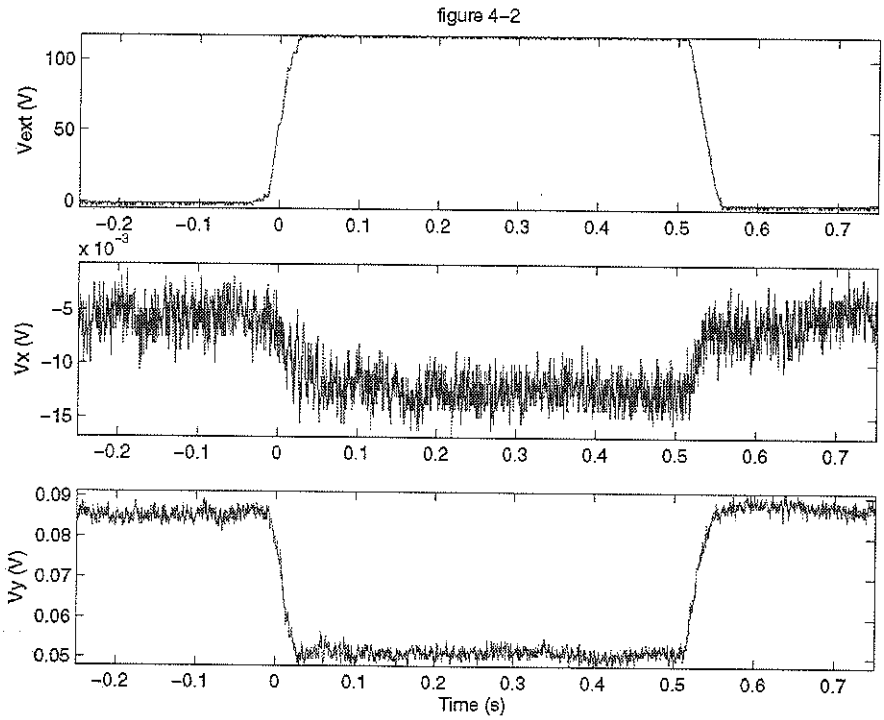

Figure A2 - 12: DC testing, membrane 4, run 2.

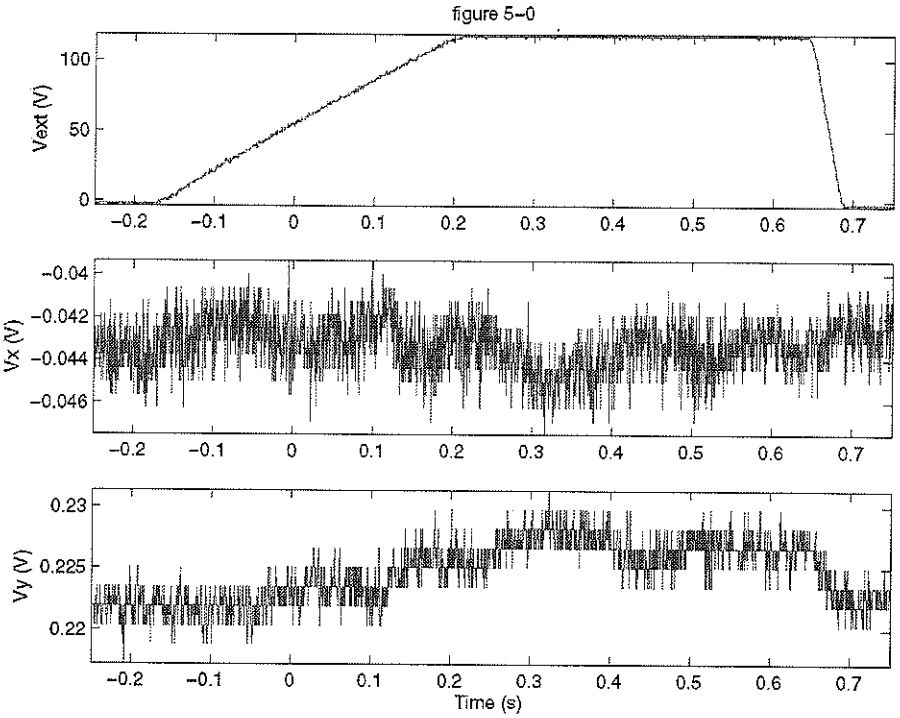

Figure A2 - 13: DC testing, membrane 5, run 0.

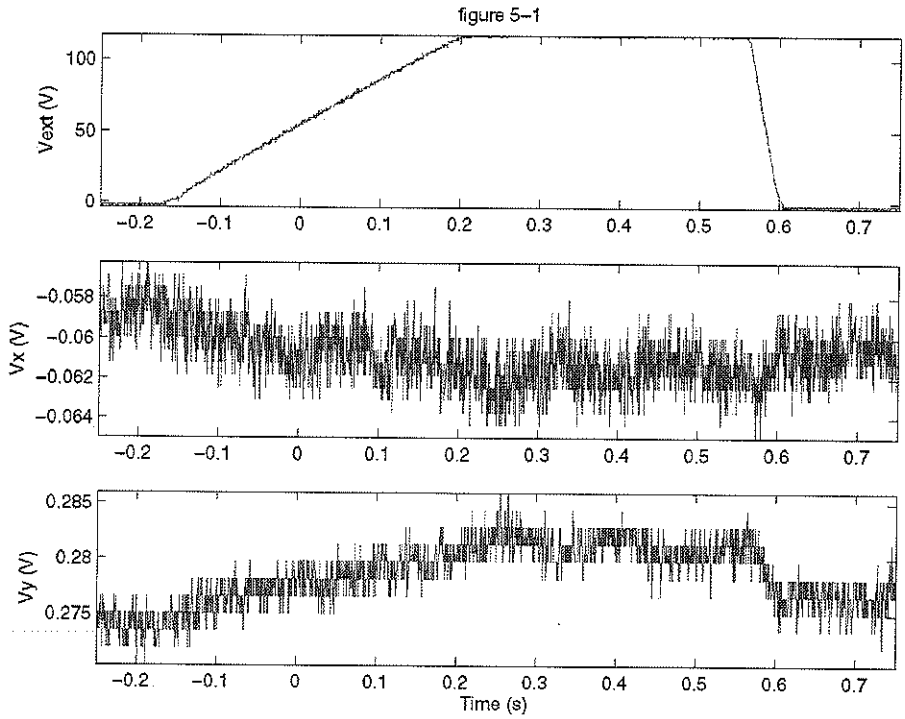

Figure A2 - 14: DC testing, membrane 5, run 1.

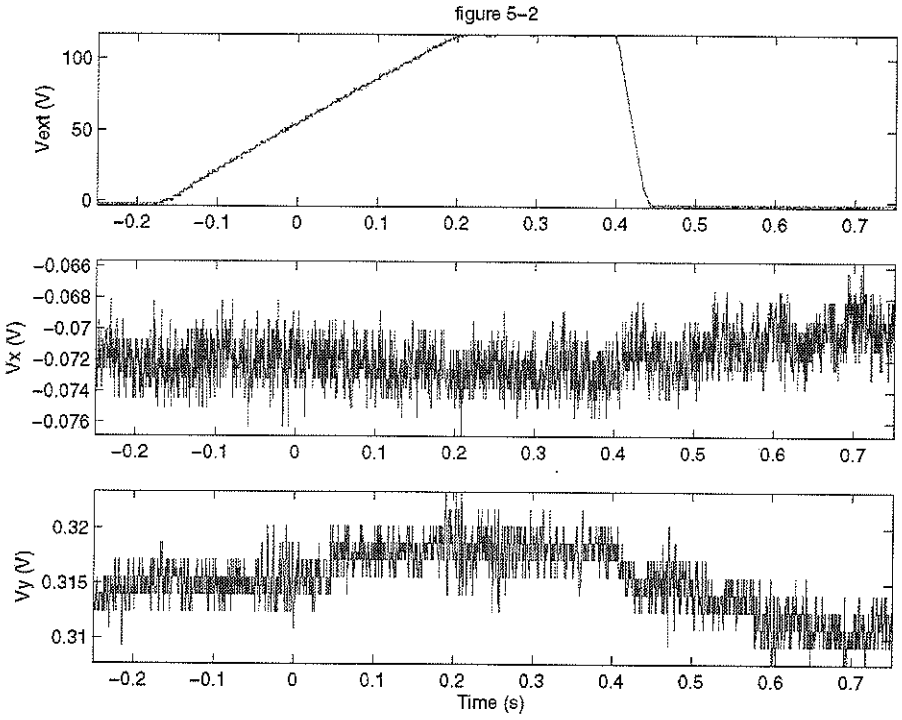

Figure A2 - 15: DC testing, membrane 5, run 2.

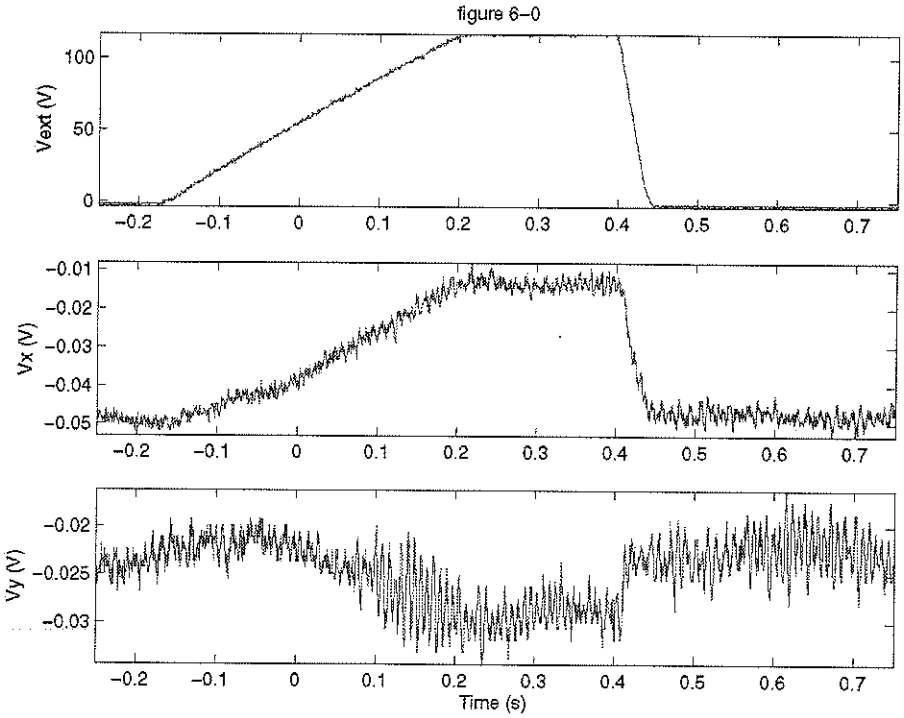

Figure A2 - 16: DC testing, membrane 6, run 0.

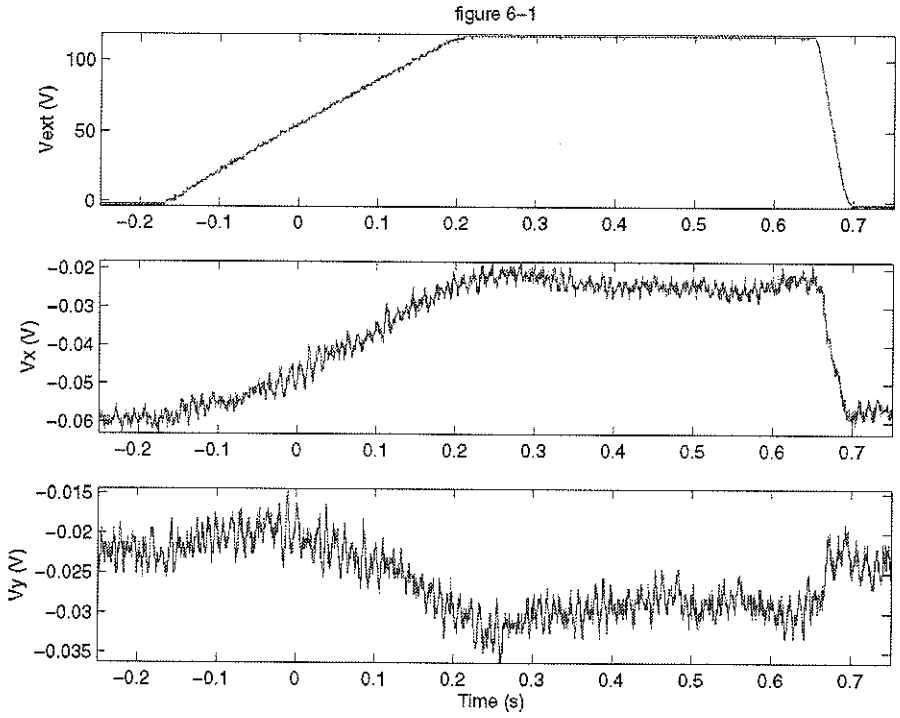

Figure A2 - 17: DC testing, membrane 6, run 1.

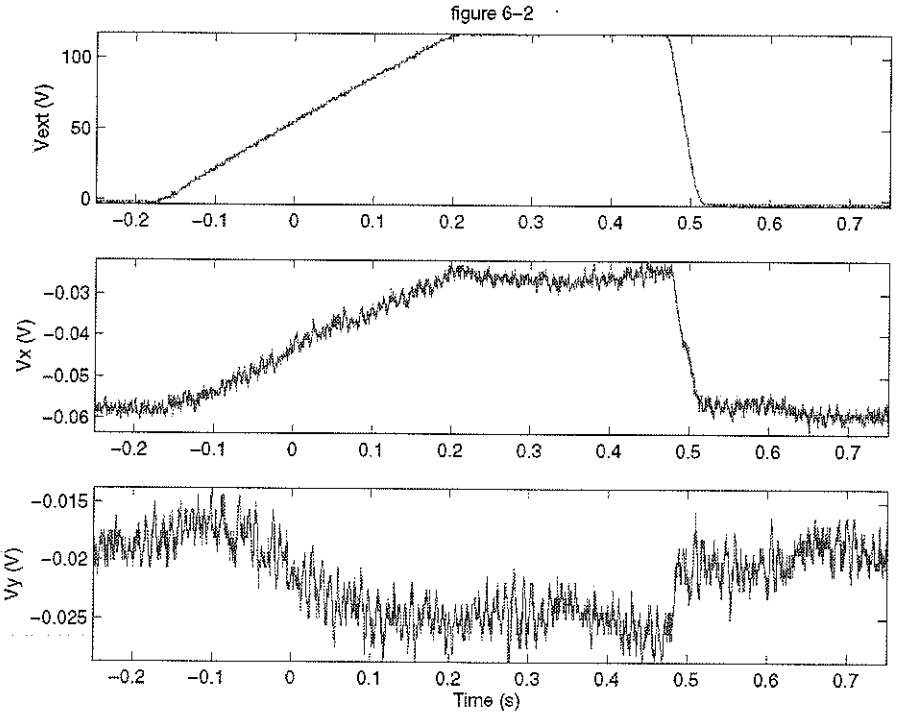

Figure A2 - 18: DC testing, membrane 6, run 2.

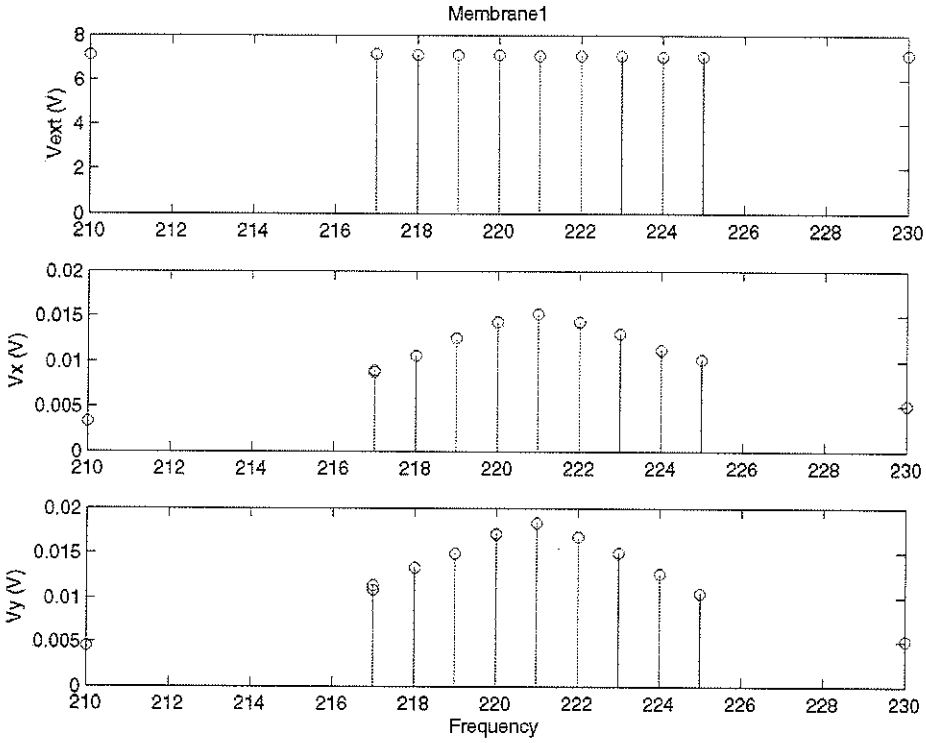

Figure A2 - 19: Membrane 1, RMS frequency response.

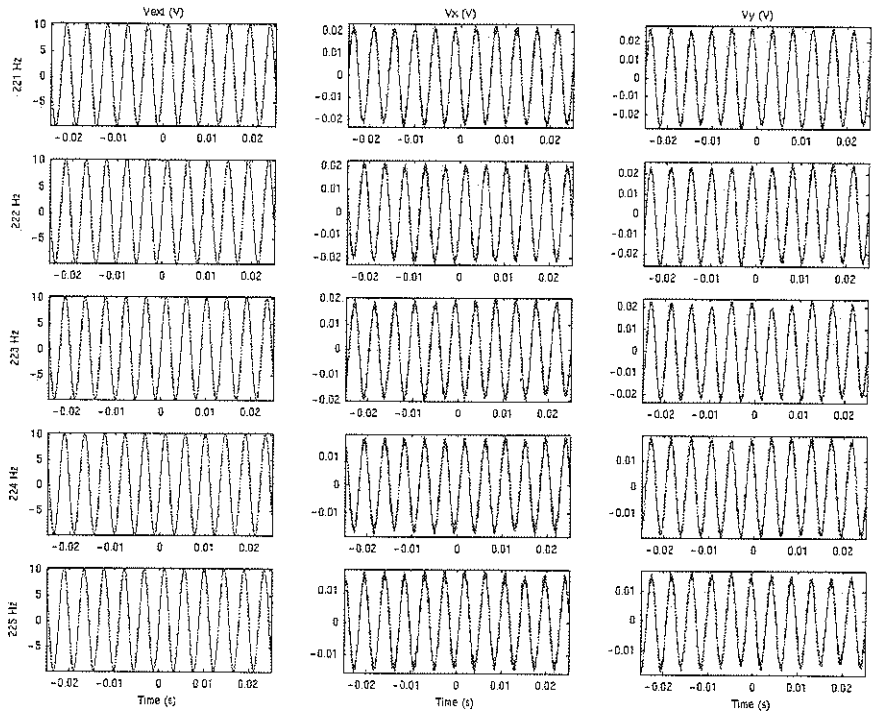

Figure A2 - 20: Membrane 1, AC testing 221 to 225Hz.

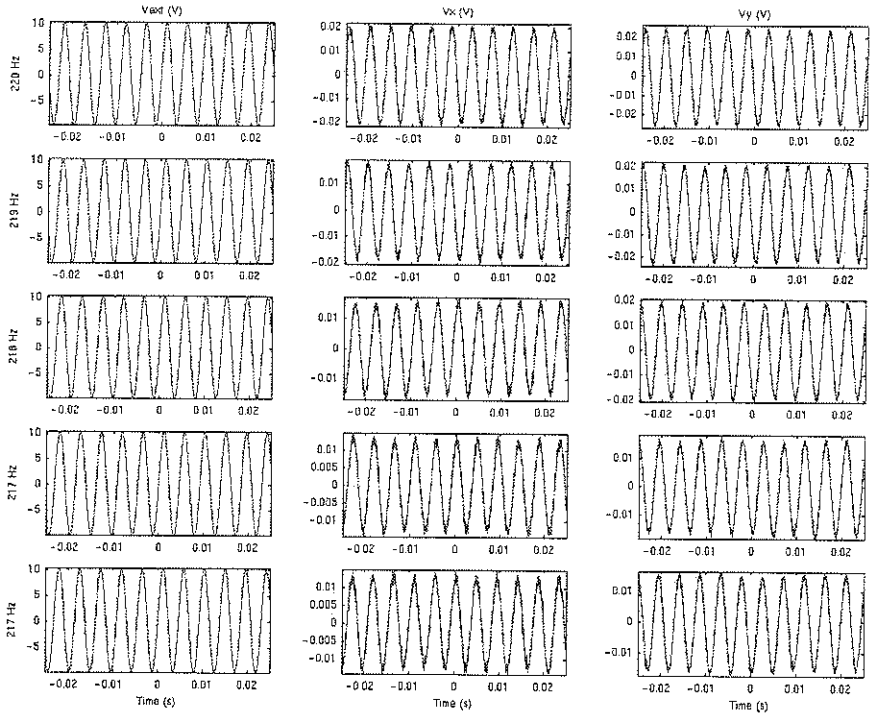

Figure A2 - 21: Membrane 1, AC testing 220, 219,218, 217, and 217Hz.

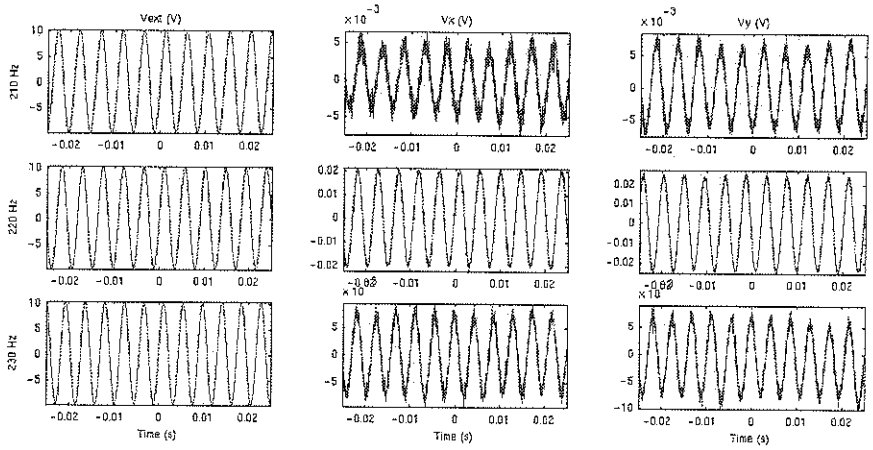

Figure A2 - 22: Membrane 1, AC testing 210 to 230Hz.

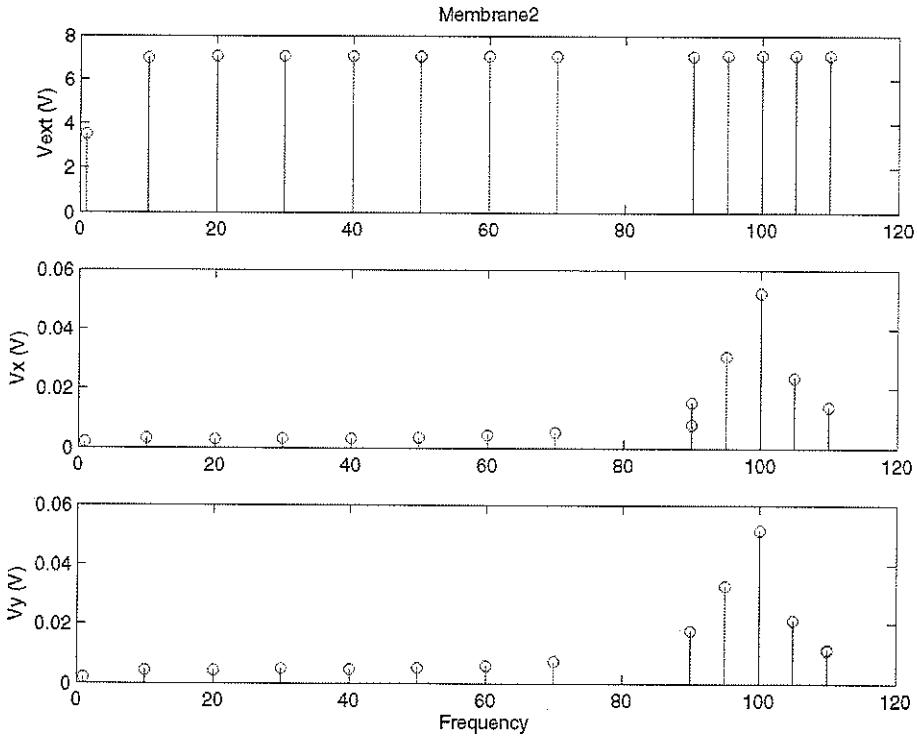

Figure A2 - 23: Membrane 2, RMS frequency response.

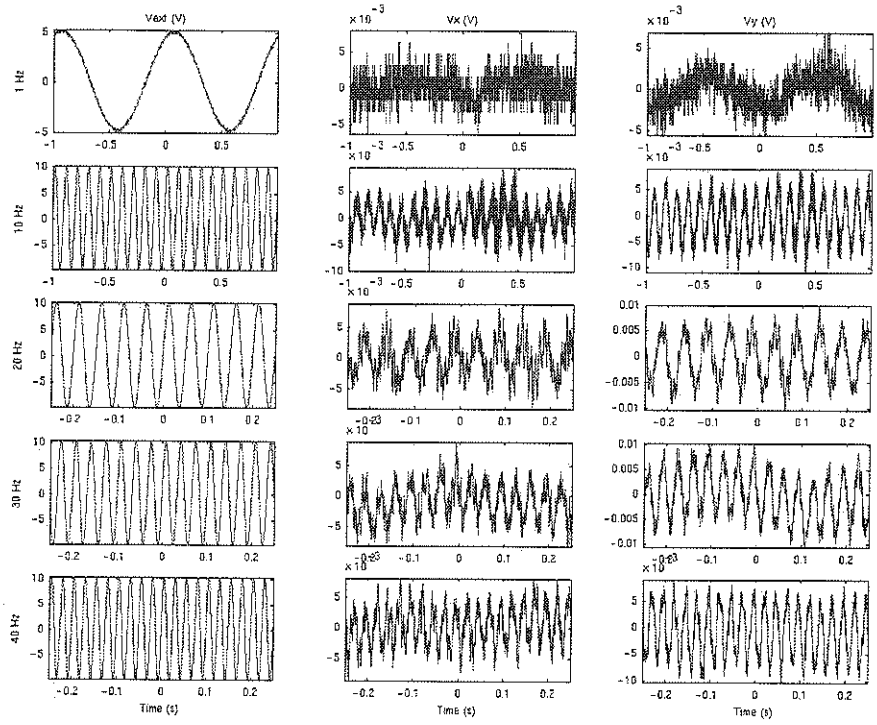

Figure A2 - 24: Membrane 2, AC testing 1 to 40Hz.

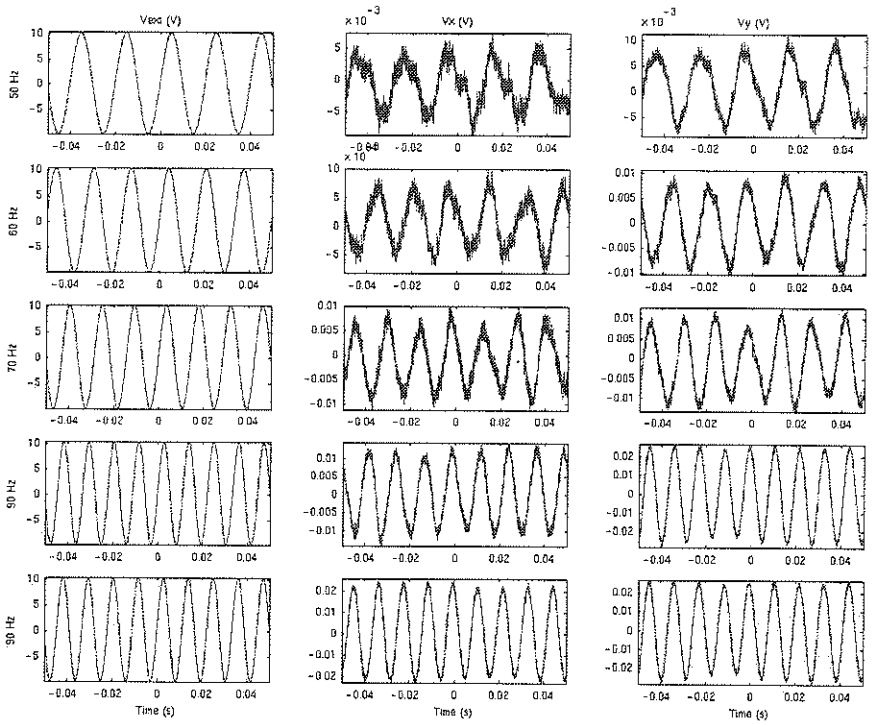

Figure A2 - 25: Membrane 2, AC testing 50 to 90Hz.

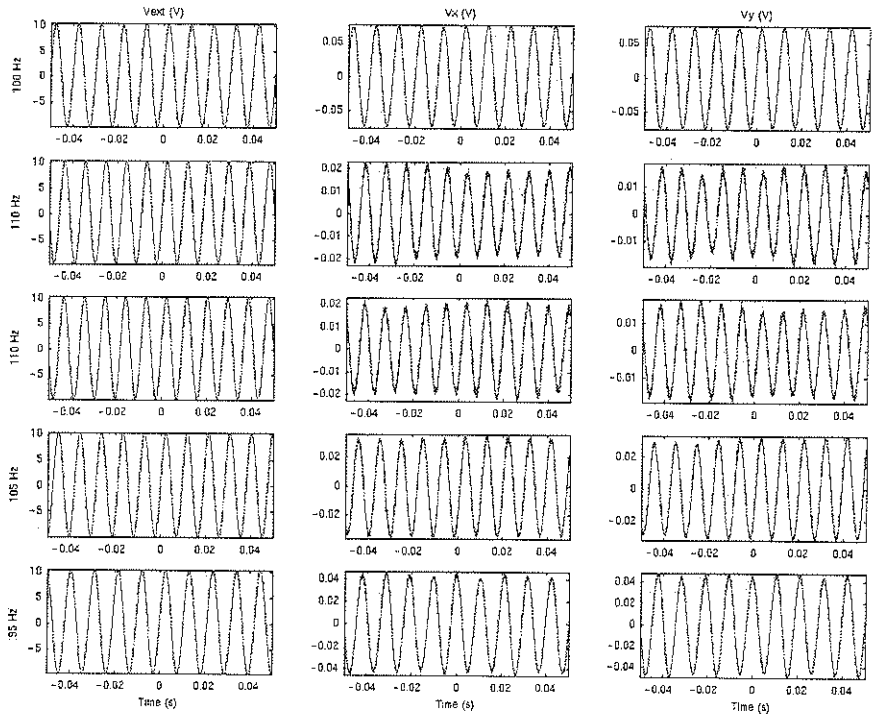

Figure A2 - 26: Membrane 2, AC testing 100, 110, 110 105, and 95Hz.

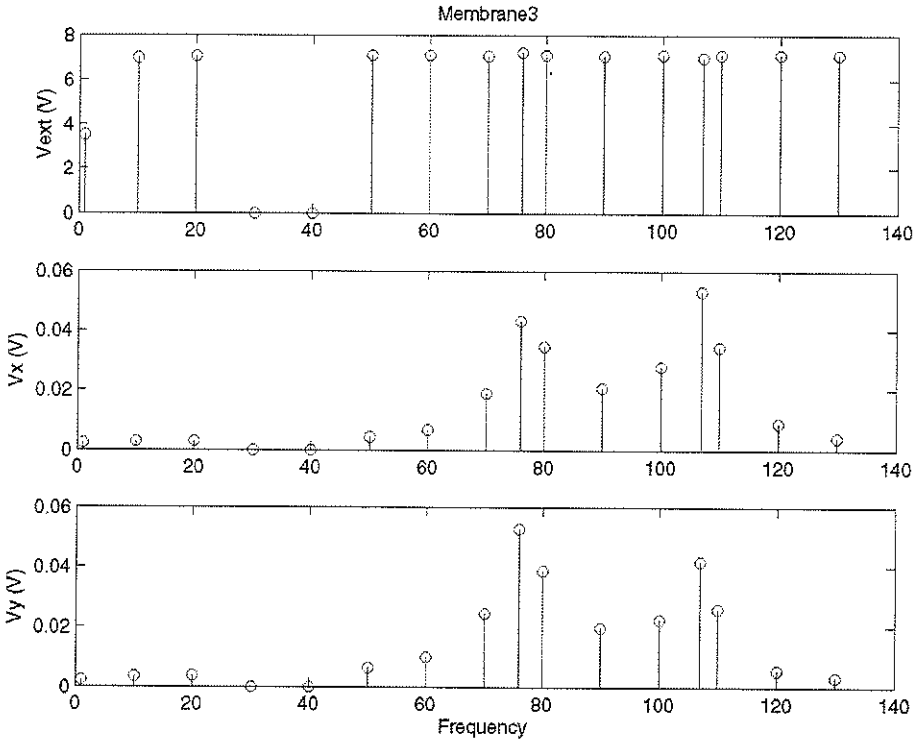

Figure A2 - 27: Membrane 3, RMS frequency response.

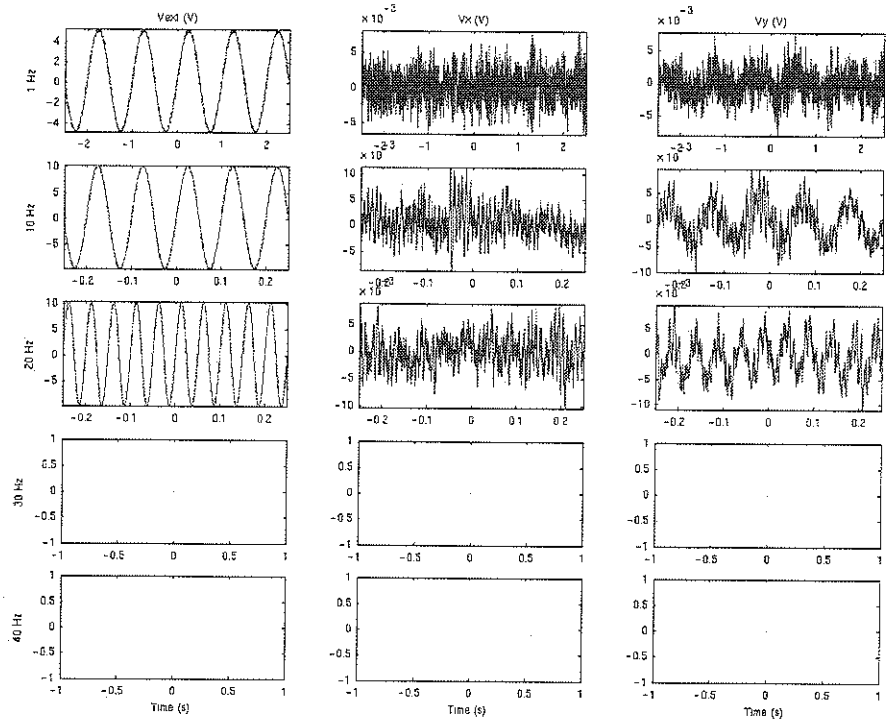

Figure A2 - 28: Membrane 3, AC testing 1 to 40Hz.

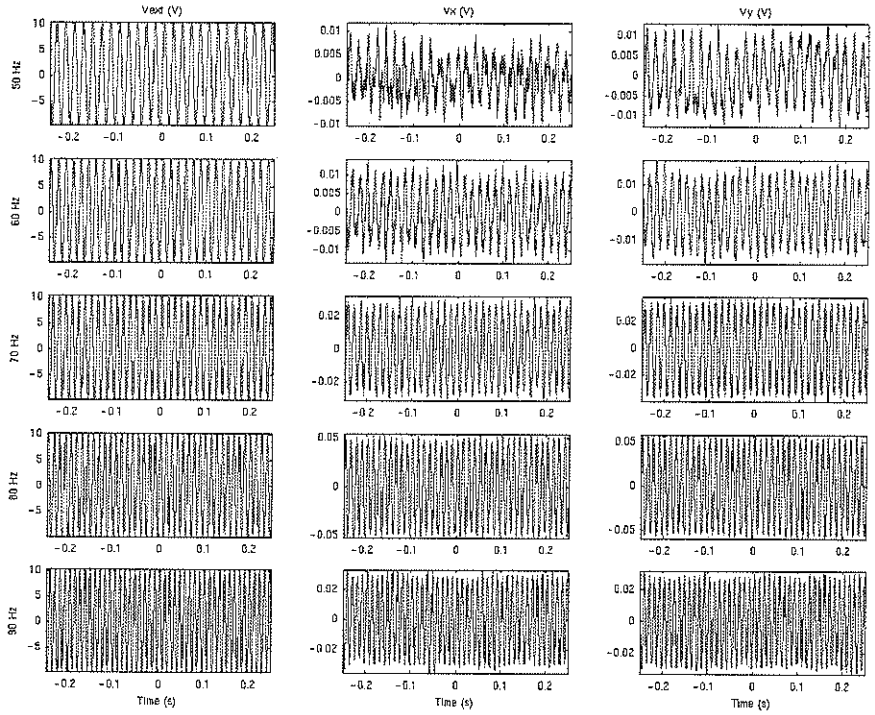

Figure A2 - 29: Membrane 3, AC testing 50 to 90Hz.

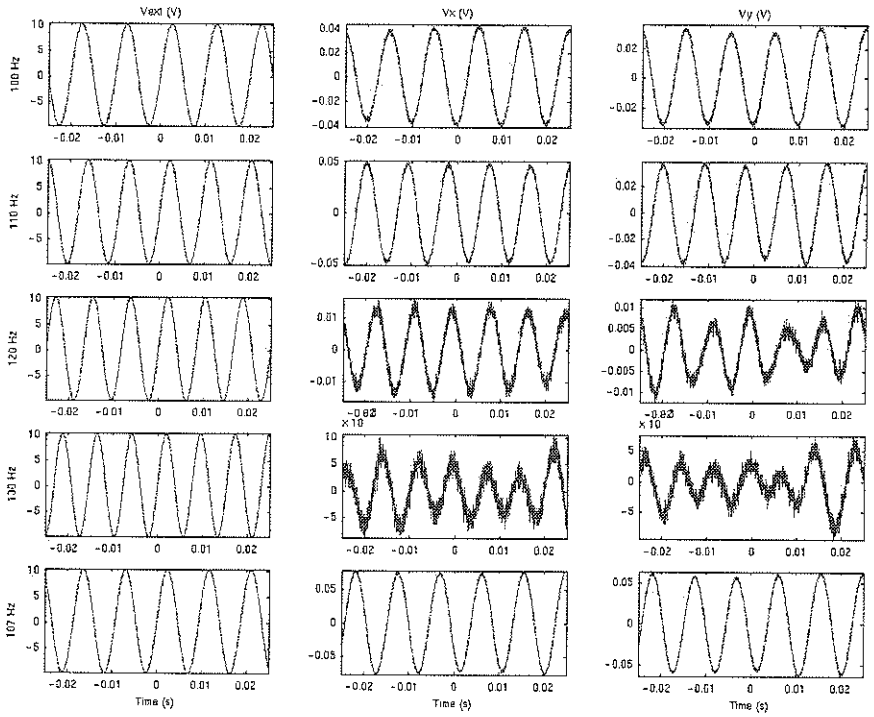

Figure A2 - 30: Membrane 3, AC testing 100, 110, 120, 130, and 107Hz.

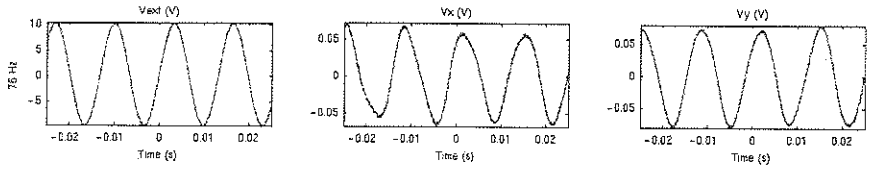

Figure A2 - 31: Membrane 3, AC testing 76Hz.

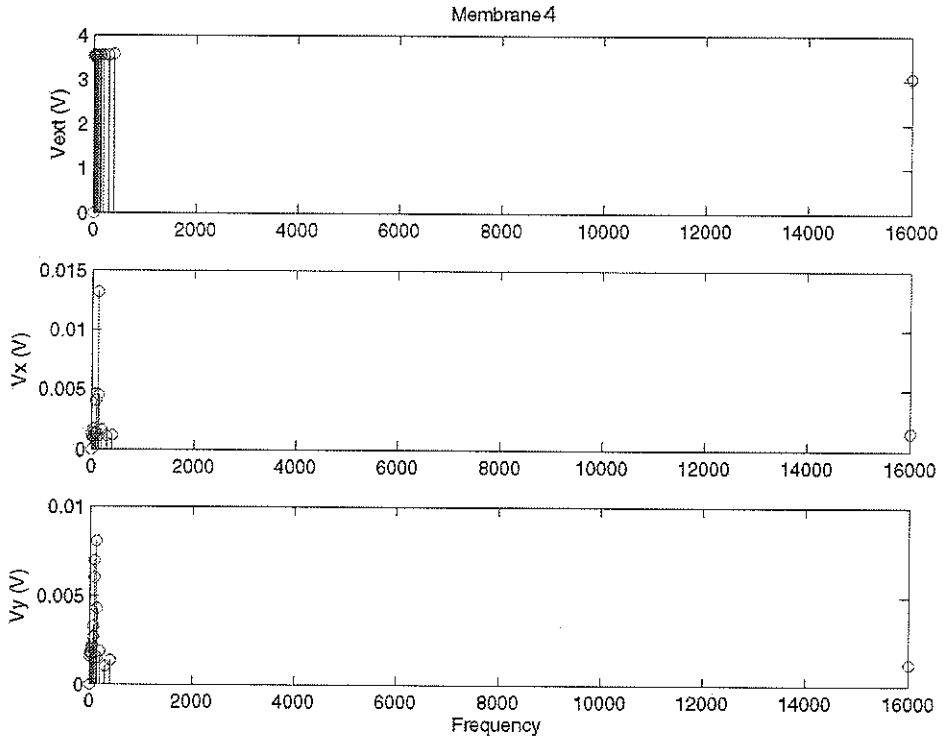

Figure A2 - 32: Membrane 4, RMS frequency response (run1).

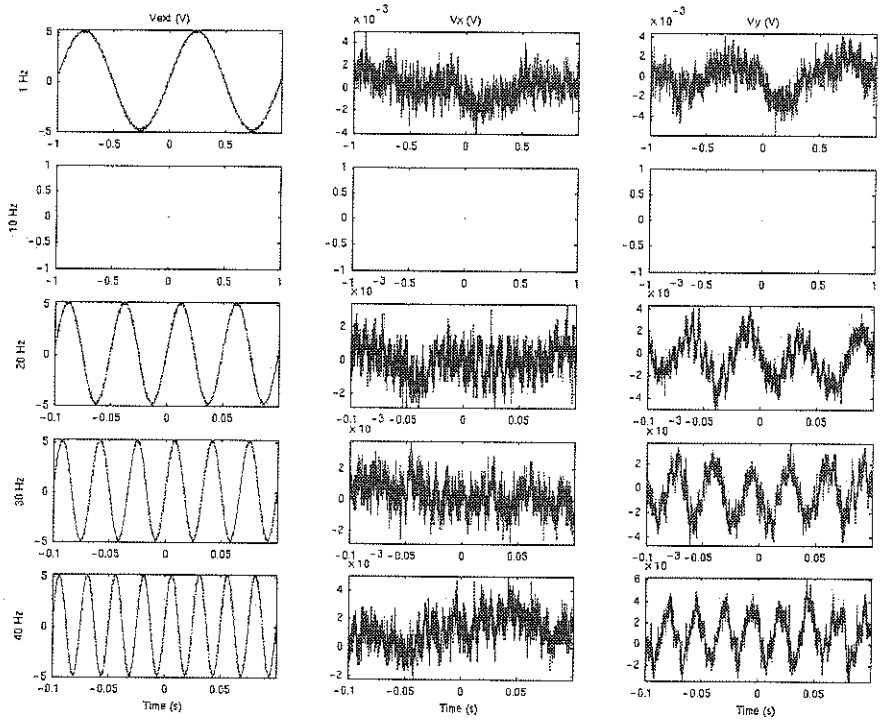

Figure A2 - 33: Membrane 4, AC testing 1 to 40Hz (run1).

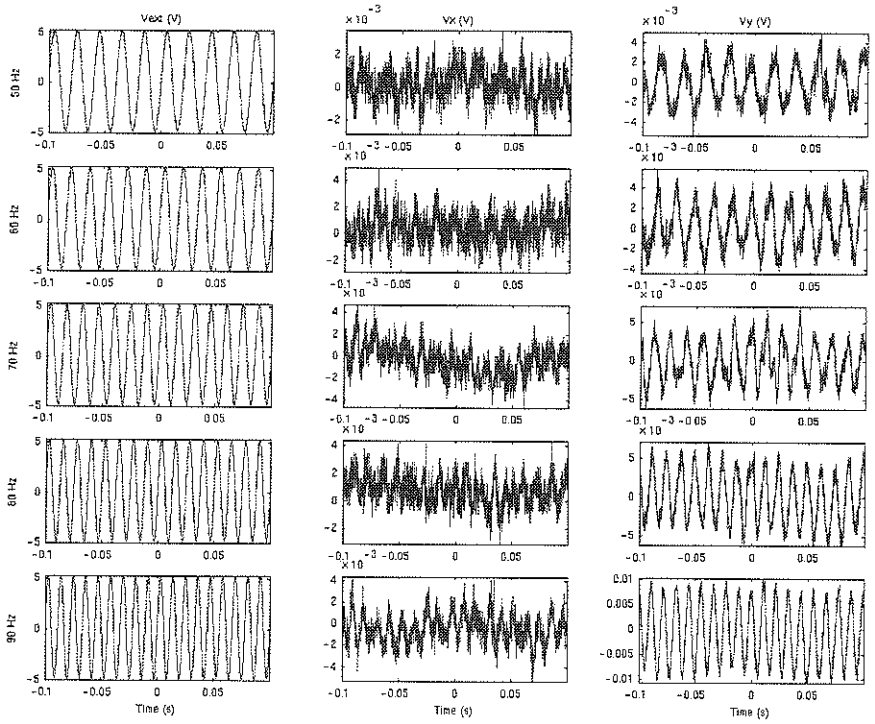

Figure A2 - 34: Membrane 4, AC testing 50 to 90Hz (run1).

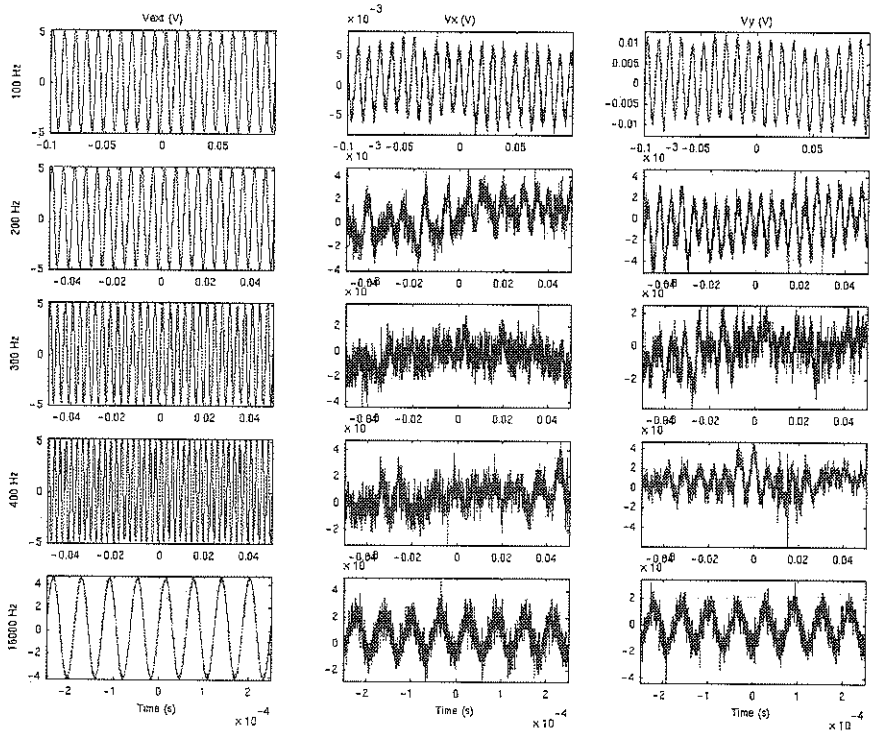

Figure A2 - 35: Membrane 4, AC testing 100, 200, 300, 400, 1600Hz (run1).

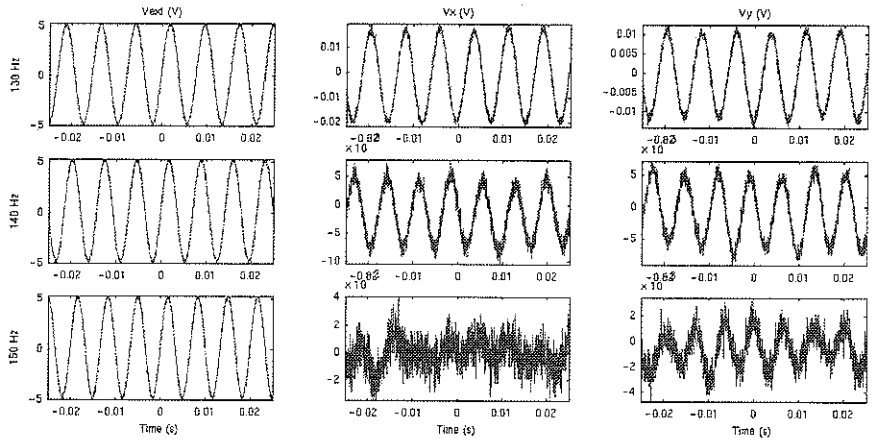

Figure A2 - 36: Membrane 4, AC testing 130 to 150Hz (run1).

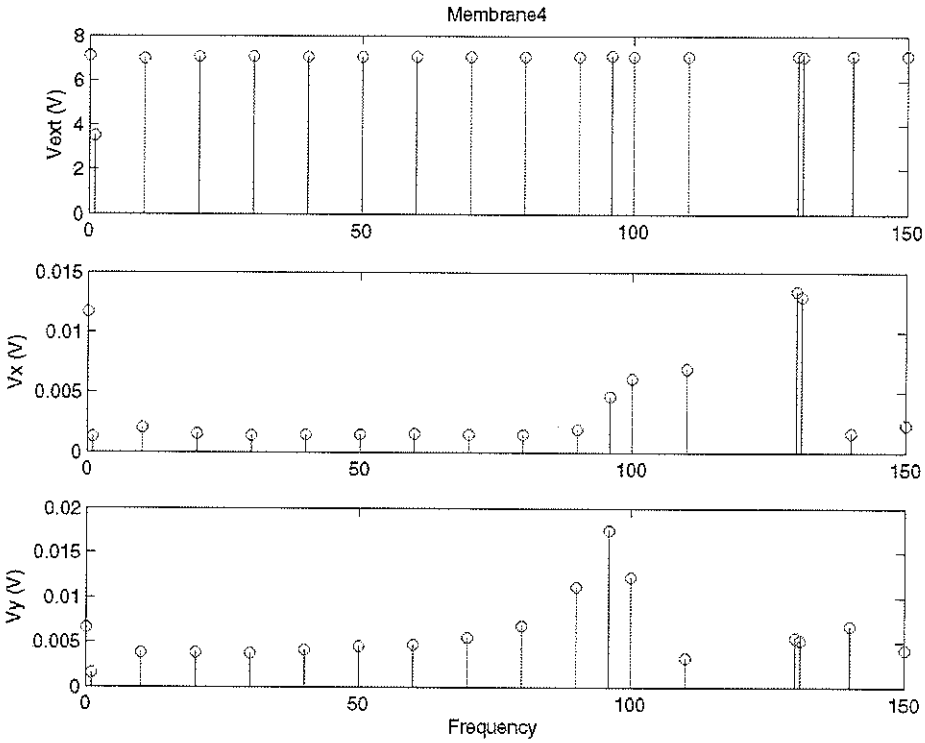

Figure A2 - 37: Membrane 4, RMS frequency response (run2).

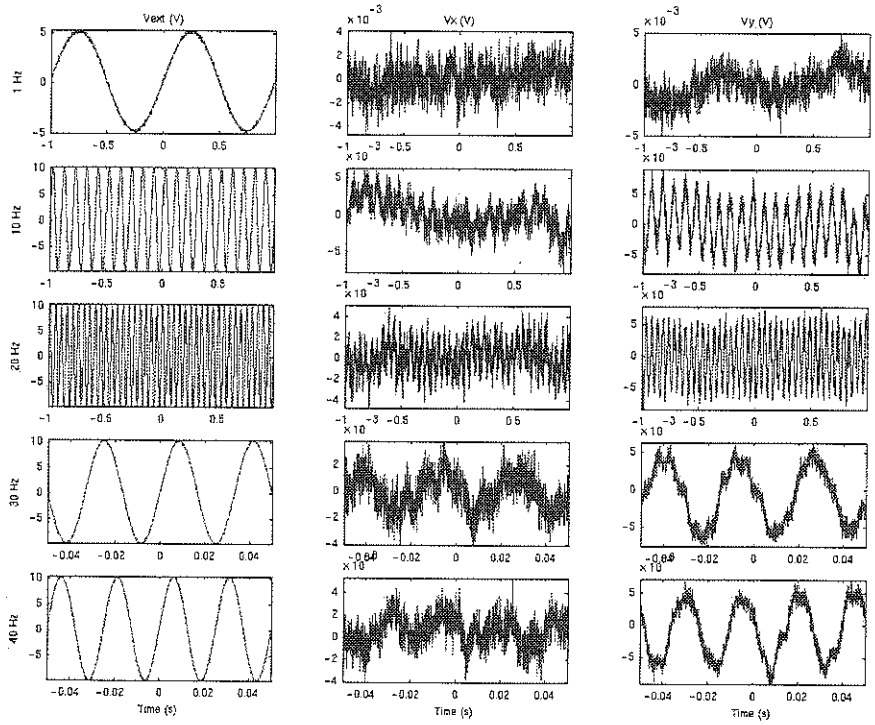

Figure A2 - 38: Membrane 4, AC testing 1 to 40Hz (run2).

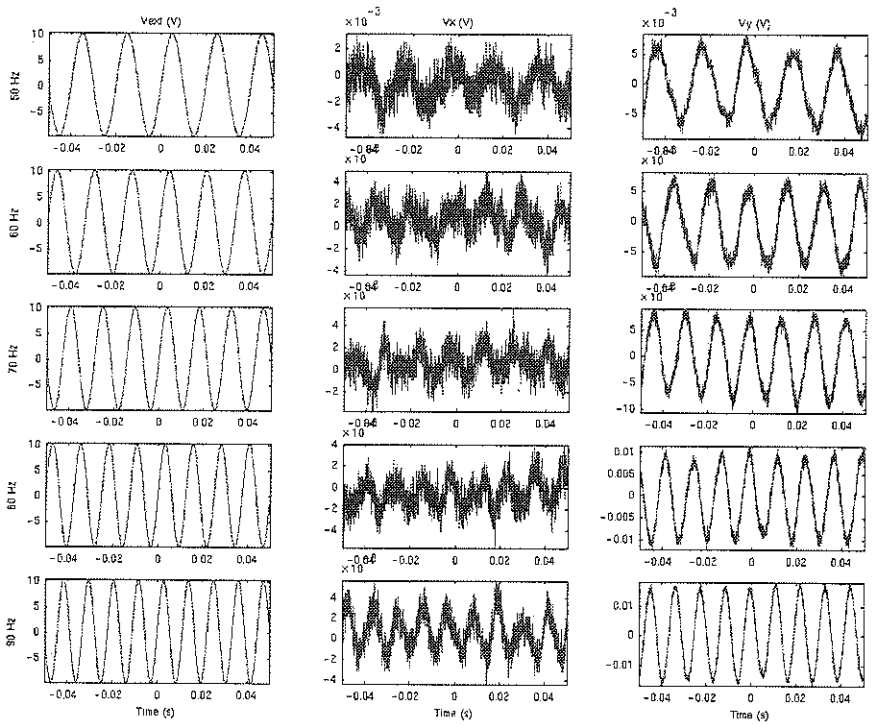

Figure A2 - 39: Membrane 4, AC testing 50 to 90Hz (run2).

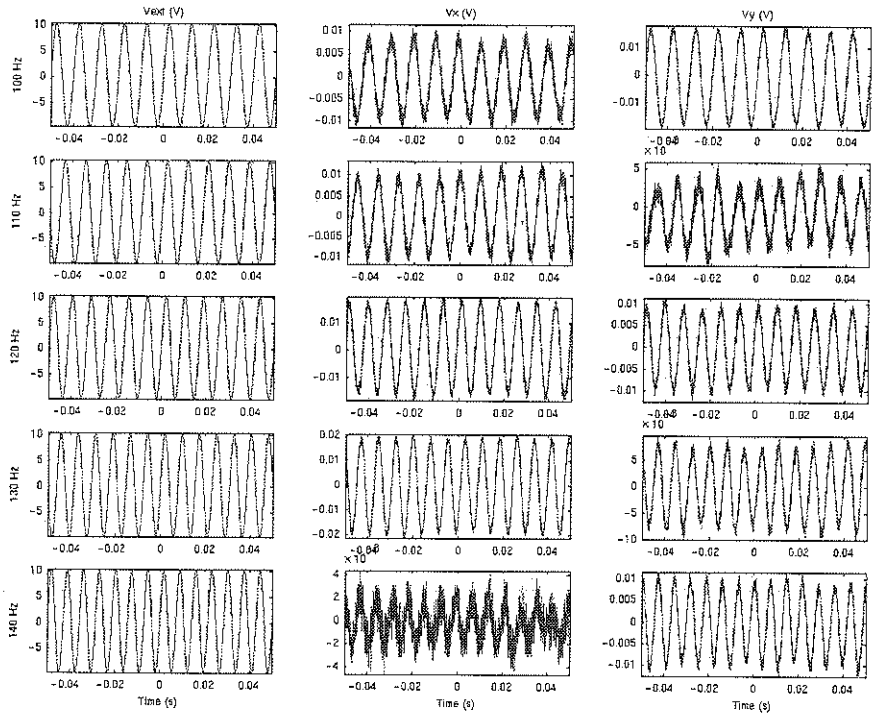

Figure A2 - 40: Membrane 4, AC testing 100 to 140Hz (run2).

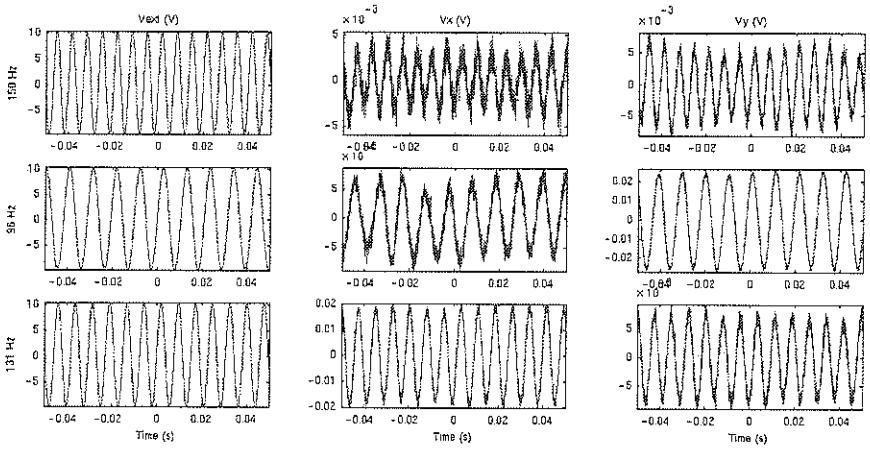

Figure A2 - 41: Membrane 4, AC testing 150, 96, 131Hz (run2).

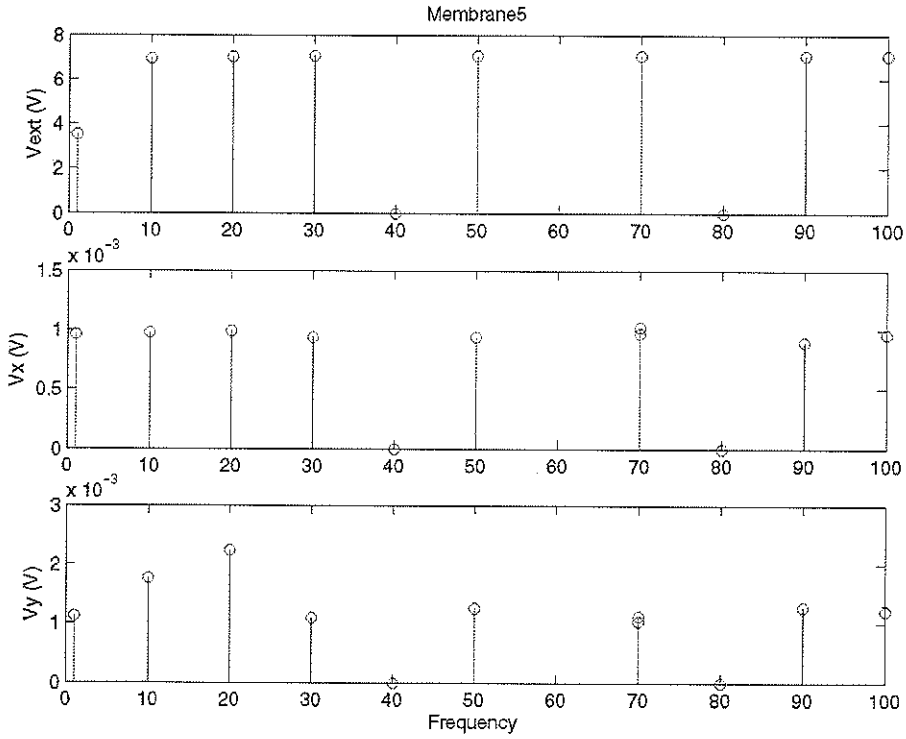

Figure A2 - 42: Membrane 5, RMS frequency response.

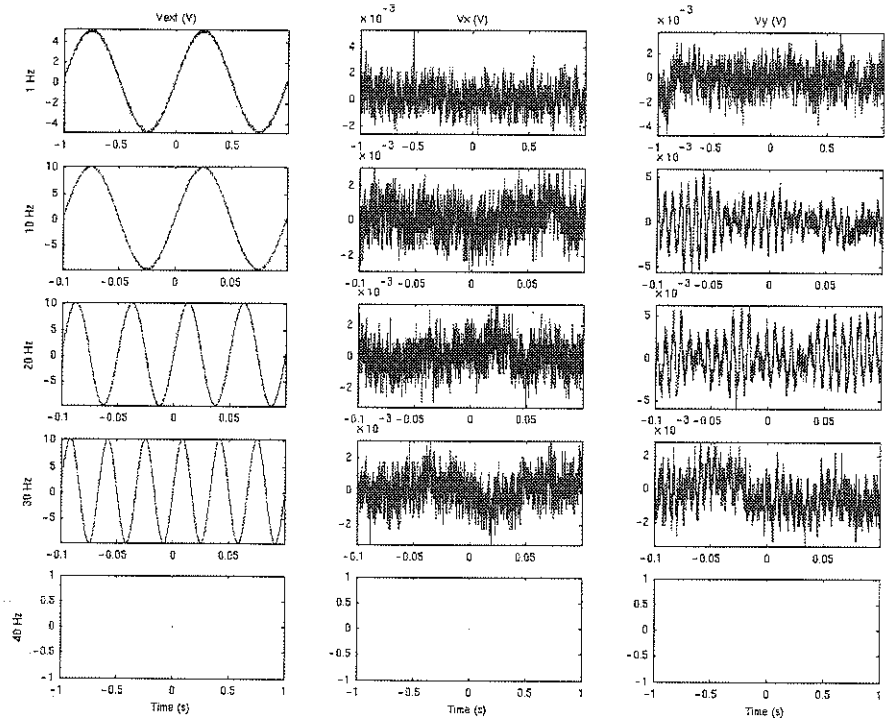

Figure A2 - 43: Membrane 5, AC testing 1 to 40Hz.

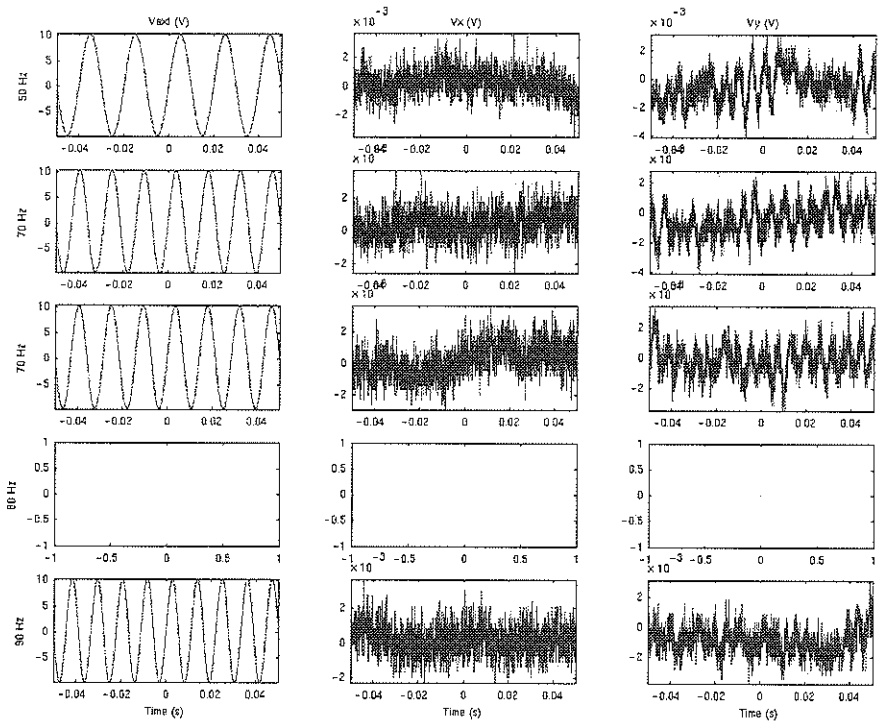

Figure A2 - 44: Membrane 4, AC testing 50 to 90Hz.

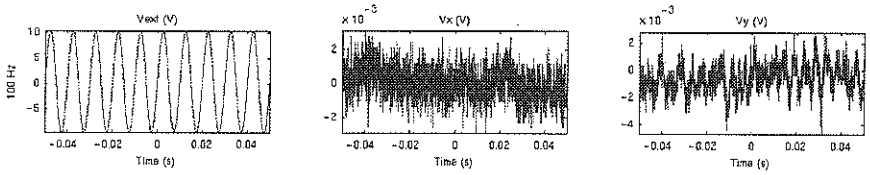

Figure A2 - 45: Membrane 4, AC testing 100Hz.

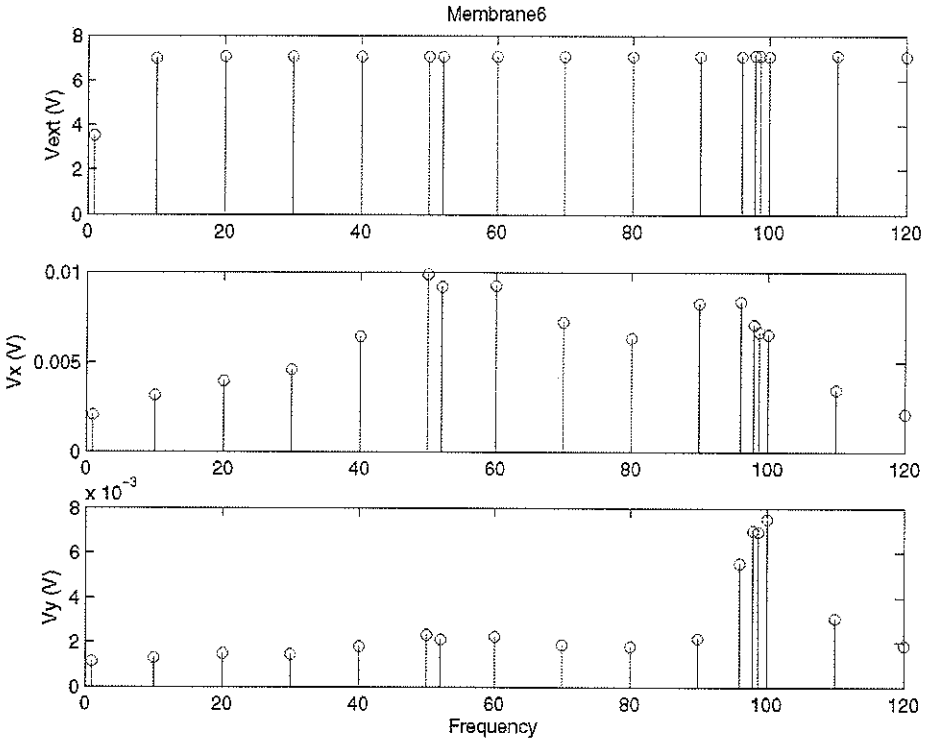

Figure A2 - 46: Membrane 6, RMS frequency response.

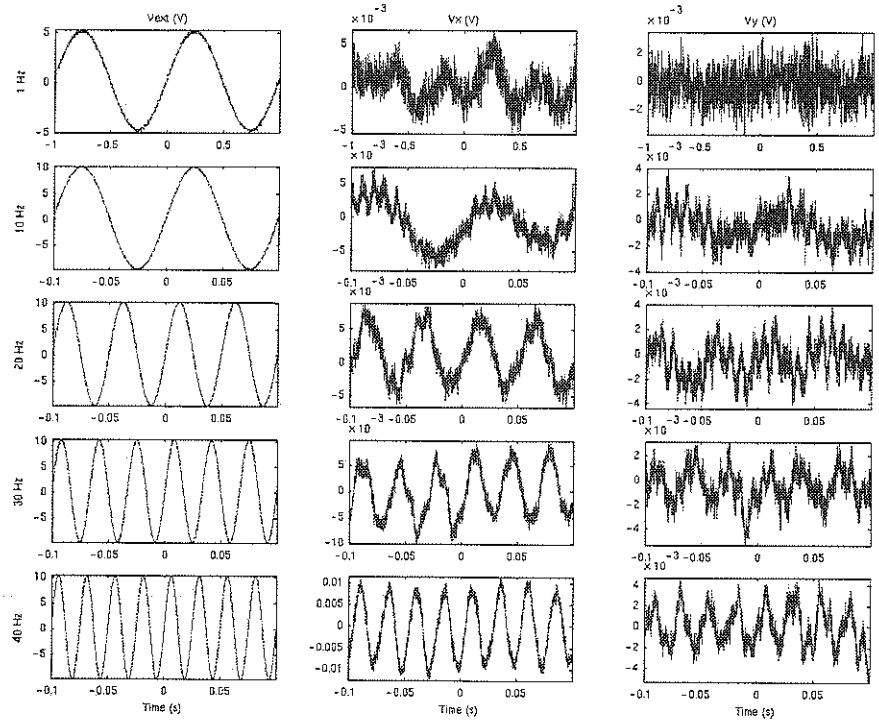

Figure A2 - 47: Membrane 6, AC testing 1 to 40Hz.

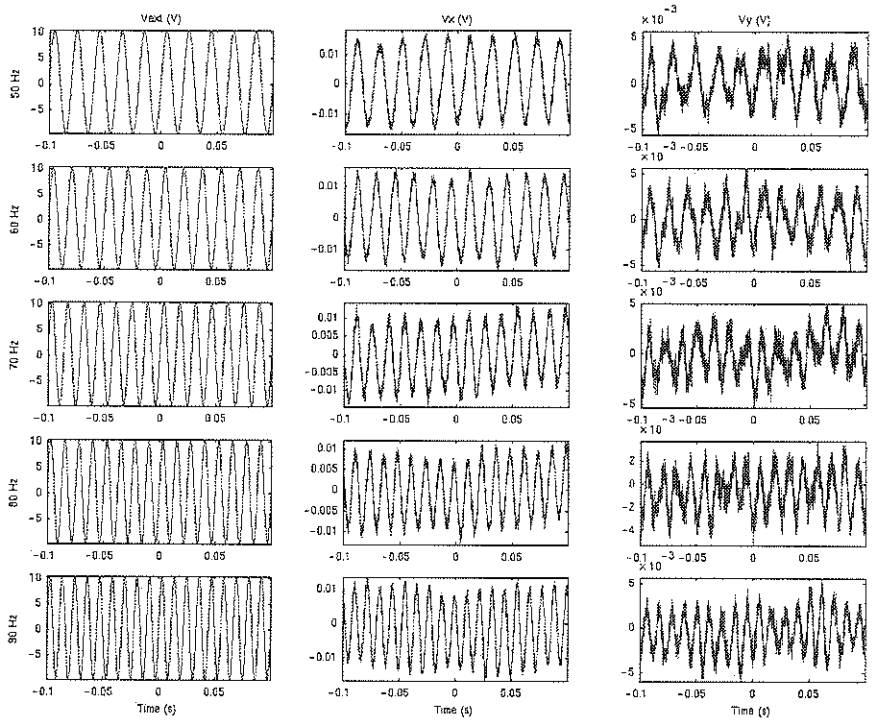

Figure A2 - 48: Membrane 6, AC testing 50 to 90Hz.

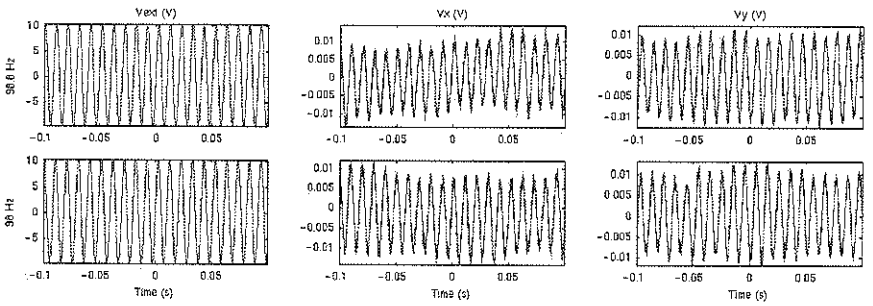

Figure A2 - 49: Membrane 6, AC testing 98.8 and 96Hz.

Appendix 3: Parts

The laser and photodiode were purchased to coincide with existing equipment in the lab. The vendors for this equipment were recommended because of their delivery times, and willingness to deal with single unit orders. Most of the optical alignment system pieces were built from stock aluminum in the departments machine shop. The electronics were constructed from manufacturer recommended circuits for precision alignment detection.

To be specific, most purchased components were selected primarily based upon recommendations by Doug Thomson. Subsequently, the selected vendors dealt in single unit orders and were compatible with existing equipment in the laboratory.

APPENDIX 3.1 Laser

A class II laser [20] was chosen for this device because of its relative safety. Class II lasers are visible and have powers up to 1mW. The safety in these devices comes from the fact that your eye can blink in response to the intense visible light *before* serious eye damage is done.

The laser chosen from Power Technology, Inc. (PTI) was a continuous wave 0.87mW, 635nm laser, model number PM01(635-5B)G3. This laser module is designed as a complete unit with constant power output. It is packaged with all the required optics and electronics, requiring only the addition of a standard 6V alkaline battery for operation.*

---

* PTI also sells a separate power supply allowing this device to be operated with regulatory compliance.

APPENDIX 3.2 Quad-cell Photodiode

The quad-cell photodiode was purchased from Advanced Photonix Inc., because they handle small volume orders. The following information in this appendix comes from the data sheet [22]. For more complete information on bi-cell and quadrant photodiodes consult information from other vendors for example application note 13, April 1982, on the UDT web site [21].

Table A2 - 1: Specifications for the quad-cell photodiode [22]

Part Number	SD 380-23-21-051	
Total Area Per Element	17.8	mm^2
Minimum Shunt Resistance	100	MΩ
Dark Current1 at 5V typical	5.0	nA
Dark Current at 5V maximum	27.0	nA
Breakdown Voltage at 10μA	50	V
Typical capacitance at 0V	375	pF
Typical capacitance at 10V	75	pF
NEP at 632.8nm	$5.2x10^{-14}$	W/√Hz
NEP at 950nm	$3.0x10^{-14}$	W/√Hz
Typical light power density	10	mW/cm^2
Typical response time at 10V	30	ns

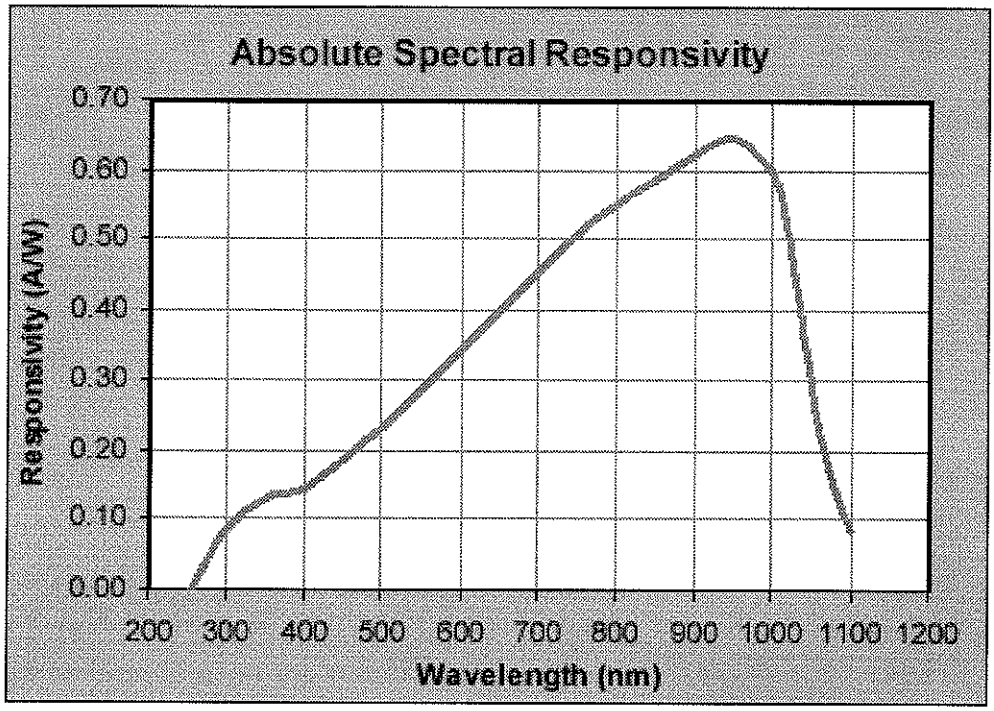

Figure A3 - 1: Quad-cell photodiode spectral response [22].

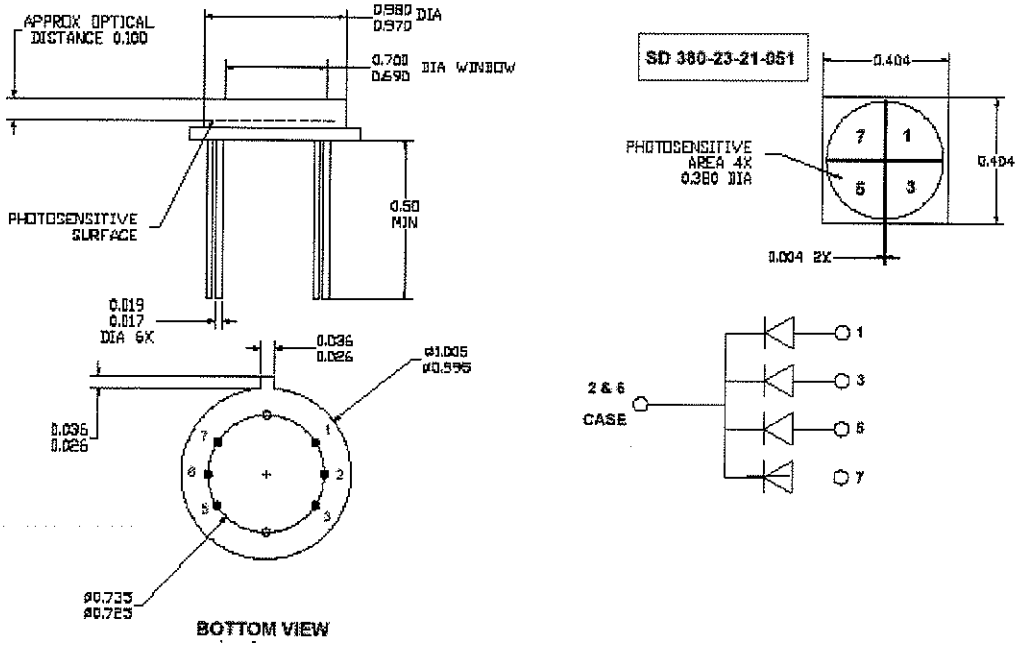

Figure A3 - 2: Quad-cell photodiode dimensions [22].

"Quadrant and bi-cell photodetectors work on the principle of having two or four separate photodiode elements separated by a small gap (2-12 micrometers) (Fig. 7). These elements are generally masked onto a common substrate so that their cathode is shared; however, the juxtaposition of discrete devices is also performed on occasion. The anode or active area of each element is individually contacted so that a light spot illuminating a single quadrant may be electrically characterized as being only in that quadrant. As this spot is translated across the detector, its energy is distributed between adjacent elements, and the difference in electrical contribution to each segment defines its relative position with respect to the center if the device." [21]

APPENDIX 3.2.1 X-Y alignment stage

For reference, the X-Y stage was a DS-40xy manually adjusted optical stage from Newport. It has a +/- 0.25 inch travel in both the x and y directions. With a 80 threads per inch screw, it could obtain 3um resolution. Since a micrometer was not required to align the detector, the manual adjustement screws and minimal play in this device were reasons for its selection.

> "Dovetail stages are preferred for small travel 'set, lock, and forget' applications. They are much less susceptible to shock and vibration than bearing stages. These DS series dovetail stages incorporate precision preloaded dovetail slides with an 80 TPI drive screw for precision positioning, hex head adjustment for tamper resistance, and an integral locking mechanism for high stability.
>
> The compact size and critical features of these stages make them ideal for OEM applications. The modularity allows reconfiguration for research applications." [25]

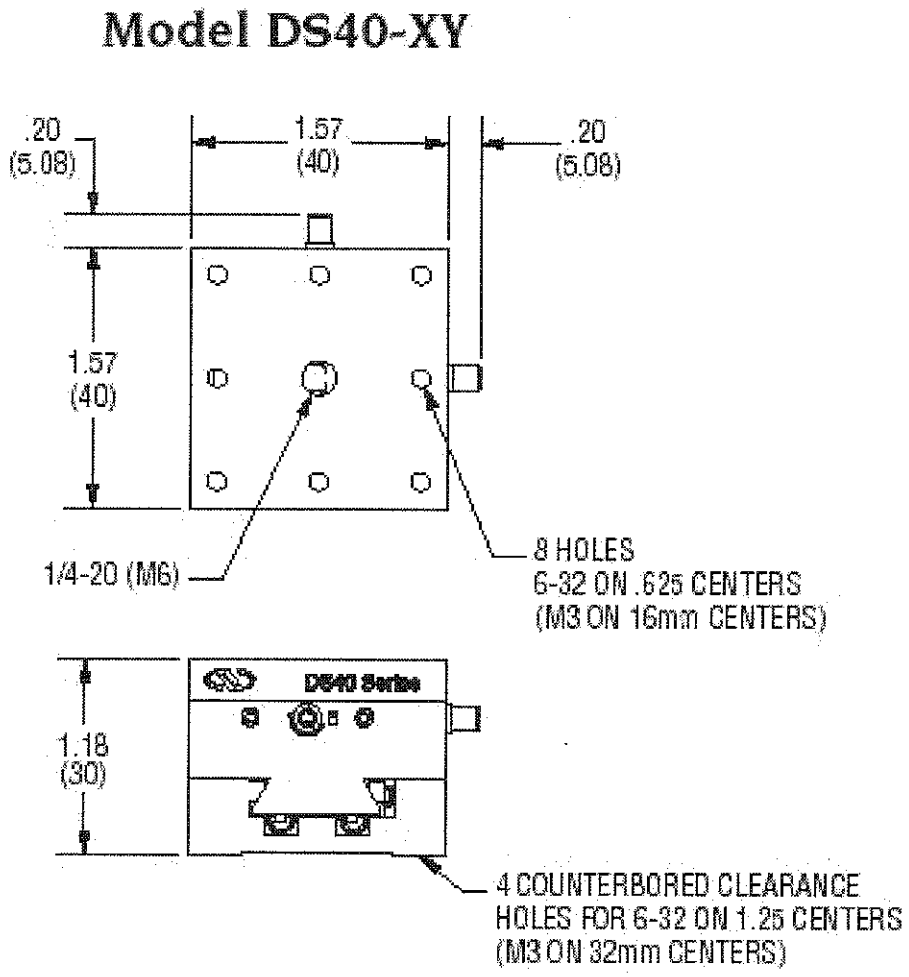

Figure A3 - 3: Model DS40-XY Compact Dovetail Linear Stage.

Appendix 4: Additional Readings

R. Bartnikas (ed), *Engineering Dielectrics Volume IIB, Electrical Properties of Solid Insulating Materials: Measurement Techniques, (ASTM STP 926),* American Society for Testing and Materials, Philadelphia, PA, 1987, ISBN 0-8031-0491-X

Douglas L. Cohen, *Demystifying Electromagnetic Equations: A Complete Explanation of EM Unit Systems and Equation Transformations*, SPIE--The International Society for Optical Engineering, 2001, ISBN 0819442348.

Marvin M. Frydenlund, *Lightning Protection for People and Property,* Van Nostrand Reinhold, New York, NY, 1993, ISBN 0-442-01338-8.

Brian Stark, *MEMS Reliability Assurance Guidelines for Space Applications*, JPL Publication 99-1, National Aeronautics and Space Administration, Jet Propulsion Laboratory California Institute of Technology, Pasadena, California, January 1999.

John N. Chubb, "Two New Designs of 'Field Mill' Type Fieldmeters not Requiring Earthing of Rotating Chopper", *IEEE Transactions on Industry Applications*, volume 26, no. 6, November/December 1990.

John Chubb, *Electrostatic Measurements: Opportunities and Applications,* V T T Automation, Electrostatics Measurements Lectures, Helsinki, May 4, 2000

H. Guckel et al, "A simple technique for the determination of mechanical strain in thin films with applications to polysilicon", *Journal of Applied Physics*, volume 57, no. 5, March 1985.

M. Horenstein, "Measuring surface charge with a noncontacting voltmeter", *Conference Record of the Industry Applications Society Annual Meeting, 1993*, vol.3, IEEE, 1993, pp 1811 - 1816

K. Kawamura et al, "Design and Development of New Electrostatic Voltmeter Using Strain Gauge", *IEEE Transactions on Industry Applications*, volume 25, issue 3, May-June 1989, pp 563 – 568.

David T. Read, "Young's modulus of thin films by speckle interferometry', *Measurement Science and Technology*, volume 9, 1998, pp 676-695

P. S Riehl et al, "Electrostatic charge and field sensors based on micromechanical resonators", *Journal of Microelectromechanical*, Systems, volume 12, issue 5, Oct. 2003, pp 577 – 589

D. M. Taylor, "Measuring techniques for electrostatics", *Journal of Electrostatics*, volume 51-52, May 2001, pp 502-508.

William .E. Vosteen, "A high speed electrostatic voltmeter technique", *Conference Record of the Industry Applications Society Annual Meeting, 1988*, vol.2, IEEE, 1988, pp 1617 – 1619.

William E. Vosteen, "A review of current electrostatic measurement techniques and their limitations', *Electrical Overstress Exposition April 24-26*, Munroe Electronics, 1984.

REFERENCES

[1] Gregory Kovacs, *Micromachined Transducers Sourcebook*, The McGraw-Hill Companies, Inc., 1998, ISBN 0-07-290722-3.

[2] D.M. Taylor and P.E. Secker, *Industrial Electrostatics: Fundamentals and Measurements*, John Wiley & Sons Inc., New York, 1994, ISBN 0-471-95233-8.

[3] *IEEE Standard Procedures for Measurement of Power Frequency Electric and Magnetic Fields From AC Power Lines (IEEE Standard 644-1994)*, The Institute of Electrical and Electronics Engineers, Inc., New York, 1995.

[4] *IEEE Recommended Practice for Instrumentation: Specifications for Magnetic Flux Density and Electric Field Strength Meters -- 10 Hz to 3 kHz (IEEE Standard 1308-1994)*, The Institute of Electrical and Electronics Engineers, Inc., New York, 1995.

[5] David Swatek, private communication 2001 to 2004.

[6] S. O. Kasap, *Optoelectronic devices and photonics: principles and practices*, Prentice-Hall Inc., New Jersey, 2001,ISBN 0-201-61087-6.

[7] Mark N Horenstein, Patrick R. Stone, "A micro-aperture electrostatic field mill based on MEMS technology", *Journal of Electrostatics*, Volume 51-52, May 2001, pp. 515-521.

[8] C. H. Hsu and R.S. Muller, "Micromechanical electrostatic voltmeter", *Solid-State Sensors and Actuators, 1991*, IEEE, 1991, pp 659 – 662.

[9] Patrick Stanley Riehl, *Microsystems for Electrostatic Sensing*, Ph. D dissertation, Engineering -- Electrical Engineering and Computer Sciences, University of California, Berkeley, 2002.

[10] W. H. Hayt, *Engineering Electromagnetics*, fourth edition, McGraw-Hill Inc., New York, 1981, ISBN 0-07-027395-2.

[11] Warren C. Young, *Roark's Formulas for Stress and Strain*, sixth edition, McGraw-Hill Inc., New York, 1989, ISBN 0-07-072541-1.

[12] David K. Cheng, *Field and Wave Electromagnetics*, second edition, Addison-Wesley, Reading, Massachusetts, 1989, ISBN 0-201-12819-5.

[13] Massood Tabib-Azar, *MICROACTUATORS, Electrical, Magnetic, Thermal, Optical, Mechanical, Chemical, and Smart Structures*, Kluwer Academic Publishers, Massachusetts, 1998, ISBN 0-7923-8089-4.

[14] Tina Shoa, private communication 2003

[15] Hector J. De Los Santos, *Introduction to Microelectromechanical (MEM) Microwave Systems*, Artech House, 1999, ISBN 089006282X.

[16] Gary Keith Fedder, *Simulation of Microelectromechanical Systems*, Ph. D dissertation, Engineering -- Electrical Engineering and Computer Sciences, University of California, Berkeley, 1994.

[17] Stephen A. Campbell, *The Science and Engineering of Microelectronic Fabrication*, second edition Oxford University Press, New York, 2001, ISBN 0195136055.

[18] Kirt R. Williams, "Etch Rates for Micromachining Processing – Part II", *Journal of Micromechanical Systems*, Vol. 12, No. 6, December 2003, pp. 761-778.

[19] *StressedMetal™ MEMS*, XEROX Palto Alto Research Center, May 13, 2004 (verified August 8, 2004) http://www.parc.xerox.com/research/eml/projects/stressedmetal/default.html.

[20] *Laser Safety*, Power Technology Inc., July 28, 2004 (verified August 8, 2004), http://www.powertechnology.com/techlib/safety.asp.

[21] *AN13 Non-Contact Optical Position Sensing Utilizing Silicon Photo Detectors*, UDT Sensors Inc., April 1982, (verified August 8, 2004) http://www.udt.com/literature.htm.

[22] *Bi-cell and quadrant photodiodes,* Advanced Photonix Inc., November 23, 2003 (verified August 8, 2004), http://www.advancedphotonix.com.

[23] *OPA27, 37 Ultra-Low Noise Precision OPERATIONAL AMPLIFIERS*, (datasheet), Burr-Brown Corporation (supplied by Texas Instruments), 1984, (verified August 8, 2004), http://www.ti.com.

[24] P. Horowitz and W. Hill, *The Art of Electronics*, second edition, Cambridge University Press, Cambridge, 1997, ISBN 0-521-37095-7.

[25] *DS Series Compact Dovetail Linear Stages*, Newport, (verified August 8, 2004), http://www.newport.com.